Faculty of Science and Engineering
Department of Exploration Geophysics

Application of Diffracted Wave Analysis to Time-Lapse Seismic Monitoring of CO2 Geosequestration

Faisal Alonaizi

This thesis is presented for the Degree of
Doctor of Philosophy
of
Curtin University

January 2014

Author's Declaration

To the best of my knowledge and belief this thesis contains no material previously published by another person except where due acknowledgement has been made.

This thesis contains no material which has been accepted for the award of any other degree or diploma in any university.

Signature: …….

Date: …….

ABSTRACT

Carbon capture and storage (CCS) is gaining attraction as a feasible strategy to stabilise or even reduce the emissions of CO_2 produced from human activities. Successful deployment of CCS projects requires reliable and cost-effective subsurface monitoring techniques. It is important to track the CO_2 plume movement in the reservoir, monitor whether CO_2 has breached the cap rock and be able to detect any leakage from the primary containment. Time-lapse seismic is often the method of choice as it provides the capability to observe changes in the subsurface caused by the gas injection with sufficient spatial and temporal resolution.

However, there are some issues with seismic methods that can affect the sensitivity of time-lapse signals to the injected CO_2. Some are related to reservoir conditions; for instance, if the injection target is a depleted gas reservoir with some residual gas or if secondary gas accumulations associated with potential small-scale CO_2 leakages are of a limited size. Other issues are associated with the repeatability of land time-lapse seismic surveys, such as geometry errors, source signature and ambient noise, which contribute significantly to time-lapse noise and hence affect the amount of CO_2 that can be detected by time-lapse seismic methods. Therefore, data processing and imaging algorithms capable of producing reliable images of the subsurface in low signal-to-noise ratio data conditions are required.

In this research a robust imaging algorithm based on detecting diffracted waves in seismic data has been developed. The algorithm is based on measuring the coherency of the data using the semblance function computed along the traveltime curve of the diffracted wave. The proposed method allows the detection of small features in the subsurface, such as linear and edge diffractors, which can be related to faults, channels on 3D seismic data, or edges of plume / altered portion of the reservoir and small-scale CO_2 accumulations on 4D seismic data. The algorithm scans over the linear/edge diffractor orientation azimuths and automatically performs a selection of a subset of data that has the highest semblance value. In the case of linear diffractors, only a small part of this surface contains the signal, the rest is noise. Therefore, this approach allows adaptively selecting that portion of the data that hosts most of the signal, which bring

stability to data with a low signal-to-noise ratio condition. The proposed method exploits the phase-reversal phenomenon of edge diffractions in the computation process and use it as a criterion to separate edge diffractions from specular reflections based on the fact that waveforms on two sides of an edge diffraction have opposite polarity.

The results of the 2D and 3D synthetic seismic data show the effectiveness of the diffraction imaging method in producing images with superior quality when compared with conventional imaging in data with low signal-to-noise ratio conditions. A numerical model based on CO2CRC Otway project data was used to investigate the sensitivity of diffraction imaging to detect a relatively small CO_2 secondary accumulation utilising time-lapse analysis as a CO_2 monitoring tool. The results indicate that the first few thousand (1000 to 3000) tonnes of CO_2 could be visible in the seismic data.

The performance of the method was then demonstrated on real 3D/4D seismic data acquired from the CO2CRC Otway project seismic surveys. Single-vintage (3D) analysis shows that the algorithm efficiently detects fault planes without the need to suppress any specular reflections beforehand. Time-lapse (4D) data analysis reveals the potential of using diffracted waves imaging to detect the boundaries of areas affected by changes at the reservoir level as specular reflections. Repeatable diffractions are cancelled out by the subtraction of the baseline stacked section from the monitor.

Future research into potential applications of the diffracted waves imaging method to different geometry settings, such as in vertical seismic profiling or in any situation where imaging of linear features in low S/N conditions, is desirable.

ACKNOWLEDGEMENTS

I take this opportunity to sincerely acknowledge King Abdulaziz City for Science and Technology (KACST) for providing the financial support for my family and me during the course of my study.

This research was partially funded by the Australian Commonwealth Government through the Cooperative Research Centre for Greenhouse Gas Technologies (CO2CRC). I would like to express my personal thanks for their support and allowing me to work on their Otway project data.

This thesis would not have been possible without the help, guidance, and valuable knowledge of my supervisor, Associate Professor Roman Pevzner. I am also extremely grateful to my co-supervisor, Associate Professor Andrej Bona, for his good advice and support during my PhD study. Additionally, special appreciation goes to the head of the Department of Exploration Geophysics, Professor Boris Gurevich, for his valuable comments and remarks.

I would like to thank the faculty and staff of the Department of Exploration Geophysics and acknowledge the contribution of Anton Kepic, Christian Dupuis, and Milovan Urosevic in designing the field experiment and data acquisition. A special thanks also goes to Valeriya Shulakova for providing the cross-equalised 3D seismic data for my research, as well as my colleagues Eva Caspari for providing the rock physics modeling results and Mohamed Alshimmary for his help in acquiring the data of the physical model experiment.

Last but not least, I would like to thank my wife, Shatha, for her love and support throughout my research and my two daughters, Maha and Nofe, for their patience and understanding.

Table of Contents

LIST OF FIGURES

1. Chapter 1- INTRODUCTION

1.1 Carbon dioxide and global warming

Global warming is widely recognised as a major challenge facing humanity in the 21st century (Houghton et al., 2001; Figueroa et al., 2008). An established scientific consensus is that the principal cause of global warming is the rise of the amount of greenhouse gases (such as CO_2, methane etc.) in the atmosphere caused by human activity (Dickinson and Cicerone, 1986; Fu and Gundersen, 2012). Options such as energy efficiency improvements, low-carbon emission energy and renewable energy sources have been adapted to mitigate atmospheric CO_2. However, fossil fuels are still the dominant source used to meet the growing demand for energy and shifting to non-carbon or renewable energy will take decades or longer (Fulcheri and Schwob, 1995; Demirbas et al., 2004) (Figure 1-1). Carbon capture and storage (CCS) has emerged as an essential strategy for the mitigation of global warming (White et al., 2003; Lipponen et al., 2011).

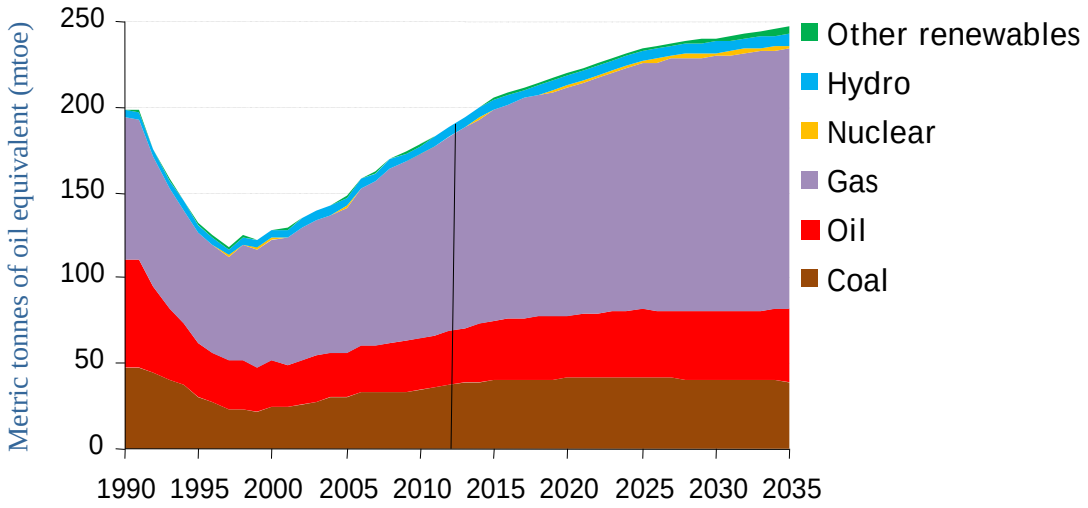

Figure 1-1: Primary energy demand in the new policy scenario (Source: OECD/IEA, 2012)

1.2 Carbon dioxide capture and storage

Carbon dioxide capture and storage (CCS) is gaining attraction as a feasible strategy to stabilise or even reduce the emissions of CO_2 produced from human activities (White, et al., 2003). CCS refers to the prevention of CO_2 emissions where the CO_2 generated from the combustion of fossil fuel is first captured then transported to a storage site and stored away from the atmosphere, usually in a deep geological formation (Stephens, 2006; McCoy and Rubin, 2008). A report published by the International Energy Agency (IEA) in 2013, concludes that CCS is currently the only large-scale mitigation option that could reduce the CO_2 emissions produced by the large industrial sectors, such as power plants, iron/steel production and chemical manufacturers.

Carbon dioxide geological storage, which is also known as CO_2 geosequestration, involves injecting CO_2 into underground geological formations for long-term storage (Figure 1-2). Various geologic storage options that can be used keep CO_2 away from the atmosphere include saline formations—deep porous rocks that contain highly mineralised brine that has no benefits to humans. The main advantages of saline formations is their potential to store huge quantities of CO_2 and their common occurrence throughout the world (Metz et al., 2005). In this case, the captured CO_2 will not require transportation to the storage site and this will reduce the overall cost of the CCS process. However, there is lack of information about saline formations when compared to oil and gas fields. Therefore, more research is needed to establish a good knowledge about this type of storage media (Michael et al., 2010). Other available CCS options are depleted or residual oil and gas reservoirs, which are considered viable options due to the extensive information that is already available about them). Uneconomic or abandoned uneconomic coal seams can also be used for CO_2 storage.

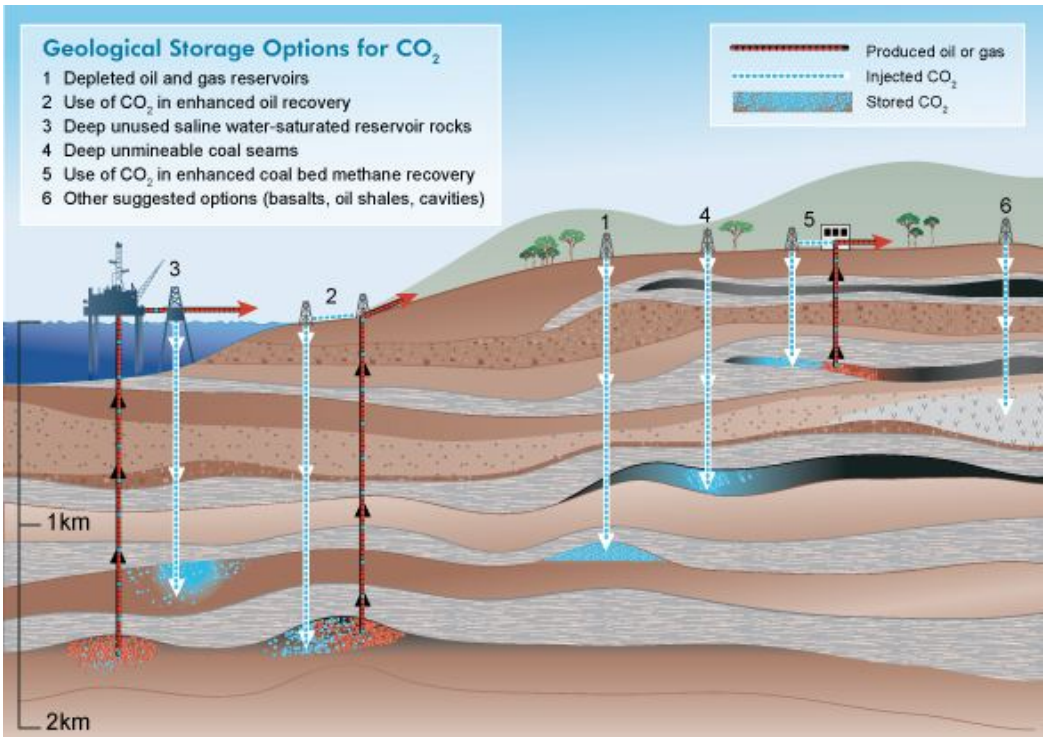

Figure 1-2: Schematic showing the geological CO_2 sequestration options (Source: CO2CRC)

CO_2 geosequestration technology was developed a long time ago by the oil and gas industry. The idea of injecting CO_2 into deep geological formations was first proposed in the early 1970s. It involves injecting CO_2 into active oil reservoirs in order to improve the reservoir's production rates and lifetime. This technology is known as enhanced oil recovery (EOR) (Brock and Bryan, 1989). Since then, the technology has become widely applied and technically viable. Now, several large-scale CO_2 sequestration for EOR projects are being undertaken around the world, such as at Weyburn Midale in Canada and In Salah in Algeria.

1.3 CCS projects around the world

Large-scale implementation of CO_2 geosequestration projects has been conducted in many part of the world, and more are planned for the future (Figure 1-3). Four CO_2 geosequestration projects are particularly large-scale (in term of the CO_2 volume injected per year): Sleipner, Weyburn, In Salah, and Snøhvit (Lipponen, et al.,

2011).

The Sleipner area in the North Sea, which was started in 1996, is considered the first commercial-scale offshore CCS project (Statoil, 2007). The CO_2 by-product that is produced with natural gas is separated and injected back into an offshore saline aquifer located 1 km below the seabed (Torp and Gale, 2004; Hermanrud et al., 2009). The Weyburn CCS project in Saskatchewan, Canada, began in 2000 as miscible flooding to enhance oil recovery. The CO_2 is transported to the injection site via pipeline from a coal gasification plant in North Dakota, USA. As of June 2012, more than 20 million tonnes of CO_2 has been stored (Jensen et al., 2013). In the Algerian Sahara Desert, a successful industrial CCS project (In Salah) started in 2004. One million tonnes of CO_2 per year have been extracted from the onshore natural gas field (Krechba field), and 70% is re-injected back into a saline leg of the gas production reservoir to enhance natural gas recovery (Durucan et al., 2011; Eiken et al., 2011). The Snøhvit project is another carbon capture and storage facility located in the Norwegian North Sea, where CO_2 injection commenced in April 2008. The CO_2 is separated from the produced natural gas then piped back and injected at the edge of the reservoir (saline aquifer) 2600 m beneath the seabed (Sweatman et al., 2011).

Figure 1-3: World map showing the current and planned CCS projects, in both saline formations and EOR or depleted gas fields (modified after Michael et al., 2010)

Table 1-1: Large-scale, integrated CCS Projects in Australia (source: Global CCS institute, 2013)

Project Name	State	Volume CO_2 (mtpa)	Operation Date	Facility Details	Capture Type
Gorgon Carbon Dioxide Injection Project	Western Australia	3.4-4.1	2015	Onshore deep saline formation	Pre-combustion capture (natural gas processing)
CarbonNet Project	Victoria	0.8-1.0	2018	Offshore deep saline formation	Yet to be decided
South West CO2 Geosequestration Hub (formerly Collie-South West Hub)	Western Australia	2.0-3.0	2017	Onshore deep saline formation	Industrial Separation
Surat Basin CCS Project (formerly Wandoan)	Queensland	1.0	2022	Onshore deep saline formation	Post-combustion capture

Since the launch of the IEA CCS roadmap in 2009 the interest in CCS technologies has increased at many levels. Governments and international organisations are collaborating and increasing investments in order to accelerate the development and deployment of CCS projects around the world. Therefore, many CCS projects are underway, planned or proposed in the next few years. In Australia, four projects have been announced to start at different locations with different CO_2 storage capacities (Table 1-1).The largest of these is the Gorgon CO_2 project where CO_2 present in the natural gas from the Gorgon group of gas fields off the northwest coast of Western Australia will be transported to Barrow Island, separated and injected into a saline formation. The construction of this project started on 15 September 2009 and the injection operations are expected to start in 2015. It will be the largest commercial-scale CO_2 injection facility in the world (Flett et al., 2009).

According to Boreham et al. (2011), existing commercial projects do not provide extensive information about the CO_2 subsurface behaviour. Therefore, pilot projects are needed in order to deliver adequate technical information on the CO_2 geosequestration process and to facilitate research into new monitoring and verification techniques, which can be adopted in future CCS projects around the world. To meet those objectives, one of the world's largest research and demonstration CCS projects (Otway project) has

been conducted by the Cooperative Research Centre for Greenhouse Gas Technologies (CO2CRC) to demonstrate that CCS is a viable option that can help Australia reduce its greenhouse gas emissions.

1.4 CO_2 monitoring and verification

Successful world-wide deployment of carbon capture and storage technology requires fast, reliable and cost-effective subsurface monitoring techniques (Benson and Myer, 2000). To make CO_2 geosequestration safe, tracking the CO_2 plume movement is important in order to observe whether CO_2 has breached the cap rock and to be able to detect leakage, if any, from the primary containment. Such tracking is necessary to minimise uncertainties associated with the long-term safety and security of the process (Oldenburg and Unger, 2003). There is a large and diverse portfolio of tools that can be utilised for monitoring CO_2 storage sites. Many of the techniques are already available and have proved to be viable while others are potentially suitable but need further development (Bannister et al., 2009). Some of the techniques are discussed in the next chapter showing their strengths and weaknesses.

1.5 CO2CRC Otway project

In 2000, a large 3D seismic survey was acquired in the Otway Basin located on the south-west coast of Victoria, Australia (Figure 1-4). The seismic exploration led to the discovery of a small natural gas field (Naylor), which was put into production from 2002 to 2004. The same site was chosen by the CO2CRC to conduct the first Australian demonstration CCS project (Otway Project) (Jenkins et al., 2012). The aim of the project is to demonstrate that CO_2 can be safely captured, transported and stored in a depleted gas reservoir (Naylor field) as a deep geological storage formation.

The initial stage of the project commenced in 2008 by extracting the CO_2-rich gas (80% CO_2, 20% CH_4) from a suspended gas exploratory well (Buttress-1). As shown in Figure 1-5, the gas is dried, compressed, and then transferred to the injection well (CRC-1). A suspended production well (Naylor-1) is used as a monitoring well (Sharma et al., 2009). A total of 65,445 tonnes of CO_2-rich gas (80% CO_2, 20% CH_4)

was successfully injected and stored in the reservoir (Naylor field) at a depth of around 2250 m (Sharma et al., 2007).

Stage 1 of the project has successfully confirmed that the CO_2 can be safely stored in a depleted gas reservoir. The CO_2 in this type of storage is structurally trapped by a seal rock above the reservoir and bound by faults on the sides (Jenkins et al., 2011). Stage 2 of the project includes further CO_2 injections into a saline formation. In order to have the information needed about the saline formation, a series of experiments was carried out using a small amount of CO_2 injected at a depth of approximately 1500 m. One of the aims of this stage is to develop a better understanding of CO_2 behaviour in saline formations by testing different types of non-structural trapping mechanisms, that is, residual gas trapping and dissolution trapping. Another aim is to study the feasibility of time-lapse seismic monitoring to resolve CO_2 plumes and track their movement in a non-structural trapping environment, where several 3D time-lapse surveys are planned to be acquired during stage 2 of the project.

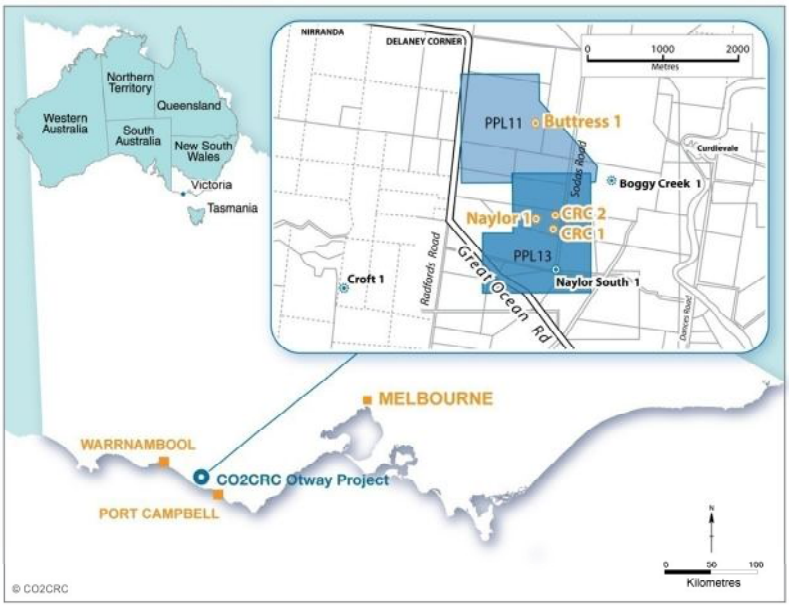

Figure 1-4: The CO2CRC Otway project located off the Great Ocean Road in south-west Victoria, Australia (Source: CO2CRC).

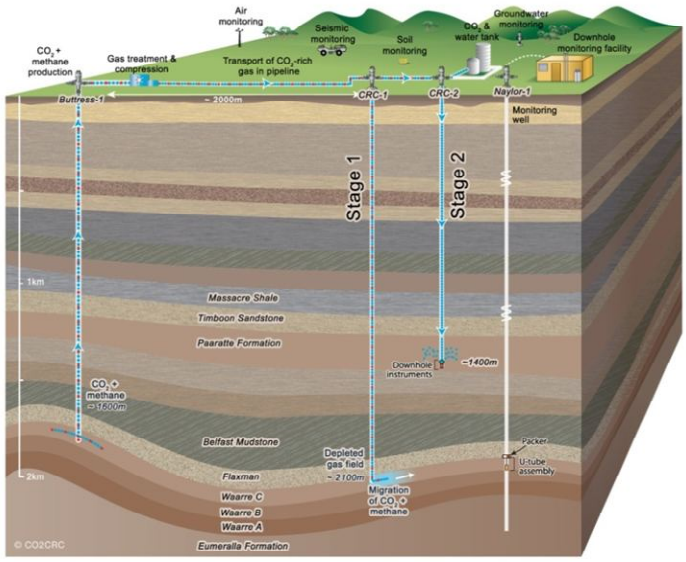

Figure 1-5: Schematic representation of the CO2CRC Otway project operation of the both stage 1 and stage 2 of the project (Source: CO2CRC).

1.6 Research motivation

The main challenge facing CO_2 geological sequestration is whether safe and stable CO_2 containment can be assured (Oldenburg and Lewicki, 2006; Wells et al., 2006). Therefore, the long-term reliability of CO_2 storage is key to the success of CCS technology. Subsurface conditions of temperature and pressure makes CO_2 density and viscosity low compared to aqueous fluids. Driven by buoyancy forces, the injected CO_2 will then tend to migrate upward to the top of the reservoir formation whenever sub-vertical permeability is available (Tsang et al., 2002; Pruess, 2005). This significantly increases the risk of CO_2 vertical leakage from the sequestration target zone into overlying strata, which could lead to contamination of other subsurface formations, hydrocarbon reservoirs or groundwater (Kumar et al., 2008). Therefore, any potential leakage pathways should be mapped and predicted as early as possible (Wells, et al., 2006).

Seismic methods are proven to be one of the most reliable methods to detect and monitor CO_2 injected into the subsurface (Lumley et al., 2008; Lumley, 2010). Many studies have demonstrated the effectiveness of seismic methods in time-lapse mode to

verify the CO_2 containment within reservoirs and map its locations and movements (Batzle and Wang, 1992; Yuh and Gibson, 2001; Arts et al., 2004; Torp and Gale, 2004; Cairns et al., 2012). Time-lapse seismic methods have also been deployed to assess the risk associated with possible CO_2 leakage scenarios and predict the CO_2 plume extent related to the amount of the leaked CO_2 from the storage reservoir (Nordbotten et al., 2004; Jenkins, et al., 2011).

However, there are issues that create difficulties for seismic methods, which affect their ability to fulfil their monitoring requirements. A hypothetical CO_2 leakage from the main storage target will not necessarily reach the Earth's surface as it can alternatively be trapped as small secondary accumulations in the upper formation with a limited lateral extend (Chang et al., 2008; Urosevic et al., 2010; Alonaizi et al., 2011; Jenkins, et al., 2011). In this case, seismic reflections may not be an ideal means for detecting and monitoring such small structures, especially if the size of the structure is small when compared to the wavelength of the seismic signal (Klokov et al., 2010; de Figueiredo et al., 2013). Moreover, injecting CO_2 into a depleted gas reservoir is not a favourable situation for time-lapse seismic monitoring, as in our case, where the injection target is a reservoir with some residual gas. This condition poses a challenge to seismic methods for CO_2 monitoring due to the remaining gas and the complex mix of various rocks in the reservoir. A modelling study done by (Caspari et al., 2012) shows that the seismic response to the presence of CO_2 is mainly below the noise level for the 3D time-lapse surface seismic data. In addition, most of the CO_2 storage sites in Australia are onshore as shown in Table 1-1, where many factors that affect the repeatability of the seismic signal are associated with land seismic acquisition (Pevzner et al., 2009). Factors such as geometry errors, source signature and ambient noise can reduce the level of repeatability of seismic surveys and contribute significantly to time-lapse noise and hence effect the amount of CO_2 that can be detected by time-lapse seismic methods (Kragh and Christie, 2002).

Developing a seismic monitoring technique is essential to detect small CO_2 plumes, track CO_2 subsurface movements, and recover the time-lapse signal in low signal-to-noise ratio (S/N) data conditions. Recent studies show that the diffractive

component of the full wave field carries high-resolution images and thus recovers information coming from structure of sub-wavelength scale (Landa, 2007; Moser and Howard, 2008; Klokov, et al., 2010). By focusing on diffracted wave imaging, and applying diffraction imaging to time-lapse data analysis, more information can be revealed in the seismic data to enhance the detectability of small CO_2 accumulations. Therefore, this research aims to explore diffractions and utilise them in time-lapse seismic data analysis for CO_2 monitoring.

1.7 Objectives

- Develop a seismic data analysis technique that is capable of detecting diffracted waves in poor S/N ratio data conditions.
- Assess the performance of the algorithm using a set of synthetic and field data examples.
- Demonstrate the applicability of the technique in time-lapse seismic data and compare it to conventional imaging techniques.
- Model a subsurface leakage scenario (in a form of a secondary accumulation) based on the geological structure, rock physics and flow simulation models provided.
- Examine the sensitivity of the seismic method using diffracted waves analysis by determining the minimum detectable amount of CO_2 that could escape from the primary reservoir based on the time-lapse seismic forward modelling of Otway data.

It is expected that this technique can be applied as a quality assurance tool to image the CO_2 plume boundary and measure the subsurface leakage magnitude early enough for action to be taken. This approach demonstrates that seismic methods are viable tools for CO_2 subsurface monitoring. Moreover, the method proposed in this work can generally be applied to identify small structure objects such as faults, pinchouts and cracks, which is very important for CO_2 monitoring.

1.8 Thesis outline

This thesis is organised into seven chapters:

Chapter one explains the importance of CO_2 subsurface monitoring to the success of carbon capture and storage as an option for greenhouse gases mitigation. Difficulties associated with seismic CO_2 monitoring are then explained to highlight the significance of developing a reliable seismic monitoring technique that will enhance the detectability of small CO_2 accumulations.

Chapter two presents an overview of the CO_2 monitoring technologies and their application to CO_2 geosequestration projects. More detailed information is then provided about Otway 3D seismic data acquisition and processing.

Chapter three provides a thorough background of the evolution of the diffraction phenomena and reviews previous work done on seismic diffraction imaging.

Chapter four describes the methodology utilised to detect diffracted wave energy for both 2D and 3D datasets.

Chapters five and six discuss the results of the method illustrated on numerical and real seismic data. The advantages of using seismic time lapse along with the detection technique are illustrated as well.

Chapter seven presents the conclusions drawn from the results obtained and suggest some recommendations for future research.

2. Chapter 2- CO_2 MONITORING AND VERIFICATION IN CCS PROJECTS

2.1 Introduction

Monitoring and verification (M&V) of geologically sequestered CO_2 is key to the success of CCS projects (Metz, et al., 2005). The large scale injection of CO_2 into the subsurface is technically possible and the oil and gas industry is well experienced in monitoring underground gas. However, monitoring of the geologically sequestered CO_2 is required on much longer time scale. It is expected that monitoring programs need to put in place during all of the storage stages: pre-operation, operation, closer and post-closer stage (Plasynski et al., 2011).

Prior to the operation stage, site selection and associated risk analysis is crucial in order to determine the appropriate monitoring program. The M&V in this stage involves:

- Identifying the site target formation.
- Reviewing existing site data (well logs, core analysis, seismic data, etc.) and acquiring more data if needed to delineate the target storage reservoir and creating baseline datasets (pre-injection) in order to allow the comparison of time-lapse datasets during and after injection.
- Developing a geological model.
- Identifying potential leakage pathways and risks.

During the operational stage (the time in which CO_2 is injected into the storage site), M&V involves:

- Verifying that CO_2 is being safely injected in the target zone.
- Tracking the CO_2 subsurface movement and identify vertical migration (if any).
- Detecting any risk factors, such as CO_2 leakage to any undesired strata or induced cracks.

The closure and post-closure stages are the periods after injection has stopped, wells used for the injection are closed and operation equipment is removed, leaving only the necessary monitoring equipment. At this stage, M&V involves:

- Confirming the injected CO_2 is confined in the target formation.
- Working with surveillance tools to protect the environment as well as the public health and safety.
- Providing information to validate flow simulation models based on the monitoring results.

Therefore, sequential observation to assess the environmental and operational monitoring is required. This includes a comprehensive monitoring program in different domains: subsurface, near surface, and atmospheric (Figure 2-1).

2.2 CO_2 geosequestration monitoring technologies

There are different types of monitoring techniques available for CO_2 sequestration projects; many of these techniques are well established while others are being tested at existing commercial and pilot injection projects (Sauer et al., 2013; Schmidt-Hattenberger et al., 2013). Both offshore and onshore monitoring tools can be categorised based on the depth of investigation: subsurface monitoring (deep), near-surface/surface monitoring (shallow), and atmospheric monitoring (Martens et al., 2013). A non-exhaustive list of CO_2 monitoring techniques are discussed in the following sections.

2.2.1 Subsurface monitoring methods (deep):

The primary objective of deep monitoring techniques is to observe the CO_2 movement and confirm that it remains stable below the cap rock. Other objectives are to provide an early warning if the CO_2 breaches the cap rock reaching a shallower depth and to obtain better geological structure information in order to identify potential leakage pathways and hence bring down the risk uncertainties (IEAGHG, 2012). Most of these methods mainly rely on geophysical and geochemical principles and can be performed either on the surface or on wells. Seismic methods are considered well established methods that can provide high quality images of the subsurface structures

and identify lateral and vertical CO_2 plume migration (Arts, et al., 2004; Chadwick et al., 2005). Unlike surface seismic, well-based seismic methods, such as vertical seismic profiling (VSP) and cross-well tomography, can provide better temporal resolution and monitored of the thin CO_2 layer. However, VSP information is limited to a short distance from the measuring wells, where surface seismic has superior spatial coverage (Urosevic et al., 2011).

One major challenge that seismic methods face is the uncertainty when describing the CO_2 quantities in the subsurface as thickness and saturation are both sometimes difficult to define (Wells, et al., 2006; Korre et al., 2011). Passive seismic monitoring can provide valuable information about the pressure front, monitor induced seismicity (geo-mechanical deformation) due to CO_2 injection at the reservoir level and monitor fracturing in the sealing layers (Bohnhoff et al., 2010; Verdon et al., 2010). As in VSP techniques, they also suffer from limited spatial coverage. Electromagnetic (EM) or controlled-source electromagnetic (CSEM) methods can detect the change of electrical conductivity due to CO_2 displacement. EM methods are inexpensive when compared to seismic methods and have the potential to provide data with high sensitivity to CO_2 movement, especially in saline aquifers (Park et al., 2013). Cross-well EM techniques have been adopted in the oil and gas industry as they can be combined with seismic methods in order to predict the CO_2 gas/oil ratio in complex hydrocarbon reservoirs (Hoversten et al., 2002). Other non-geophysical monitoring tools are mainly based on direct measurements performed on solids, liquids and gases and are mainly geochemical techniques. Perfluorocarbon tracers, and U-tube are multi-level geochemical sampling systems that have the capabilities to track the CO_2 migration at reservoir level and detect and quantify CO_2 leakage at the shallow layers (Freifeld et al., 2005; Jeandel et al., 2010).

2.2.2 Near-surface/surface monitoring methods (shallow)

The primary objective of the near-surface monitoring system is to identify whether or not CO_2 leakage is occurring. Their measurement tools aim to detect, locate and quantify the CO_2 that could escape from the target injection zone and migrate upward to the near surface (vadose zone). Direct measurement of the soil-CO_2 flux, groundwater

and tracers are acquired regularly using downhole fluid samples in order to monitor the changes in CO_2 concentration. The geochemical monitoring tools are classified based on the chemical nature of the measured species, which include a wide spectrum of chemical and isotopic parameters, such as the pH[1] measurements, or ion concentration (Elodie and Philippe, 2012). For example, in case of leakage into a near-surface freshwater aquifer, the CO_2 concentration will increase in the aquifer and water becomes more acidic. This can be detected by measuring the pH parameter where it will give low values due to the presence of CO_2 in the water (Dethlefsen et al., 2013). On the surface, a high precision surface deformation tools, such as tiltmeters can be deployed on the surface or be placed in a shallow borehole (McColpin, 2009). Tiltmeters measure tilt movements with an accuracy up to 1 nanoradian as they can record very small change on the surface caused by small subsurface terrain changes due to CO_2 plume upward migration (Ringrose et al., 2009; White, 2013).

2.2.3 Atmospheric monitoring

The earth's surface and atmosphere monitoring methods are very important as they can obtain direct CO_2 measurements and provide assurance to the public that the gas is being contained within the target formation. CO_2 fluxes and concentrations are measured periodically in order to identify and locate any possible CO_2 leakages at the surface. There are different atmospheric techniques that are suitable for CO_2 gas leakage related to CO_2 geo-sequestration. These techniques can be measured from point, line and area sources, such as flux chambers and micrometeorological methods (Leuning et al., 2008).

However, one major problem in atmospheric monitoring is distinguishing between the background measurement (natural CO_2 cycle, and other sources) and the real signal (leaked CO_2). Therefore, a long sampling time is needed to establish background measurements (Lewicki et al., 2005). Another drawback in atmospheric monitoring tools is that they are point-based, which makes them suffer from spatial shortcomings. This can be avoided by placing the tools where CO_2 release is expected, near abundant

[1] The pH of a solution is a measure of the molar concentration of hydrogen ions in the solution and as such is a measure of the acidity or basicity of the solution. The letters pH stand for "power of hydrogen".

wells, or in areas of concern, such as faults or fractures. High-resolution satellite images that can monitor millimetre-scale vertical movement can be used to measure the surface deformations caused by the CO_2 subsurface movement. This method has been deployed in the In Salah project where the results of time-lapse images are more successful than originally expected (Mathieson et al., 2009).

Therefore, a broad range of monitoring tools has been successfully applied to different CO_2 storage sites. Studies show that different monitoring tools, such as seismic, CSEM, and satellite imaging can effectively track and monitor injected CO_2 at different levels (Benson, 2006; Benson and Cole, 2008; Wildenborg et al., 2009; Mathieson et al., 2011). By running in a “time-lapse” mode, these tools can find the differences between the baseline measurements and the subsequent (monitor) measurements (after CO_2 injection). However, each monitoring tool has different parameters and applications, so understanding the tool limitations is essential in order to predict whether the objectives of the monitoring program will be met (Simone et al., 2009). Each geo-sequestration site has a different geological structure and risk profile, which requires case-by-case cost-effective and focused monitoring tools. Thus, a proper monitoring program requires integrating various monitoring technologies that need to be applied simultaneously in order to monitor the sequestered CO_2 and validate that it remains in the target formation.

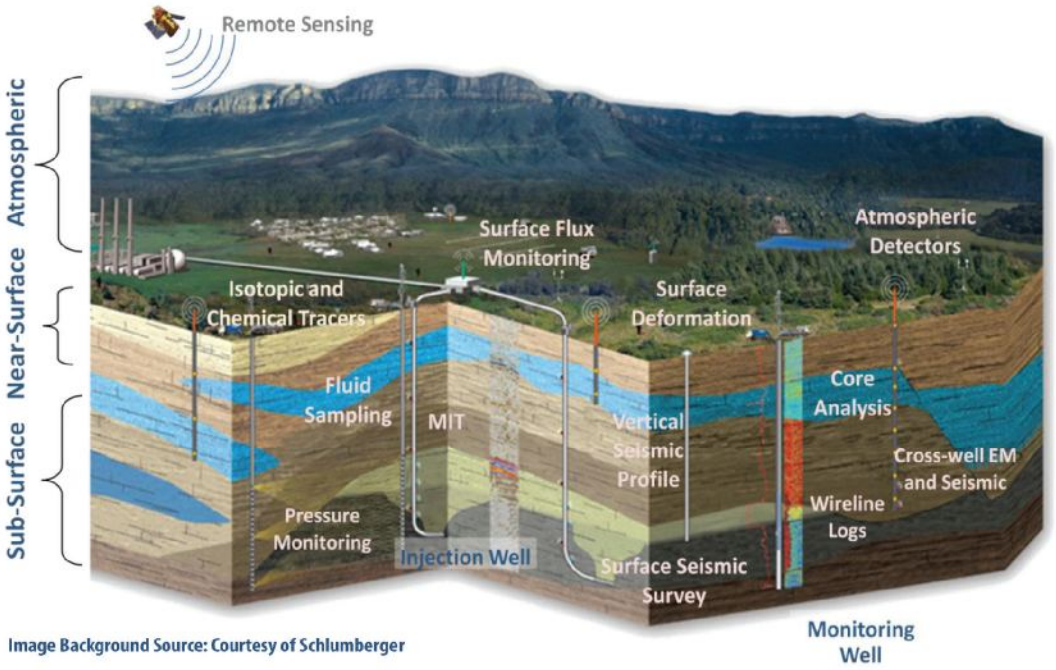

Figure 2-1: The three CO_2 monitoring categories: subsurface, near surface, and surface domains (Source: NETL, U.S. Department of Energy).

2.3 Seismic monitoring of sequestered CO_2

Injecting CO_2 into a formation will change its pore fluids contents causing physical rock properties, such as density and P and S-wave velocities, to change due to fluids substitutions (Gassmann, 1951; Smith et al., 2003). This change provides appropriate seismic properties for CO_2 monitoring. The same seismic monitoring methods that have been successfully used to track fluid movement in oil and gas industry can be applied to monitor and verify the injected CO_2 subsurface movement (Lumley, et al., 2008; White, 2011). The most obvious application of seismic methods for CO_2 monitoring is in time-lapse mode where a number of seismic surveys are acquired over the storage site at every stage of the project (White, et al., 2003). The 3D time-lapse technique (also known as 4D) is proven to be one of the most promising methods to detect and monitor CO_2 injected into the subsurface where it has been effectively utilised to verify CO_2 containment within reservoirs (Arts, et al., 2004; Torp and Gale, 2004).

Time-lapse seismic methods in CO_2 geo-sequestration are mainly used to verify the CO_2 containment in the injection zone (short term monitoring) and to monitor the CO_2

front movement away from the injection zone (long term monitoring) (Alonaizi et al., 2013). The literature shows significant contributions of time-lapse seismic analysis for CO_2 monitoring. White (2009) demonstrated the ability of 4D seismic methods to monitor physical changes in Weyburn reservoir and showed the distribution of CO_2 and indicated that P-waves time-lapse seismic monitoring is sensitive to the presence of a CO_2-rich gas within the reservoir (Figure 2-2). Chadwick et al. (2010) provided time-lapse seismic images that showed the evolution of the Sleipner CO_2 plume and track its growing accumulation over time as shown in Figure 2-3. These images clearly show the vertical and lateral expansion of CO_2 plume over the injection period.

However, the applicability of seismic monitoring methods to detect CO_2 depends on the magnitude of change in the subsurface elastic properties after CO_2 injection. Properties such as velocity and density, along with the reservoir conditions are important factors that affect the CO_2 response on seismic data (Korre, et al., 2011). Therefore, a feasibility study is mandatory for any storage site prior to injection since time-lapse seismic repeatability alone is not enough to detect CO_2 response (Kazemeini et al., 2010).

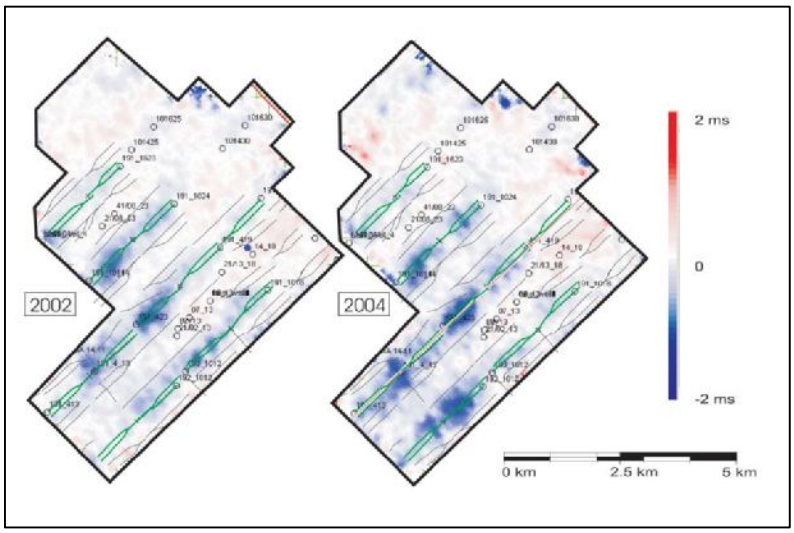

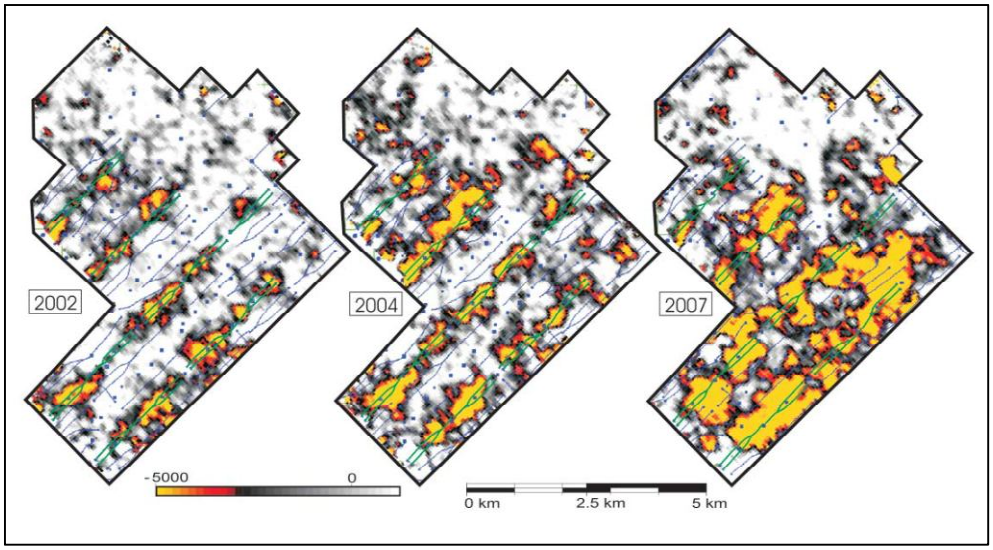

Figure 2-2: (top) Time-lapse traveltime difference determined for a horizon within the reservoir level showing the traveltime anomalies. (bottom) Time-lapse negative amplitude difference showing the accentuated CO_2 saturation effects (after White, 2009).

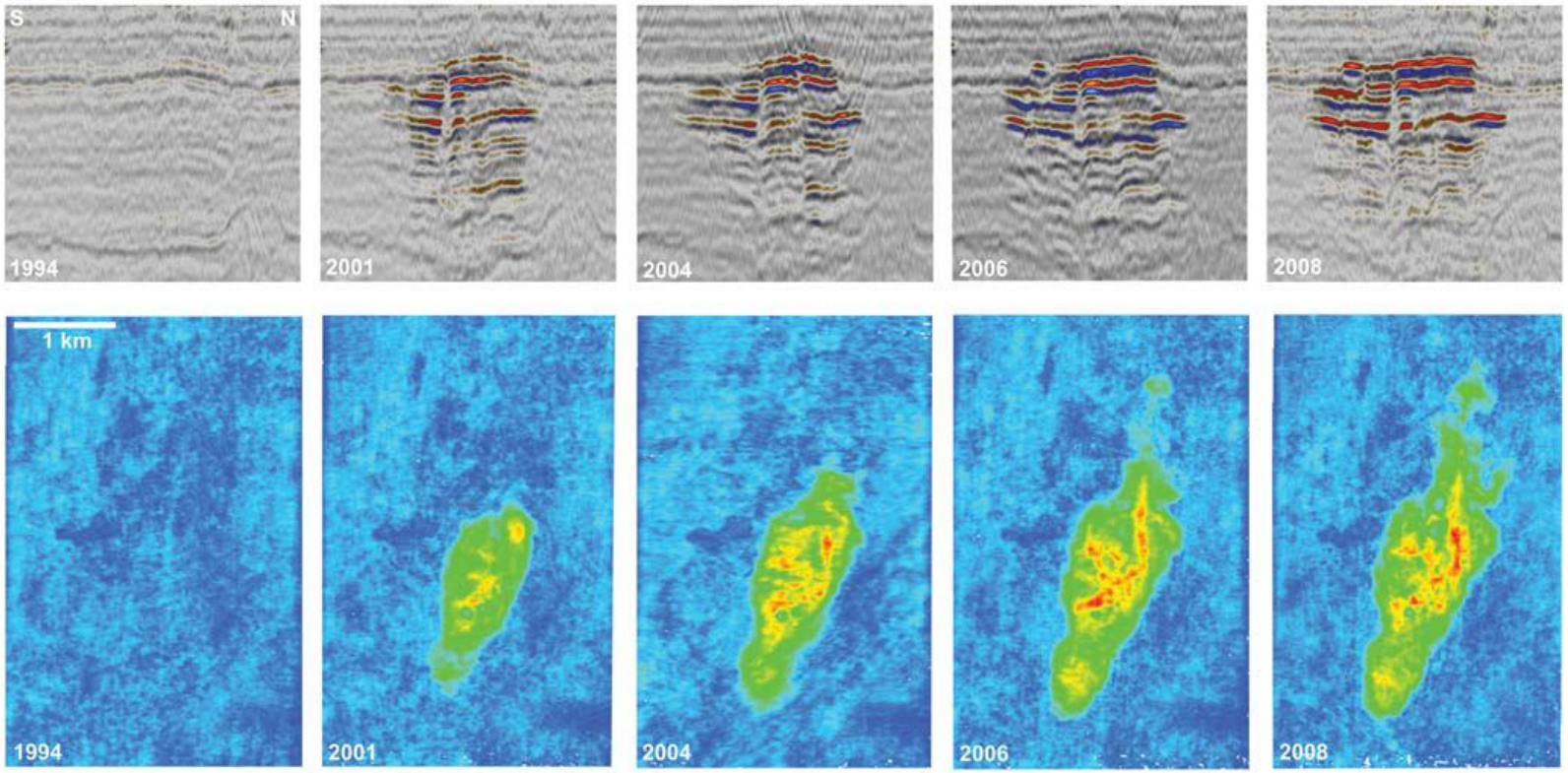

Figure 2-3: Time-lapse seismic data images of the Sleipner CO_2 plume for five surveys. (top)In-line cross-section through the injection point. (bottom) Time-slices of the total reflection amplitude of the plume. (after Chadwick et al., 2010).

2.4 Seismic monitoring in the Otway project

CO2CRC has put in place an extensive monitoring and verification program in the Otway project. The monitoring procedures include atmospheric monitoring, geochemical monitoring (e.g., soil and ground water) and geophysical monitoring using seismic surveys. A range of seismic monitoring techniques has been utilised including vertical seismic profiling (VSP), high resolution 4D surveys and micro-seismic surveys.

2.4.1 Time-lapse seismic data acquisition

Several 3D surface and borehole seismic surveys were acquired during stage one of the project. 3D surface seismic surveys were repeatedly acquired over the storage site by Curtin University crew. A baseline survey (pre-injection) was shot in January 2008. Then the first and second repeated surveys were acquired subsequently in 2009 and 2010 after the injection of about 35000 tonnes and 66000 tonnes of CO_2/CH_4 respectively (Table 1).

It is most desirable to conduct 3D surveys using the same acquisition equipment; however, this is not always possible, as in our case where limited receiver cables were available. The 2008 survey was acquired in two swaths with two receiver line groups: group I (435 channels) was shot by odd source lines 1-27 and 28 and group II (437 channels) was shot by even receiver lines 2-24 and 29 using a weight drop source where all geophones for the survey were fixed and not moved during the survey. In the next two surveys (2009 and 2010), all receiver lines were used for every single shot (Figure 2-4) and the seismic source was changed from weight drop to 15,000 lbs vibroseis (IVI Mini-vibrator) in order to provide more energy (Figure 2-5).

Both laboratory data and field experiments suggest that the influence of CO_2 on seismic properties of rocks is sufficiently strong enough to be detectable (Lumley et al., 2008). However, there are many issues that may arise when dealing with time-lapse seismic methods in CO_2 monitoring. Unlike marine surveys, acquiring time-lapse seismic data for CO_2 detection in onshore sites is a challenging task due to the repeatability issue that can affect the time-lapse signal (Pevzner, et al., 2009). Unavoidable variation in the weathering layer between surveys, ambient noise generated by rain or wind and source receiver coupling can have a significant impact on the repeatability of land seismic data.

The high nominal fold 3D survey was designed to optimise the signal-to-noise ratio and improve the repeatability of the time-lapse signal (Urosevic, et al., 2011). The nominal stacking fold was doubled from ~100 for the 2008 survey to ~200 for 2009 and 2010 as shown in Figure 2-6, where the full spread (all receiver lines) was used for each shot point.

Table 2-1: Acquisition parameters used for the 3D seismic monitoring surveys acquired at Otway site.

	Survey I	**Survey II**	**Survey III**
Date	2008 baseline	2009 after injecting 35,000 tonnes of CO_2	2010 after injecting 66,000 tonnes of CO_2
Source	Weight drop (concrete breaker), 1350 kg.	IVI Mini-vibrator, 12s sweep Frequency: 10 – 140 Hz	
Bin size	10 x10 m	10 x 10 m	
Number of source points	2181	2223	
Source spacing	20 m		
Source line spacing	100 m		
Number of Receiver lines	10		
Receiver line spacing	100 m		
Receiver point spacing	10 m		

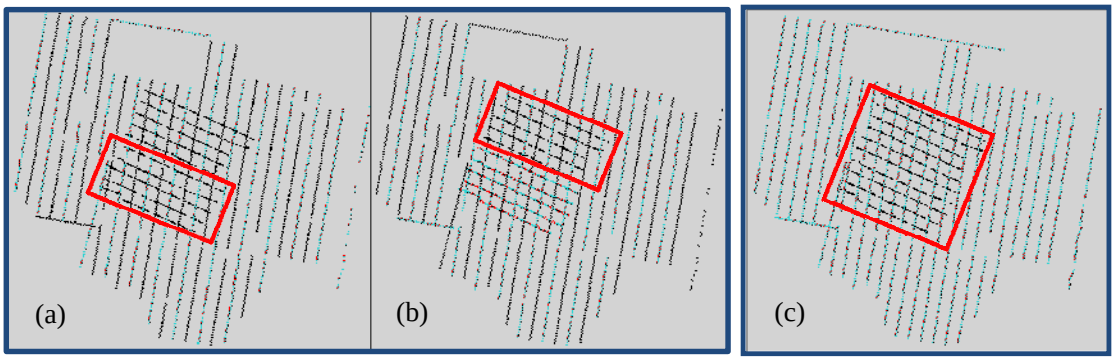

Figure 2-4: Base map of the geometry layout of source and receiver lines: (a) for the year 2008, the first swath was recorded by 1-5 receiver lines using the odd source lines (blue dotted lines), (b) the second swath was recorded by 6-10 receiver lines using the even source lines and (c) all source lines were recorded by all receiver lines for the repeated surveys (2009 and 2010).

Figure 2-5: Seismic source type used for the Otway seismic survey data. (left) Weight drop source and (right) Mini-vibrator source.

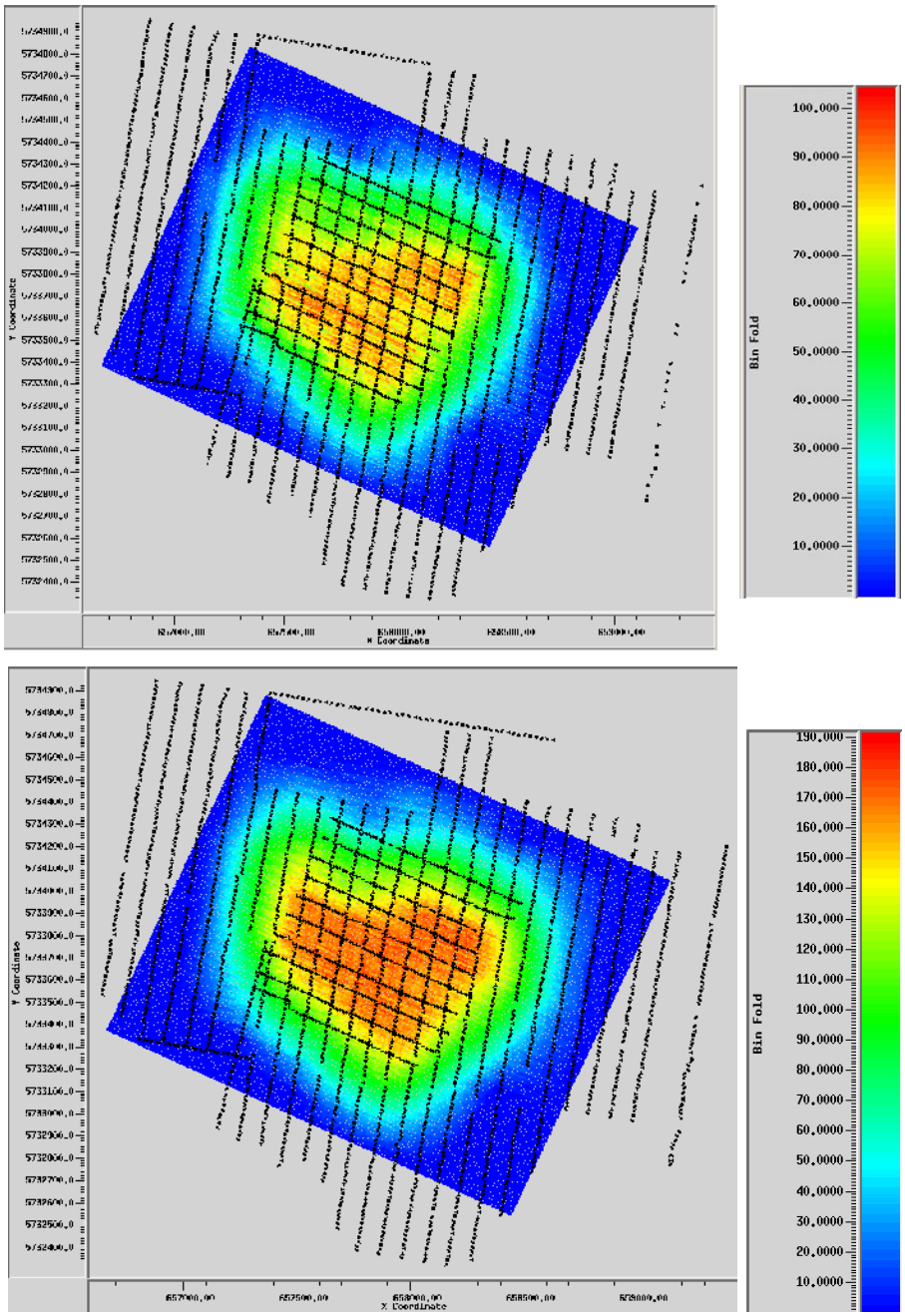

Figure 2-6: (top) Common depth point (CDP) fold map of the 2008 survey with a nominal fold of 100, (bottom) where it has been doubled for the 2009 and 2010 surveys.

2.4.2 3D seismic processing and cross-equalisation

The three seismic volumes conducted for 4D analysis were analysed and processed simultaneously through the same processing flow focusing on preserving reflection amplitudes. The difference between the source types (weight drop and vibroseis) affects the shape of the wavelet and the frequency content between surveys as well as the coherent noise, which is very pronounced in the data (Figure 2-7). Therefore, this effect needs to be removed in order not to spoil the equalisation between the three vintage sets. The number of channels per shot was reduced for the data of 2009 and 2010 to the match the number of channels that was used in 2008 dataset. After that, a trace-equalisation of the data was performed in order to be able to make the data comparable using the following steps (Shulakova et al., 2012)

- **Static corrections** (time shift): Even with well-repeated geometry a systematic wavelet difference is unavoidable due to the change of weathering layer conditions. A post-stack time shift was calculated and applied to match the reflector's geometry on different surveys. The 2009 survey data was used as the master (reference) survey because of its obviously superior data quality. A cross-correlation was then used between corresponding traces pairs of cubes (2008-2009, 2010-2009, and 2010-2008) and a calculated static shift was applied to the data of 2008 and 2010 to match 2009 data.

- **Shaping filter:** After applying time equalisation, a matching filter was applied in order to remove the residual amplitude and phase difference between the data. The match filter was designed to make both volumes (2009 and 2010) match the 2008 volume.

- **Time variant gain function (TVG):** A time variant scaling function was derived from the data where the amplitude characteristics were very similar for the 2009 and 2010 volumes but not the 2008 volume due to the much weaker source energy used for the 2008 survey. Therefore, a TVG function was only applied to the 2008 volume as an adjustment in order to match the amplitude spectrum of the 2009 and 2010 volumes.

Figure 2-8 shows the cross-equalisation results of the three migrated volumes that can be used for time-lapse analysis to investigate the effect caused by the CO_2 injection. The results obtained from cross-equalisation show a very subtle change in seismic data due to the residual gas and the complex mix of various rocks in the reservoir, which increases uncertainty as to whether the change is real or artefacts.

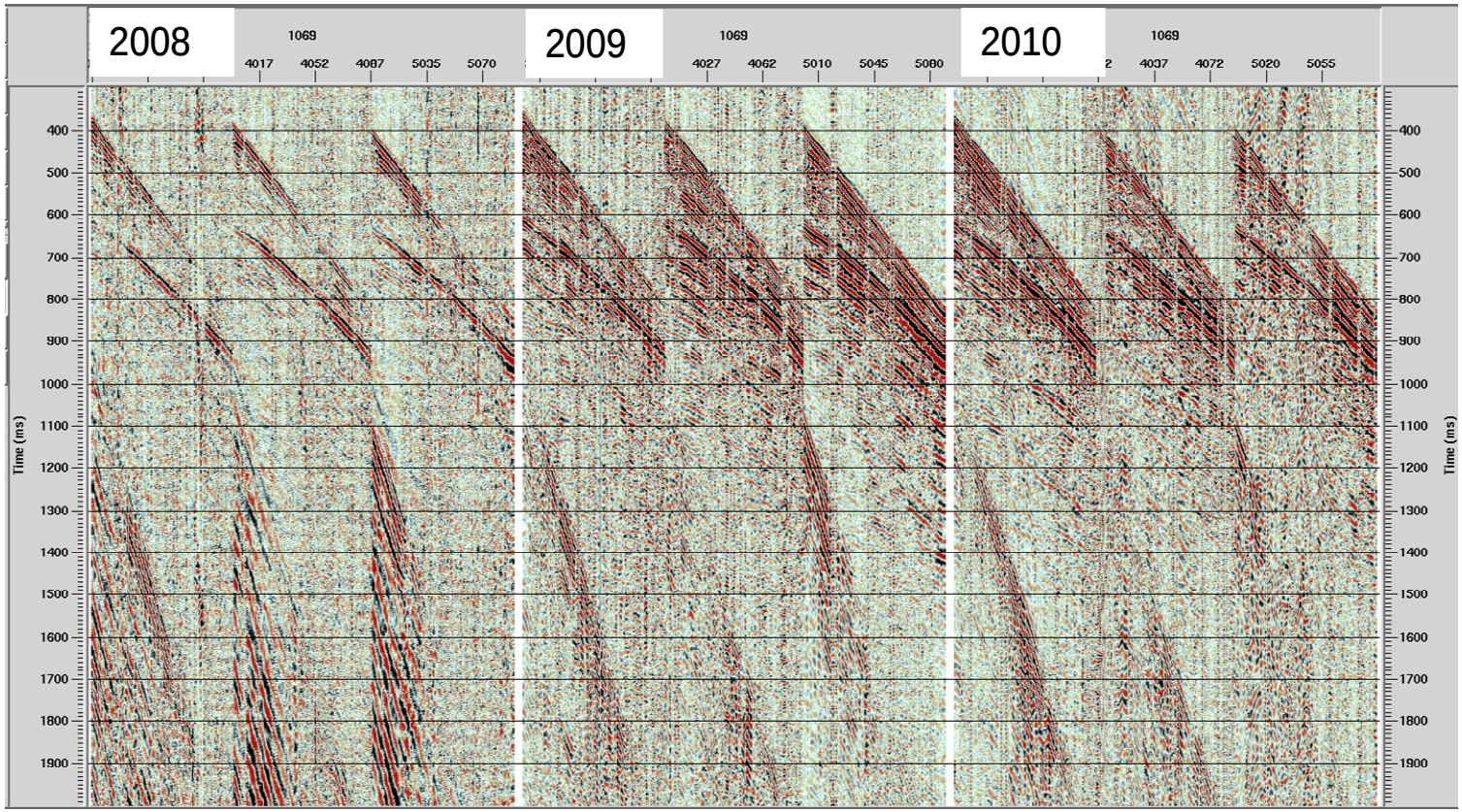

Figure 2-7: A comparison between one raw shot gather for the three surveys. Notice the difference between 2008 and both 2009 and 2010, where the seismic energy is much weaker in 2008 where its spectral content varies significantly.

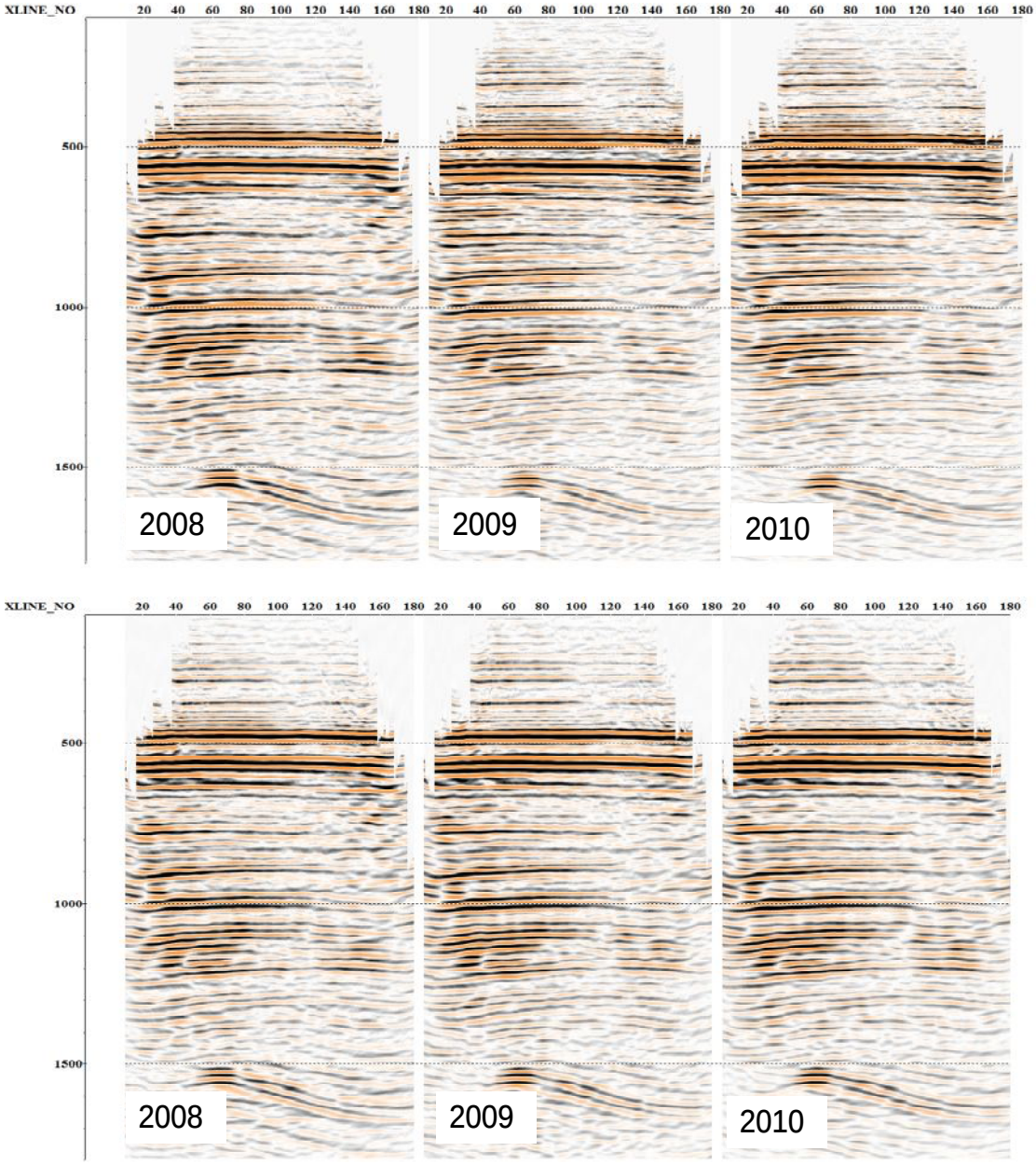

Figure 2-8: Migrated time section of in-line 87 of the three surveys: (top) after conventional seismic data processing and (bottom) the same section after cross-equalisation.

2.5 Conclusion

Successful deployment of carbon capture and storage projects requires fast and reliable monitoring techniques to detect small amounts of CO_2 that could escape from the primary containment. A comprehensive monitoring and verification program must be implemented during all stages of the project. CO_2 properties, such as low density and viscosity, increase the risk of leakage, which could lead to contamination of other subsurface formations, hydrocarbon reservoirs or groundwater. Therefore, continuous monitoring is required at and around the storage reservoir and at different depths, from the reservoir level up to the surface. A significant number of research studies and pilot projects focus on developing new monitoring technologies and enhancing the existing ones in order to detect leakage and quantify CO_2 stored in reservoirs.

A wide range of monitoring techniques can be utilised for CO_2 monitoring sites; however, the effectiveness of each technique is different from site to site. Seismic methods (surface and borehole) have proved to be very effective tools that can provide spatial coverage of the subsurface CO_2 movement and possibly trace its distribution. Time-lapse seismic surveys have an important role in the Otway project, where several high density 3D seismic surveys were acquired to assure the absence of leakage from the reservoir. The results obtained from Otway 4D seismic analysis suggest that the time-lapse signal is very weak due to the presence of the residual gas in the reservoir. Therefore, novel seismic imaging approaches can be employed in order to enhance the detection of time-lapse signals.

3. Chapter 3 - DIFFRACTED WAVES IN APPLIED SEISMOLOGY

3.1 Introduction

When a seismic wave passes a structure whose radius of curvature is shorter than the wavelength of incident wave, or encounters an abrupt change at the reflection interface, the laws of reflection and refraction no longer apply. In such situations the incident seismic energy is radiated in all directions; the phenomenon is known as *diffraction* (Muncaster, 1993). A common source of diffraction is the edge of an interface caused by faulting, cracks, paleochannels, intrusions and so on.

Seismic diffraction imaging has recently gained more attention where diffracted waves are treated as valuable information that can be analysed in processing rather than in interpretation. Diffraction imaging is becoming an important part of seismic data processing, where more accurate delineation of reservoir structures and fracture zones can be provided (de Figueiredo, et al., 2013). However, diffraction energy is one or even two orders of magnitude weaker than reflection energy, which makes it difficult to identify (Landa et al., 2013). Therefore, imaging diffracted waves suggest unconventional processing approaches in order to extract or separate diffraction events from specular reflections.

3.2 History of diffraction theory

Diffraction phenomenon was firstly reported by Johannes Marcus Von Kronland (1595-1667) in his book published in 1648 that discusses the colour of rainbow and the diffraction of light around a wire (Porter and Teich, 1992). Others believe diffraction was first reported by Leonardo da Vinci in the 15^{th} century (Born and Wolf, 1999). However, Francesco Maria Grimaldi (1618-1663) was given the main credit as he created the term “diffraction” as a fourth mode of light other than rectilinear, refracted and reflected and was the first to record an accurate observation of the phenomenon in his posthumously published two-volume book (Grimaldi, 1665). Newton studied the phenomenon in optics and attributed it to inflexions of light rays as he believed that light was made up of tiny particles (Feynman, 2006). In 1678, a physicist named Christian Huygens gave an explanation of the propagation of light using a wave model. This great

accomplishment is what is known as Huygens' Principle and implies that each point on the wave front can be considered as a source of secondary spherical wavelets with a speed equal to the speed of propagation of the waves (Huygens, 1690). This theory describes why the light when passing through an aperture spreads out rather than propagates along a straight line. Tomas Young (1804) introduced and demonstrated the concept of interference of light and deduced that light must propagate as waves based on his famous double-silt experiment. The ideas of Huygens and Young were brought together by French physicist Augustin-Jean Fresnel (1788-1827), who invented the idea of dividing the wave front into a certain series of zones and explained Young's experiment mathematically for the first time. Unlike Huygens, who only described the propagation of light and not the diffraction phenomena, Fresnel developed the wave theory of light to explain the diffraction, reflection, and refraction. Fresnel elaborated on the Huygens' principle and with his interference principle was able to explain the diffraction effects in his famous memoir that won the prize of the French Academy of Science (Fresnel, 1819).

But not until 1882 were the ideas of Huygens and Fresnel put in a formal mathematical theory by Gustav Kirchhoff. Based on the solution of the Helmholtz equation by means of Green's function, in the case of diffraction from the aperture of a plane screen Kirchhoff described the field on the screen in a form of an integral over the aperture (with the use of two approximations about the boundary condition) as a result of the interference of Huygens's secondary sources.

Since then the subject of diffraction has been extensively discussed by many authors. In 1962 an article written by Joseph B. Keller described the diffraction of a ray, which described the modern formulation of diffraction theory known as "Geometrical theory of diffraction" (GTD), one of the most cited in the modern diffraction literature. GTD is considered an extension of Geometrical Optics (GO) as it postulates another method of ray generation in addition to reflection and refraction. The GTD employs an extension of Fermat's principle and assumes that the diffracted field behaves like diffracted rays.

3.2.1 Helmholtz-Kirchhoff theory, Synthesis of the Huygens-Fresnel principle

The Kirchhoff diffraction formula expresses the Huygens-Fresnel principle mathematically using Green's function and Helmholtz equation in the context of acoustics and for mono-chromatic waves. Following the work of Goodman and Gustafson (1996), to derive the formula let us consider two complex valued functions *U* and *G* of position *P* in a volume *V* enclosed by a surface as shown in Figure 3-1. The volume does not include the singular point *P*. According to Green's theorem the following relationship holds for the given functions *U* and *G*:

$$\int_v (U\nabla^2 G - G\nabla^2 U)dv = \oint_s \left(U\frac{\partial G}{\partial n} - G\frac{\partial U}{\partial n}\right)ds, \qquad 3\text{-}1$$

where *n* is the outward vector normal to the surface *S*. The complex functions *U(P)* and *G(P)* can be represented by the time-independent equation known as the Helmholtz equation:

$$(\nabla^2 + k^2)U = 0 \quad \text{and} \quad (\nabla^2 + k^2)G = 0, \qquad 3\text{-}2$$

where ∇^2 is the Laplace operator, and *k* is the wave number given by

$$k = \frac{2\pi}{\lambda}, \qquad 3\text{-}3$$

and where λ is the wavelength in the medium.

Considering *G* to be a spherical wave originated at point P_o to P_1, with the help of Green's theorem, the function *G* at an arbitrary P_1 is expressed by

$$G(P_1) = \frac{e^{jkr}}{r}, \qquad 3\text{-}4$$

where *r* is the length of vector $\vec{r}$ measured from the point P_o to P_1. The field solution at any point P_o can be obtained by knowing the field distribution of the wave in a closed surface *S* surrounding a volume *V*, by substituting Helmholtz equation 3-2 into the Green's function:

$$U(P_o) - \frac{1}{4\pi}\oint_{s'}\left[\frac{\partial U}{\partial n}\left(\frac{e^{jkr}}{r}\right) - U\frac{\partial}{\partial n}\left(\frac{e^{jkr}}{r}\right)\right].dS. \qquad 3\text{-}5$$

This result is known as *Helmholtz-Kirchhoff integral theorem* of the diffraction problem, which plays an important role on the developing of the scalar theory of diffraction.

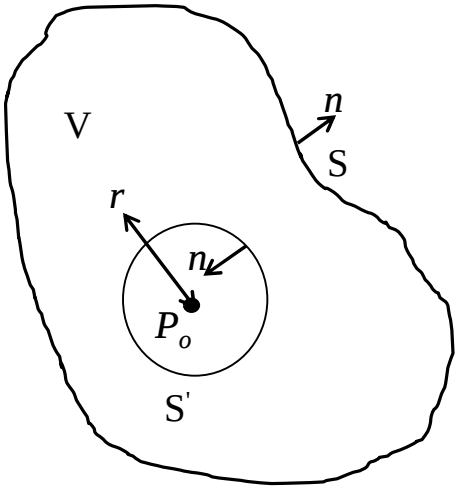

Figure 3-1: A volume *V* enclosed by a surface S. The volume does not include the singular point *P*.

Kirchhoff's second major contribution to the theory of diffraction was the application of the theorem to the problem of diffraction light by a small aperture in an infinite opaque screen as shown in (Figure 3-2a). Where the surface *S* consists of two parts: a plane surface laying behind the diffraction screen S_c, and a large spherical cap, S_R of radius *R* centred at the observation point P_o. The total closed surface *S* is simply the sum of S_c and S_r, thus applying (3-5):

$$U(P_o) - \frac{1}{4\pi}\iint_{S_C+S_R}\left(G\frac{\partial U}{\partial n} - U\frac{\partial G}{\partial n}\right)dS, \qquad 3\text{-}6$$

where $G = \frac{e^{jkr}}{r}$.

As *R* increases, S_r approaches a large hemispherical shell. We can say since both *U* and *G* will fall off as 1/*R*, the integral over the S_r will ultimately be zero. Thus, to calculate the disturbance at P_o we consider the integral just over S_c:

$$U(P_o) - \frac{1}{4\pi}\iint_{S_C}\left(\frac{\partial U}{\partial n}G - U\frac{\partial G}{\partial n}\right)dS. \qquad 3\text{-}7$$

As mentioned earlier, the screen is opaque except for the open aperture (S_A). From equation 3-6 the major contribution to the integral is from S_C located within the aperture S_A where we expect the integration be large. Kirchhoff accordingly made the following simplifying assumptions:

1. Away from the aperture, the field U and its derivative $\partial U/\partial n$ are the same as in the absence of the screen.
2. The field U and its derivative $\partial U/\partial n$ are equal zero.

These two conditions are commonly known as the ***Kirchhoff boundary conditions***. The equation 3-6 can then be reduced to

$$U(P_o) - \frac{1}{4\pi}\iint_{S_A}\left(\frac{\partial U}{\partial n}G - U\frac{\partial G}{\partial n}\right)dS. \qquad 3\text{-}8$$

A further simplification of the expression for $U(P_o)$ is obtained by noting that the distance r is much larger than the wave length (λ), that is, $k>>1/r$, we can say that

$$\frac{\partial G(P_1)}{\partial n} = jk\cos(\vec{n},\vec{r})\frac{e^{(jkr)}}{r}. \qquad 3\text{-}9$$

Substituting this approximation in equation 3-7, we find

$$U(P_o) - \frac{1}{4\pi}\iint_{S_A}\frac{e^{(jkr)}}{r}\left(\frac{\partial U}{\partial n} - jkUcos(\vec{n},\vec{r})\right)dS. \qquad 3\text{-}10$$

Now suppose that the aperture is illuminated by a single spherical wave

$$U(P_1) = \frac{Ae^{jkr_1}}{r_1},$$

arising from a point source at P_2, at a distance r_1 from $P1$ (Figure 3-2 b), the equation 3-10 can be directly reduced to

$$U(P) - \frac{A}{j\lambda}\iint_{S_A}\frac{e^{[jkr(r_1+r]}}{r}\left[\frac{cos(\vec{n},\vec{r})-cos(\vec{n},\vec{r_1})}{2}\right]dS. \qquad 3\text{-}11$$

This result is known as the ***Fresnel-Kirchhoff formula*** for an illumination of a single point source. Note that the formula is symmetrical with respect to source and observation point, which is referred to the reciprocity of the wave equation.

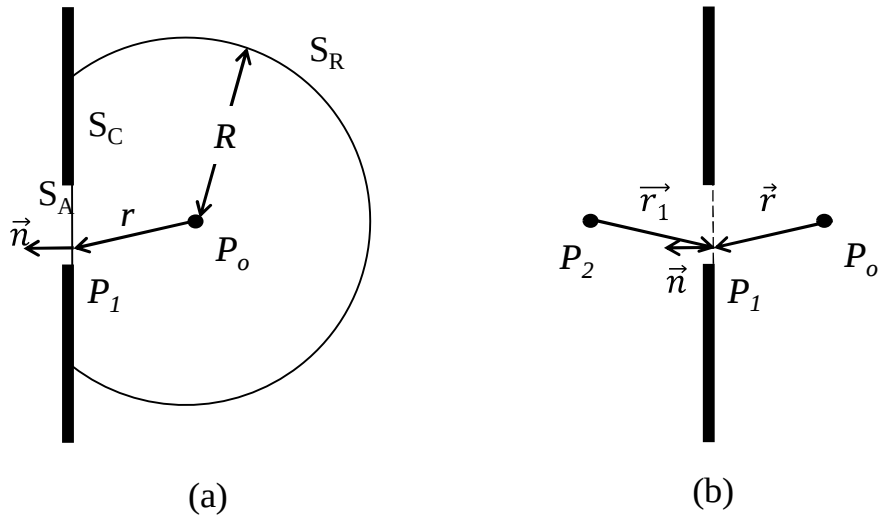

Figure 3-2: (a) Kirchhoff formulation of diffraction by a plane screen and (b) a point source illumination of a plane screen.

3.3 The difference between 2D and 3D diffractions

In order to avoid the expensive finite difference forward modelling in 3D, an investigation of the difference between the relative strength of diffracted to reflected signals in 2D and 3D data was made. The result will help us to differentiate between the outputs of our 2D forward modelling to 3D "real world" diffraction amplitude response.

Waves propagating in 2D and 3D media have different characteristics. Not only the geometrical spreading is different for these two situations but the shape of the waves generated by the same source type is also different. In particular, waves in 2D media have a "tail" following the wavefront unlike waves in 3D media. These differences can be expressed mathematically by Green's functions *G* for the wave equations

$$\nabla^2 G - \frac{1}{v^2}\partial_t^2 G = -4pd\left(r-r'\right)d\left(t-t'\right), \tag{3-12}$$

$$G\left(r,t,r',t'\right) = \frac{2H\left(v\left(t-t'\right)-\left|r-r'\right|\right)}{\sqrt{v^2\left(t-t'\right)^2-\left|r-r'\right|^2}}, \tag{3-13}$$

in 2D and 3D, respectively and

$$G\left(r,t,r',t'\right) = \frac{d\left(\left|r-r'\right|-v\left(t-t'\right)\right)}{v\left|r-r'\right|}, \tag{3-14}$$

where H is the Heaviside step function, δ is the Dirac delta function, r, r' denote location, and t, t' denote time.

To quantify the differences between waves in two- and three-dimensional media, we numerically compute seismograms for waves reflected and diffracted from a line segment in 2D and a surface with edges in 3D using the far-field Kirchhoff diffraction formulae —the bases for Kirchhoff migration (Scales, 1997), respectively:

$$\psi(r,t)_{2D} = \int \frac{\cos\theta}{2\pi R v}\partial_s^{\frac{1}{2}}\psi(y,s)\Big|_{s=t-R/v} dy$$

, and (3-15)

$$\psi(r,t)_{3D} = \int \frac{\cos\theta}{2\pi R v}\partial_s\psi(y,s)\Big|_{s=t-R/v} dy$$

. (3-16)

The above expressions relate the value of wavefield y at (r, t) to integrals of the wavefield along the line/surface acting as the reflector and diffractor. y can denote any quantity that satisfies the wave equation. R denotes the distance between the receiver located at x and the diffraction point y. q is the angle between the normal to the side that acts as a specular reflector and direction from y to x. The symbol $\partial_s^{\frac{1}{2}} y$ denotes the half derivative defined by the following expression:

$$\partial_s^{\frac{1}{2}} f(s) = \frac{1}{\sqrt{p}} \frac{\partial}{\partial_s} \int_{-\infty}^{s} \frac{f(s)}{\sqrt{s-s}}\, ds \ . \qquad (3\text{-}17)$$

The wavefield along the reflector/diffractor is taken to be an incident wave generated at the source—a wavelet convolved with the appropriate Green's function. This approach effectively ignores the reflection coefficient. Since I am interested in comparing only the relative strength of the diffracted signals to specular reflections for the two cases, the effect of the reflection coefficient would cancel out and therefore can be ignored.

To investigate the relative strength of diffractions to reflections, the above integrals are numerically computed using a model consisting of a line segment (2D case) and a rectangular surface (3D case), in a medium with a wave velocity of 1600 m/s as described in Figure 3-3. Figure 3-4 shows the shot records obtained from 30 receivers and scaled by the maximum amplitude of the reflected waves. Figure 3-5 shows the difference between the two- and three-dimensional wave propagation; the main difference is the presence of a "tail" behind the two-dimensional wavefronts. This "tail" results in a shift of the amplitude of the diffracted signal on 2D data; however, the difference between the maximum and minimum of the diffracted wavelet on the scaled shot records shows that the two- and three-dimensional cases result in the same relative strength of diffracted to reflected signals.

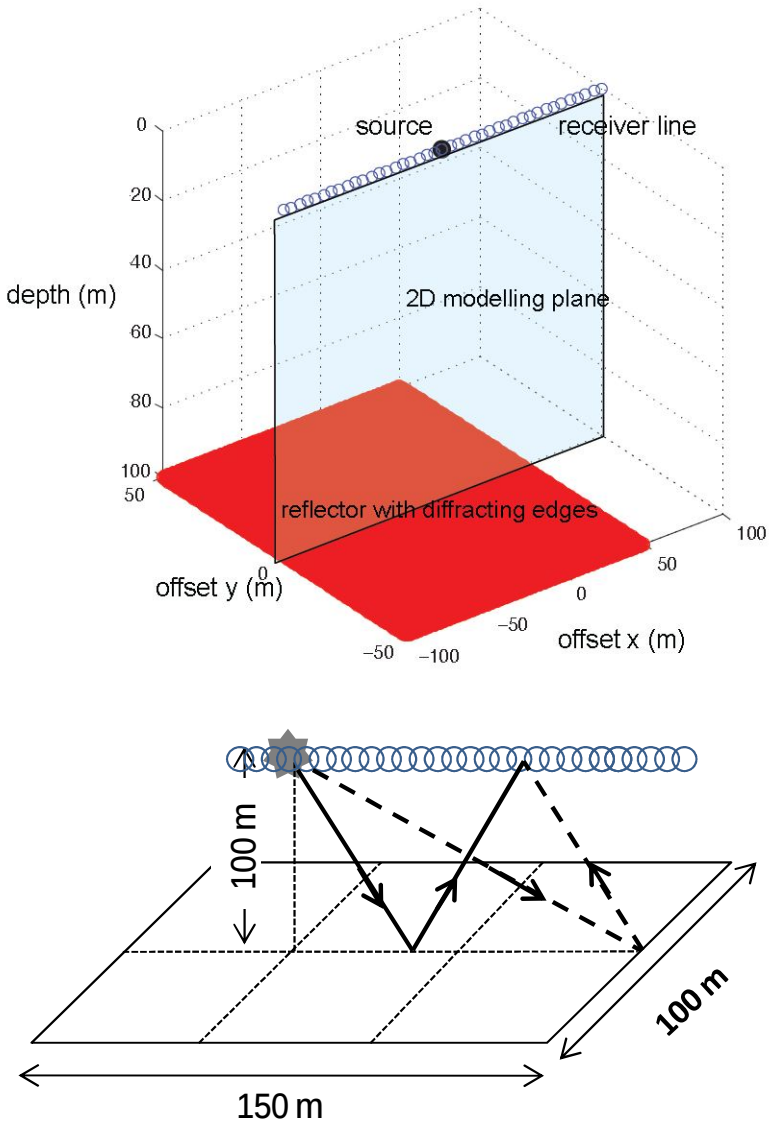

Figure 3-3: (Top) A schematic showing the geometry of the 2D model (light blue plane), and the 3D model (red rectangular surface). (Bottom) A diagram of the reflected (solid line), and diffracted (dashed line) rays.

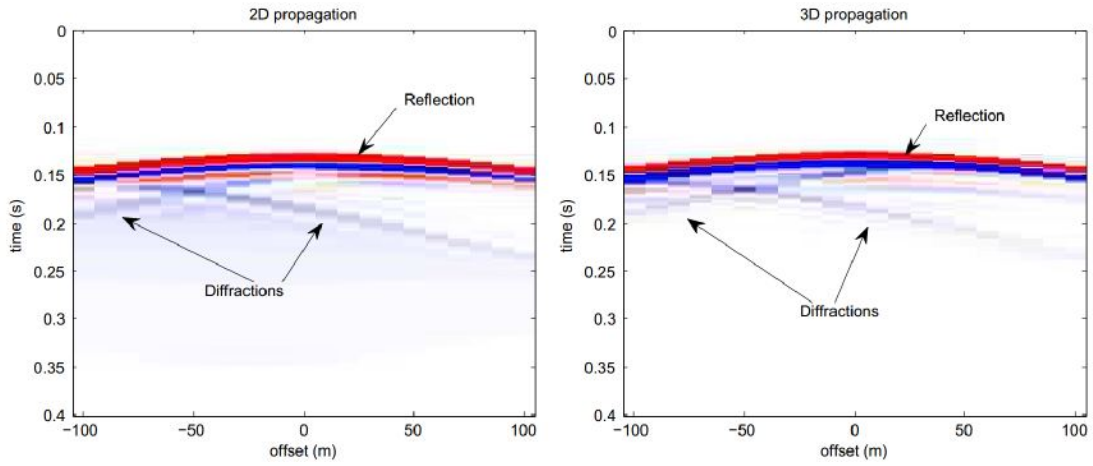

(a) (b)

Figure 3-4: Synthetic shot records for the diffractor/reflector for waves governed by the (a) 2D, and (b) 3D wave equation.

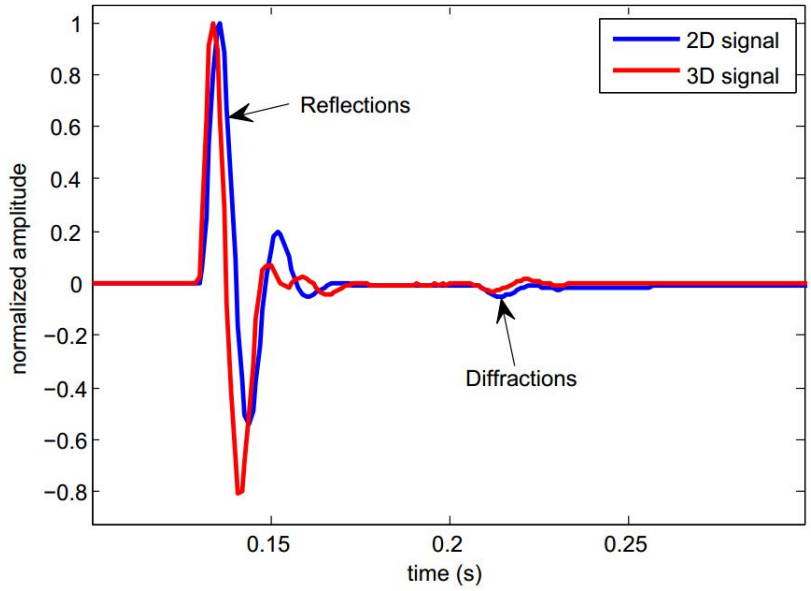

Figure 3-5: Two traces scaled to the same maximum amplitudes corresponding to 2D and 3D wave propagation.

3.4 Diffraction imaging in seismic exploration

The study of diffracted waves in exploration seismology has a long history, Krey (1952) showed the importance of diffraction and demonstrated for the first time how diffraction events can be used to identify faults in seismic records. Seismic diffraction characteristics have been extensively studied on both synthetic and field seismic data. Trorey (1970) derived the response of a point source diffraction from an arbitrary acoustic subsurface and studied the diffraction properties using zero-offset sections and non-zero separation of source and receiver (Berryhill, 1977; Trorey, 1977)

Geological discontinuities, such as small throw faults, fractures, cracks, or even fluid contact terminations are usually characterised in seismic data by diffractions (Pant et al., 1992; Papziner and Nick, 1998). Vermeulen et al. (2006) stated that:

> "*Diffractions are more direct indicators of discontinuities than coherency anomalies since they are coherent events with very specific signatures that cannot be created by noise*".

Therefore, diffractions can be considered as a direct indicator of such geological discontinuities and be used as a tool that aids the interpretation process.

Many researchers have paid attention to the importance of seismic diffraction imaging in order to increase the image sharpness and extract more information (Moser, 2011). Due to the small amounts of diffracted energy compared to reflection and refraction, a successful detection of the diffracted waves on seismic data depends mainly on the ability to extract them from the total wavefield. Several methods have been proposed in the literature to separate the diffraction events from the specular reflections and to use them for high-resolution structural imaging and velocity analysis. Describing the difference in kinematic dynamic properties between diffraction and reflection, Landa et al. (1987) presented a method for diffracted wave detection applied on common-offset sections. They used a two-dimensional model of a right-angled wedge to describe the main properties of diffraction waves as shown in Figure 3-6. In this figure the source and receiver are located at X_S and X_R respectively, and X_{CMP} is the common midpoint. The half offset is given by h, and X_D, Z_D are the coordinates of the diffraction

point. X_B denotes the termination point of the reflected waves. Their method utilises the traveltime, amplitude and phase characteristics of diffracted waves to identify the diffracted energy by correlation between tracts on the chosen observational plane. Working on a common-offset plane, the data is analysed for different curves to find the closest curve to the traveltime curve of the signal, where the diffracted traveltime curve is given by

$$t_D = \sqrt{t_\circ^2/4 + (\varepsilon + h)^2/v^2} + \sqrt{t_\circ^2/4 + (\varepsilon - h)^2/v^2}\,, \qquad (3\text{-}18)$$

where $t_\circ$ is the two way traveltime between the diffraction point and its projection on the line of observation, and v is the velocity of the medium.

Then compute a semblance coherance measure for various values of the unkown parameters $t_\circ$, ε, v, a function along the diffraction curve. The highest semblance value corresponds to the best parameter estimated and is related to the location of the diffraction. The output is a diffraction (D-) time section similar to the conventional stacked section. Using a similar concept, Landa and Keydar (1998) proposed to use scattered/diffracted waves and D-section images for detecting local heterogeneities with the use of time-lapse techniques. The method is based on constructing D-sections from two successive seismic surveys acquired over the area of interest and then comparing the images obtained by subtracting one D-section from the other. Anomalies that remain on the differential D-section should be related to scattering objects produced during the time between the two surveys.

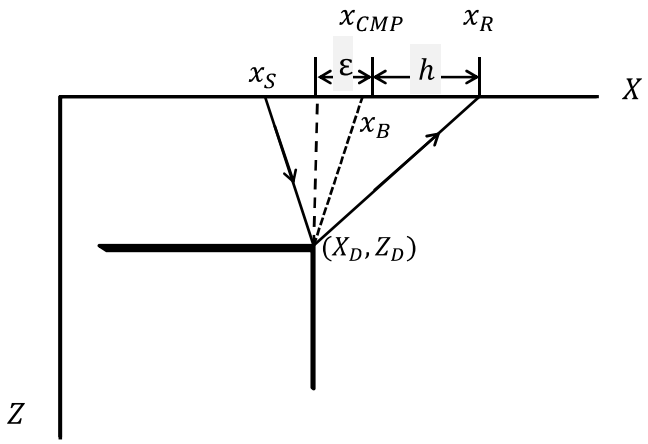

Figure 3-6: The model of a 2D right-angled wedge (After Landa et al., 1987).

Kanasewich and Phadke (1988) described a similar technique, which takes into account the traveltime and amplitude characteristics of the diffracted waves. They proposed a workflow that performs stacking over diffraction hyperbolae analogous to common-depth-point stacking (CDP) and produces a diffraction stack section on what they called a common-fault point (CFP) section. The CFP section not only shows diffractions from fault edges but also those from other geologic features with impedance discontinuities such as reefs, unconformities, salt domes and so on.

Khaidukov et al. (2004) proposed diffraction based imaging algorithm as a supplement to reflection imaging. Exploiting the moveout difference between reflections and diffractions they focused the reflection on its imaginary reflection source to mute it out then de-focused the energy and applied a diffraction stack to the shot gather, now with mostly diffracted energy. Ultimately, two images can be provided: the reflectivity image with the main reflection events and the image comprising the diffracted events that includes small, yet important structures.

An interesting approach for coherent summation of diffracted events and creation of an image containing mainly diffraction energy is presented by Berkovitch et al. (2009). The method uses a new time correction formula based on the multi-focusing method (MF) proposed by (Berkovitch et al., 1994) and described by Berkovitch et al. (1998), Landa (2007), and Berkovitch et al. (2008). The moveout correction does not require knowledge about the subsurface and is valid for arbitrary observation geometry. The MF method constructs a zero-offset section by stacking traces that could belong to different CMP gathers, wherein each trace is computed from pre-stack traces located arbitrarily around an imaging position. Thus, the MF super-gather exceeds the CMP fold by at least one order of magnitude, which in return allows the imaging of weak seismic events, such as diffractions, that cannot be seen in conventional processing. Unlike the conventional CMP stacking, the MF process requires more general moveout corrections and its moveout equations are based on the spherical representation of wavefronts.

The plane-wave destruction filter introduced by Claerbout (1992) was proposed by Fomel (2002) as tool to remove the strong coherent events with continuously variable slopes. Taner et al. (2006) used the simulated plane-wave section method (Taner, 1976)

to separate and image diffracted events in full pre-stack data. They showed that by applying the plane-wave destruction filter they can suppress specular reflections and produce plane-wave sections of diffractions. The separation workflow starts by performing plane-wave decomposition for each shot record to obtain a common p section for the entire line. A plane-wave destruction filter is then applied to produce a section containing mainly diffraction energy and residual specular reflection energy. After that, the section is sorted back to a shot domain and an inverse Radon transform is applied. These records now can be used for velocity analysis and produce a pre-stack migration image emphasising sharp discontinuities where more of the scatter objects, which was masked on the conventional migration section, are observed on the diffraction section, as shown in Figure 3-7.

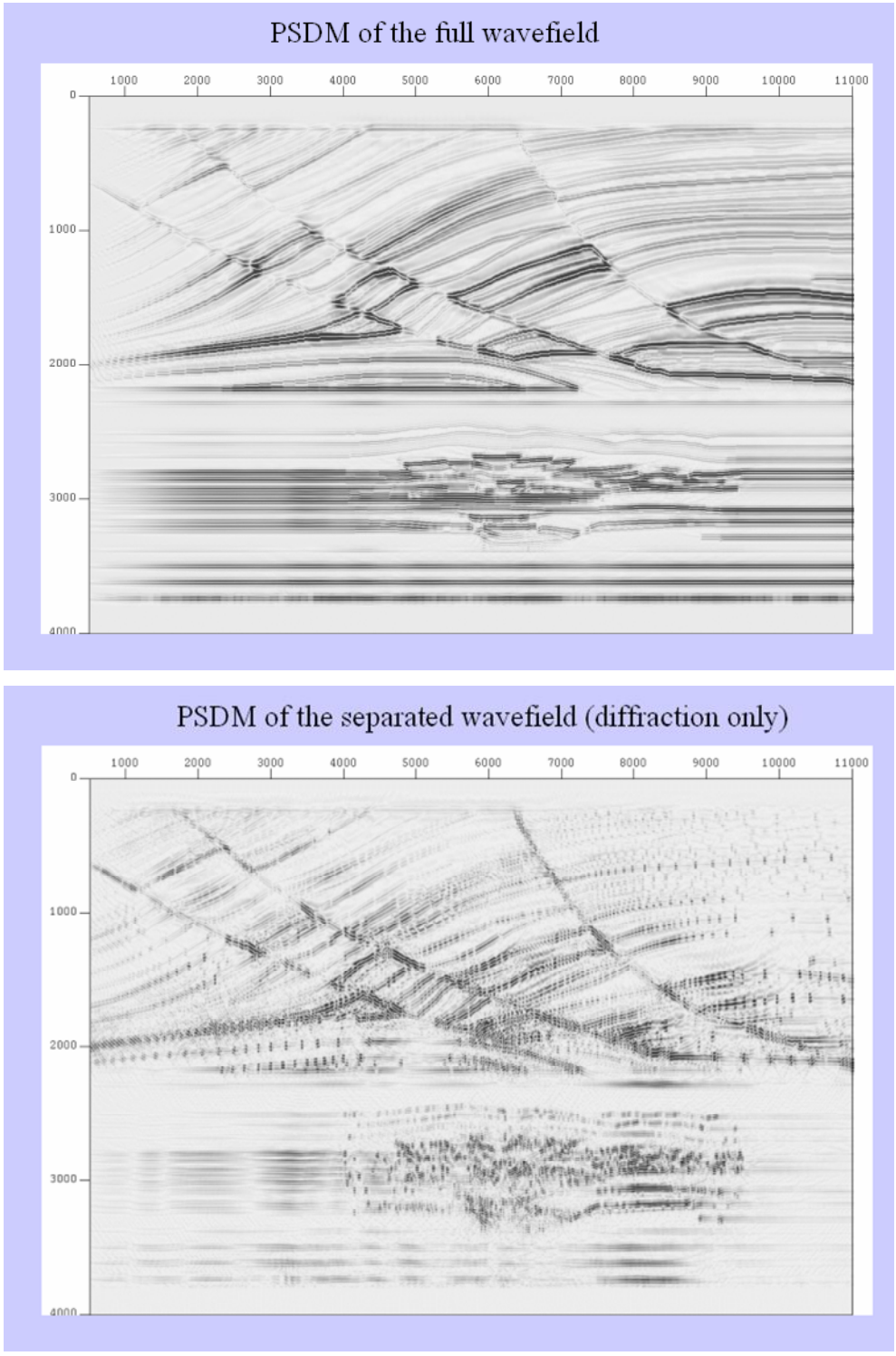

Figure 3-7: (top) Pre-stack depth migration of the full wavefield and (bottom) diffraction components only (After Taner et al., 2006).

Bansal and Imhof (2005) examined several workflows on synthetic and real seismic data to enhance diffraction events over reflections in the pre-stack domain. They found that using the eigenvector filter was the most effective technique to preserve diffractions and suppress reflections. Vermeulen et al. (2006) applied diffraction imaging to enhance fault images by combining diffraction analysis with coherency attributes.

The use of diffraction events and correctly identifying them can be very important for velocity estimations. Fomel et al. (2007) suggested the use of diffractions to perform semblance-based post-stack velocity analysis. They proposed a data processing approach by using a plane-wave destruction filter to remove reflection events and preserve diffracted waves, this time in a stacked section (e.g., dip moveout correction and the use of nearest-offset stacks). Harlan et al. (1983) separated diffractions from the data by focusing with a slant stack then subtracting it from the data. They used the remaining diffractions for velocity estimation.

The post-migration dip-angle domain has gained more attention lately as a tool that can show high quality images of complex structures (Audebert et al., 2002; Reshef et al., 2005). Landa et al. (2008) and Reshef and Landa (2009) proposed in their works a technique that utilised the post-migration dip-angle domain in order to extract and analyse diffracted events and use them for velocity estimations. The reflections after migration in the dip-angle domain will have concave-shaped events while diffraction events come with the correct velocity.

3.4.1 Diffraction in time lapse

As we have seen earlier, several methods have been proposed in the literature to separate diffraction events from specular reflections. Seismic time-lapse analysis can also be utilised as a complimentary tool that can extract diffractions from the total wavefield. In a sequence of seismic surveys repeatable recorded signals from any constant subsurface features, including diffractions, can be eliminated. The diffraction energy that is affected by changes at the reservoir level can be imaged using the method described in the next chapter. Thus, application of an imaging technique aiming to detect presence of edge diffraction to the difference volume will give us contours of the area affected by those changes. This can have several important practical applications,

such as estimation of the horizontal extent of the CO_2 plume in carbon sequestration projects.

3.5 Conclusions

In this chapter general information about diffraction was discussed, which included a brief history showing the rise of diffraction theory from early observation by Grimaldy in the 1600's to the modern theory of diffraction. The importance of diffractions in seismic imaging was described because they originate from important structures that cannot be detected with the conventional reflection methods. Many researchers have paid attention to diffraction analysis showing that instead of dealing with diffraction as noise and attenuating it, it can be extracted and analysed to obtained additional information relating to the reflection seismic models. Using diffraction analysis not only increases the resolution of imaging small-scale heterogeneities, but it can also help us implement velocity analysis in both pre-stack and post-stack domains. Finally, we numerically investigated the relative strength of the diffraction signal in 2D and 3D. The result shows that the relative amplitude of edge diffractions and specular reflections in 2D and 3D are similar. This is important as it gives us an opportunity to use 2D FDTD modelling for our studies, which is much cheaper compared to 3D FDTD.

4. Chapter 4 - DIFFRACTION IMAGING METHODOLOGY

4.1 Introduction

In this chapter, an explanation of the proposed technique is illustrated showing the workflow used to extract the diffracted waves for both 2D and 3D seismic data. The term “edge diffraction” in this work means the diffraction produced from an edge or a corner of an edge, “line diffraction” means diffraction caused by linear objects, such as narrow channel, and “tip diffraction” is for the diffraction caused by a point-like scatterer (small-scale heterogeneities). Edge and tip diffractions are produced from the edge and tip of a smooth reflecting surface and are mainly generated at the termination of reflectors caused by faults, fractures. Each type can be distinguished by its different characteristics. The tip diffracted waves are diffracted in all directions. In contrast, the diffraction caused by an edge is governed by Keller’s law of diffraction (Keller, 1962) where the diffracted wave front lies on a cone with the axis aligned with the edge. Unlike tip and line diffractions, the diffraction waveforms produced by the edge diffractor exhibits a reverse polarity on either side of the diffraction traveltime curve (Trorey, 1970; Harlan, et al., 1983). The 180° phase change produced from the edge diffraction is utilised as the principal feature that can distinguish edge diffractions from the total wave field component. This approach can be applied on both 2D and 3D datasets, each in a different work flow as described in the following sections.

4.2 Diffraction image construction

From the kinematic point of view, the detection of diffracted waves in this method is based on the diffraction summation scheme that is commonly used in Kirchhoff zero-offset time migration (Bancroft, 2007). However instead of constructing reflections as an envelope of the secondary Huygens’ diffractions, the proposed algorithm intends to use image real diffraction events in post-stack domain.

Let us consider a scatter (red point) in Figure 4.1. The zero-offset two-way traveltime to and from the scatter point to the surface point x_i is denoted by t_i, where t_o, denotes the traveltime from and to the surface projection x_o of the scatter point. From the

geometry in Figure 4.1, the zero offset travel of the output trace t_i can be computed using the double square root (DSR) equation (4.1).

The process assumes an output sample (red point) defined by t_o, and then sums the samples from all available input traces along the diffraction-time curve that is associated with the red point and assigns the value to the apex point of the curve. This procedure is repeated for every output sample in the output data. If a diffractor exists, the signal will add up at the apex and collapse the diffraction into a point; whereas the noise will cancel out.

$$t_i = \sqrt{t_0^2 + \frac{4\left(x_i - x_0\right)^2}{v^2}} \,. \tag{4.1}$$

The velocity v used in equation (4.1) is the stacking velocity obtained from velocity analysis of the reflection data.

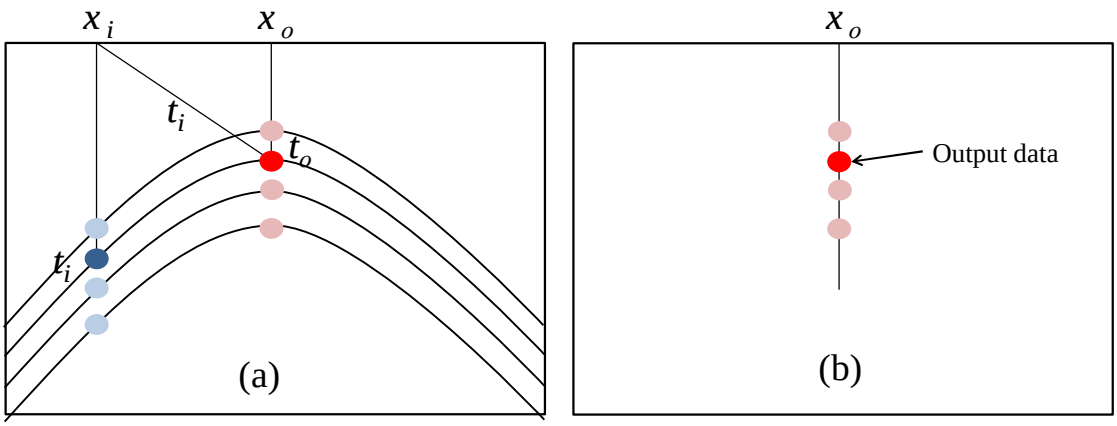

Figure 4.1: Illustrations of basic Kirchhoff zero-offset time migration (a) summing the data samples along the diffraction-time curve for every sample in the data and (b) the output data after diffraction summation where the blue point is collapse to the apex of the hyperbola (red point) using equation (4-1).

The final image is then produced by measuring the coherency of the data using the semblance function calculated in a given time window along the traveltime curve

defined by equation (4.1). The semblance function S, which normalised the output-to-input power ratio (Taner and Koehler, 1969) is given by:

$$S = \sum_{t=-m}^{+m} \left(\sum_{i=1}^{N} f_{it(i)} \right)^2 \Bigg/ N \sum_{t=-m}^{+m} \sum_{i=1}^{N} f_{it(i)}{}^2 . \qquad (4.2)$$

Equation (4.2) defines a normalised ratio of energy of the sum of the traces to the sum of the energies of the individual traces. The inner summation of the samples $f_{it(i)}$ is performed for all traces (index i) at the time (index t) given by equation (4.1), and the outer summation is performed over a given time window of width $2m$. N is the number of traces in the selection.

The image produced emphasises the diffraction energy depicted by the high semblance value at the diffractor location. This approach (the semblance based image) is based on the work presented by Landa and Keydar in 1987. Therefore, following their work I named the output image *D-section* (diffraction section). However, the algorithm in this research utilises the phase-reversal property of the edge diffraction and uses it as a criterion to separate the edge diffracted wave from the total wavefield component in post-stack domain.

Using semblance in *D-section*, the weak diffraction energy that is masked by the dominant specular reflections becomes more pronounced and easy to spot. Working in a post-stack domain makes the method robust and more efficient. However, this means that the data is stacked over common midpoint (CMP), which enhances reflections over diffractions. Therefore, it is important to have a dip move-out (DMO) correction applied to the input data to enhance the appearance of diffractions as illustrated in the following chapter.

4.3 Phase-reversal phenomenon in edge diffraction

As mentioned earlier, the traveltime curve of a wave diffracted from an edge has 180^o phase shift across the intersection of the diffraction and the reflection traveltime curves. For illustration, Figure 4.2 shows a synthetic data with edge diffraction at the termination of a line segment. The phase-reversal across the diffraction curve apex is indicated by an arrow. In this case a simple summation would tend to partially cancel the contributions from the two sides of the edge diffraction curve. Therefore, to avoid

losing the diffraction energy during the imaging process, the diffracted time curve is divided into two parts based on the horizontal offset from its apex: the off-end part from the reflector with one polarity and the part below the reflector (the shadow zone) with the opposite polarity. Using the phase-reversal feature in equation (4.1) allows us to separate edge diffractions from other wavefield components and distinguish the diffraction produced from an edge from diffractions produced by a symmetric linear object (e.g., a narrow channel or a wedge).

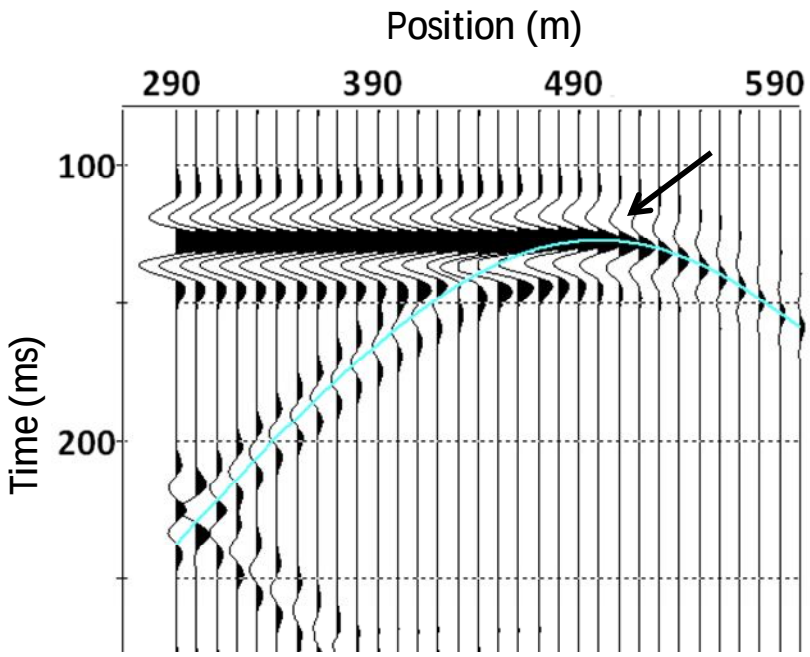

Figure 4.2: A common-offset gather from a finite-difference synthetic model of edge diffraction. The locations of the midpoints are in the direction across the edge. The arrow indicates the termination of reflections where the diffraction occurs with half of the reflection amplitude. The edge diffraction curve exhibits a phase-reversal below the reflection (the shadow zone). The cyan line shows the correspondent traveltime curve; one can see that it follows the peak of the wavelet on one flank and trough on the other.

As mentioned before, the detection method is mainly focused on edge diffractions. However, the seismic wavefield in a complex area will likely also contain tip diffractions (Klem-Musatov, 2008). Therefore, for each dataset one can compute two sets of D-sections: one corresponding to tip diffractions and one to the edge diffractions, taking into account the phase-reversal. Both types of the ***D-sections*** can be useful for interpretation.

4.4 3D diffraction: *D-volume*

In order to expand the method to a 3D post-stack (zero-offset) case, I need to replace the diffraction traveltime hyperbolae with diffraction hyperboloids given also by equation (4.1) but with $(x_i\text{-}x_0)$ being a 2D vector. Furthermore, diffraction from an edge or a linear segment is given by a superposition of signals along such hyperboloids. For such diffractions, the focus is only needed on a portion of each hyperboloid that is contributing to the total envelope of the superimposed hyperboloids along the edge/segment. To this end, I split the hyperboloids into a range of sectors and run multiple iterations, each corresponding to different possible orientation of the edge/segment diffractor (Figure 4.3). The following workflow is used to image the diffractors in 3D:

1. Divide the full range of possible directions of the edge/linear diffractor into several intervals ($\Delta\alpha$) (Figure 4.4). For every direction of the analysis we compute D-volumes using steps a–c.

   a. For every image point (trace and t_0), compute the diffracted wave traveltime hyperboloid. Then for each trace compute the lateral offset h from the line passing through the image point in the direction orthogonal to the direction of the analysis (expected orientation of the diffractor). Then exclude the parts of the hyperboloid where h exceeds a certain threshold h_0. This offset limit h_0 is a trade-off parameter between the signal-to-noise ratio and the lateral resolution. The effect of this parameter is illustrated in Chapter 5. A good proxy for this parameter is the Fresnel zone.

b. In case of edge diffraction, flip the polarity of the signal along the line passing through the image point in the direction of the analysis.

c. Compute the semblance value using equation (4.2) along the part of the hyperboloid constructed in step 1a.

2. For every image point using all of the D-volumes (corresponding to different orientations of edge/segment diffractors), estimate the maximum semblance and the corresponding azimuth.

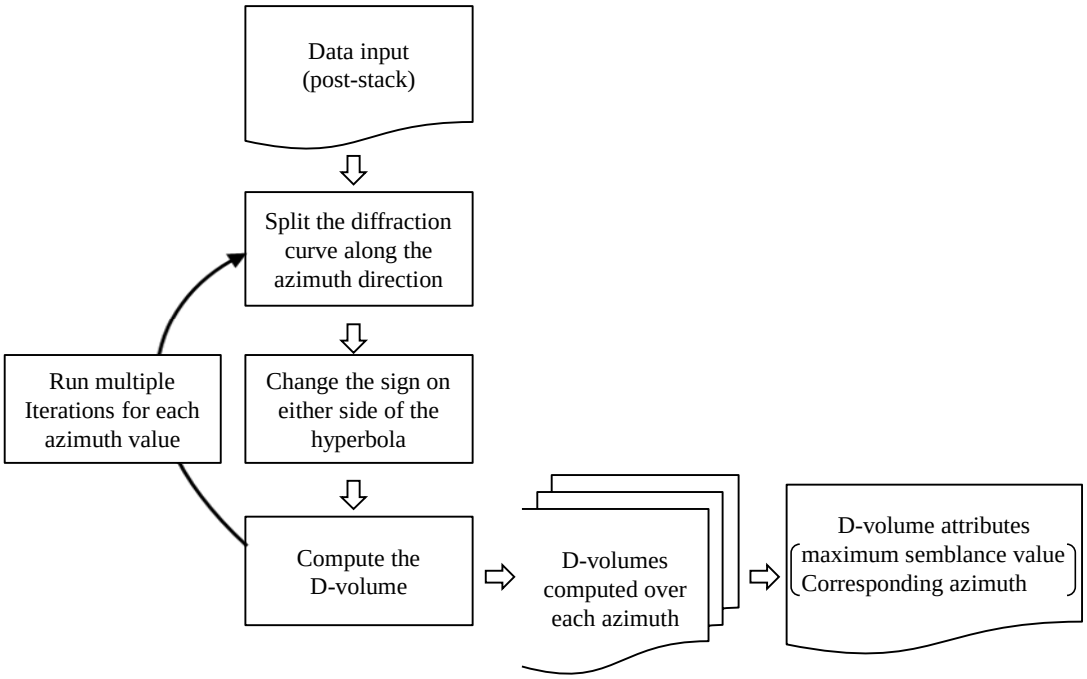

Figure 4.3: The above flow chart illustrates the process of computing the D-volume applied on 3D zero-offset/stacked data.

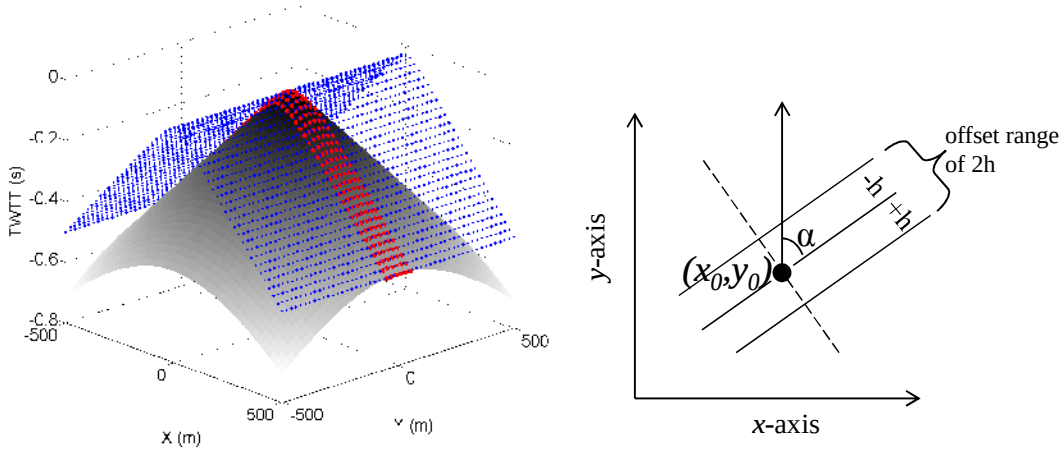

(a) (b)

Figure 4.4: (a) A diffraction hyperboloid (grey) and corresponding direction of the edge diffraction (blue). A limited offset (red) used to compute the D-volumes. (b) A 2D projection of (a) showing the parameters used for D-volumes computations, where α is the azimuth and the dashed line is where we split the diffraction traveltime for phase change.

Unlike the conventional Kirchhoff migration that stacks the full data along the point scatterers' traveltime surface, the proposed algorithm scans over the linear/edge diffractor orientation azimuths and automatically selects a subset data that have the highest semblance value. In the case of linear diffractors, only a small part of this surface contains the signal, the rest is noise. Therefore, this approach allows adaptively selecting that portion of the data that hosts most of the signal. The method proposed here is based on the assumption that the change of phase of the diffraction traveltime curve is occurring at its apex from a horizontal reflector. This is not always the case as the diffraction events could also be produced from edges of a dipping reflector. In this case, the change of the polarity will occur not at the apex of the diffraction hyperbola, but at the "junction" of the hyperbola with the reflection traveltime curve. In other words, the polarity would change in the shadow zone only. However, for small dips and relatively shallow depths, the difference between the apex and the actual point of polarity change would be small compared to the total length of the considered traveltime curve and will be ignored further in this paper. Therefore, this technique will thus be limited to areas without steep dips.

5. Chapter 5 - 2D DIFFRACTION IMAGING EXAMPLES

5.1 Introduction

In order to be able to extract the diffraction energy and produce an image that can successfully focus the edge diffraction, several models have been created to gain more insight into the properties and characteristics of diffracted waves. Seismic diffraction modelling helps us develop a better understanding of the diffracted waves, test the validity of the method and improve the methodology of the algorithm. In this chapter, the diffraction imaging is tested on models based both on the finite-difference seismic forward modelling and small-scale physical laboratory experiments. Another illustration for the diffraction imaging method is provided using ground penetration radar (GPR) data. Finally, a numerical model based on Otway project data is introduced to investigate the sensitivity of the method to detect a relatively small CO_2 plume utilising time-lapse analysis as a CO_2 monitoring tool.

5.2 Numerical model of a simple edge diffractor

A simple numerical model was initially created in order to understand the diffractions produced from an edge. The model consists of a reflector with P-wave velocity of 3300 m/s at 400 m depth and 500 m long in a background velocity of 3160 m/s as shown in Figure 5-1. The seismic data were obtained using 201 receivers and 101 shots with 10 m intervals. Figure 5-2 shows the data computed from the simple model in common offset gather. The diffractors are tangent to the reflection at both ends of the reflector. Notice the clear polarity change between the ‘light’ and ‘shadow’ parts of the diffractions.

The polarity-reversal across the diffraction hyperbola can be observed in different gathers (Figure 5-3). Figure 5-4 shows the same datasets of the simple model in a pre-stack domain with common source and common receiver gathers. When cross plotting these gathers and displaying them in time slices we can see clearly the reverse polarity of the diffractions produced at the termination of the reflector (Figure 5-5). One can notice the significant drop in the amplitude of the edge diffractions and how they are weak compared to the amplitude of reflections.

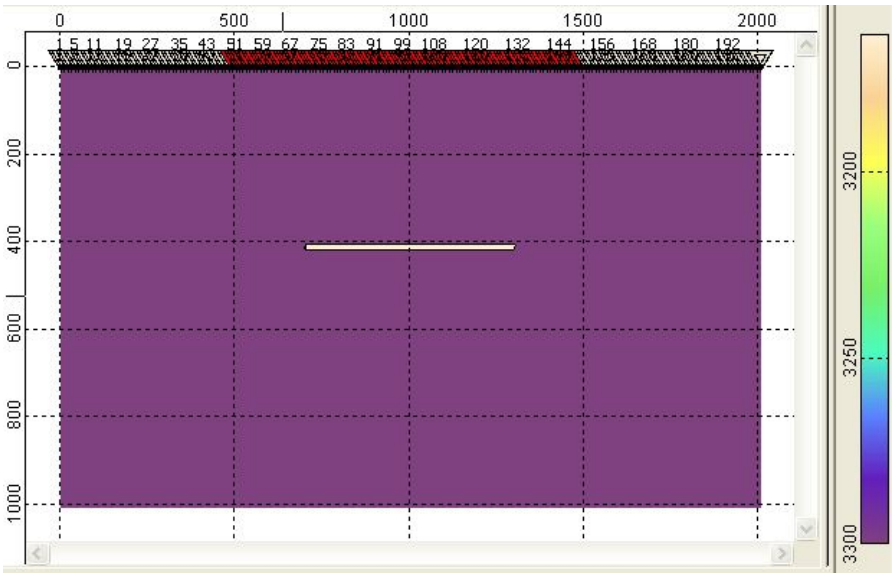

Figure 5-1: A simple cartoon model created to examine the edge diffraction detection technique in uncomplicated case.

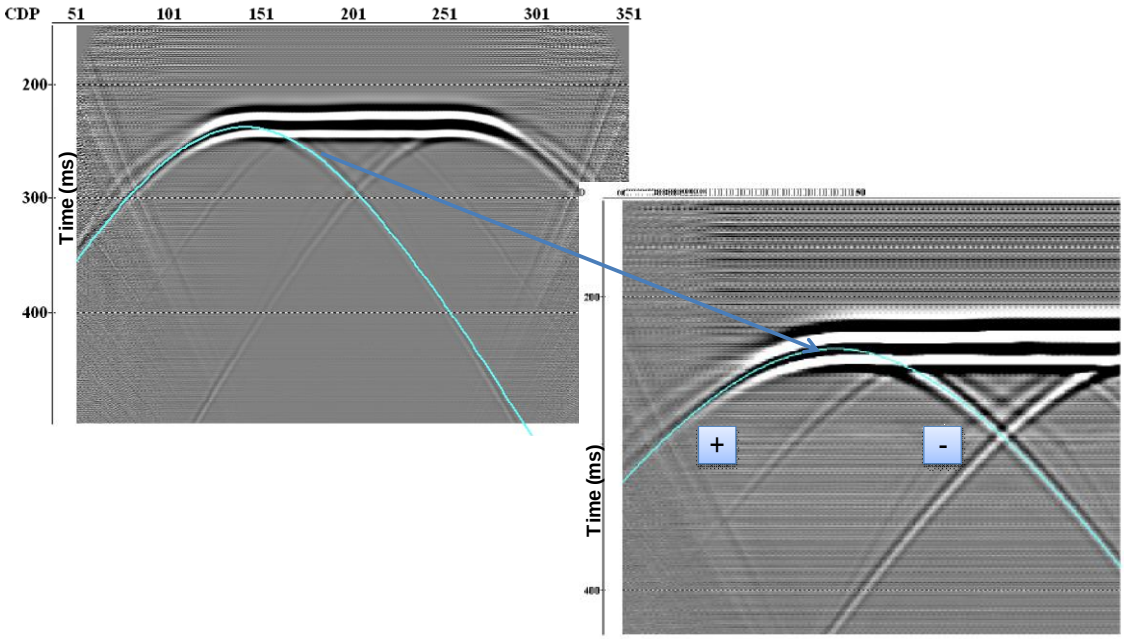

Figure 5-2: A common-offset gather of the data obtained from the simple model. Note the polarity change between light and shadow part of the diffracted wave.

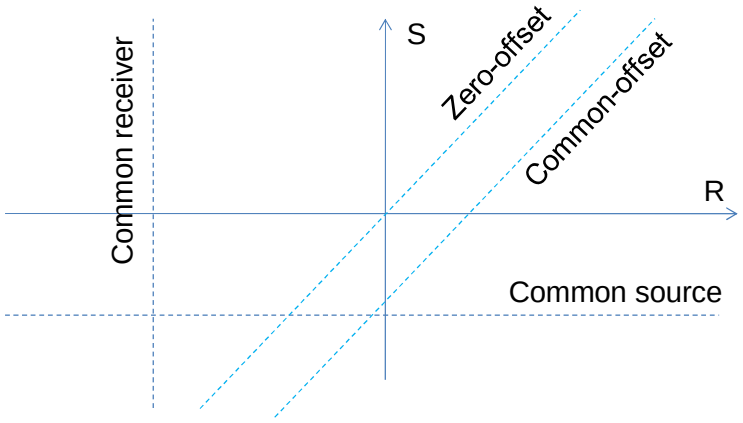

Figure 5-3: A different trace gathers chart showing different domains of trace sorting in seismic data.

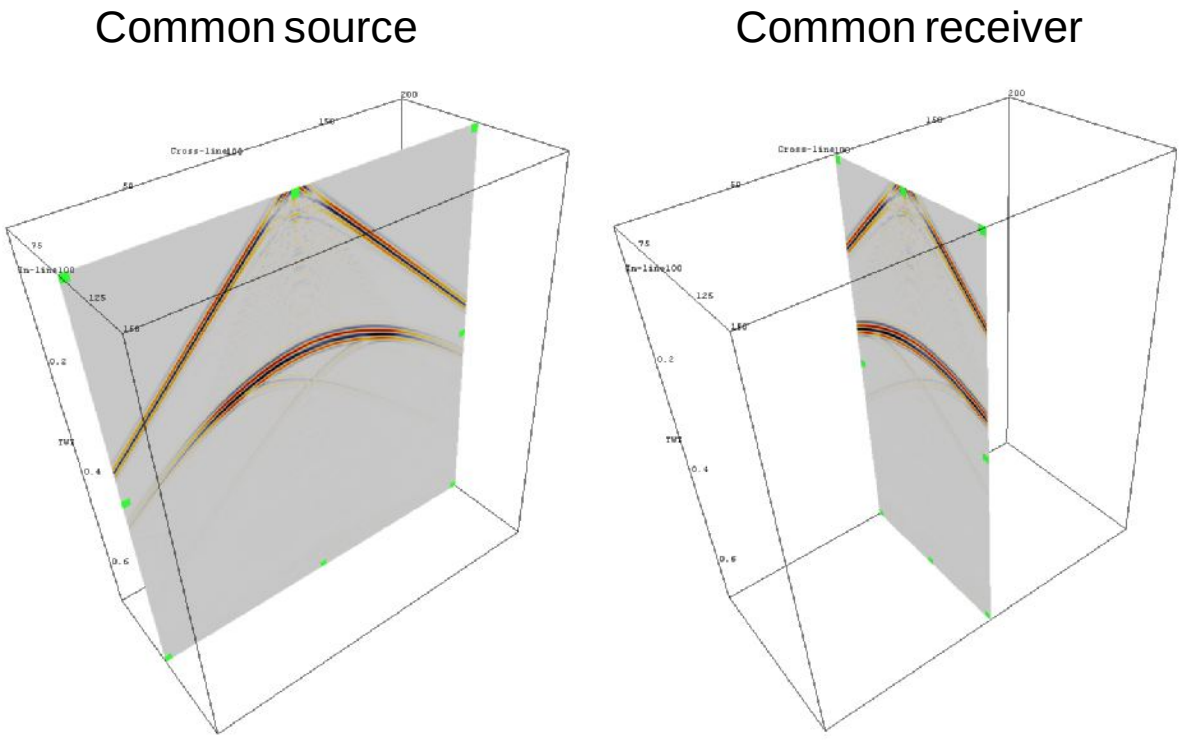

Figure 5-4: A pre-stack domain of the data in different gathers: (left) common source gather, and (right) common receiver gather.

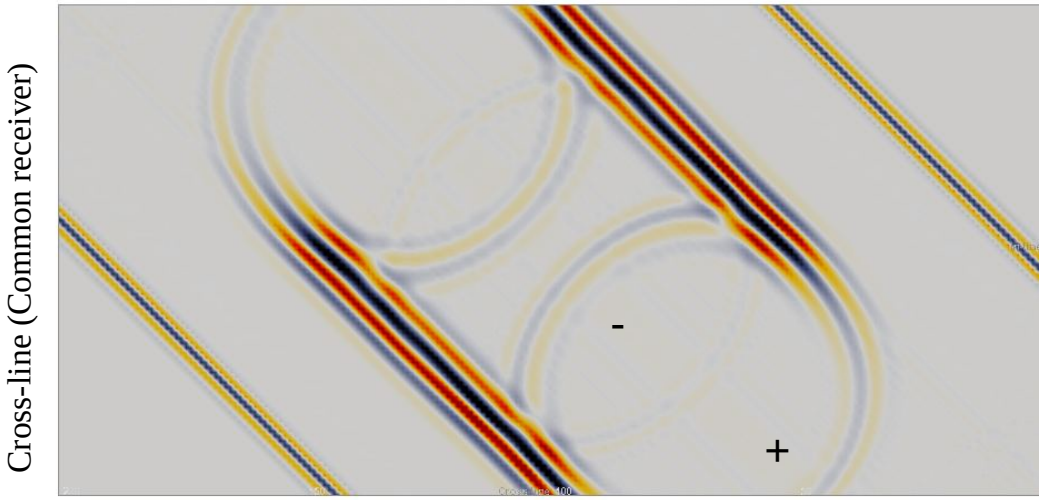

Figure 5-5: The time-slice of cross-plotting common source and common receiver gathers at 274 ms. Note the polarity reversal observed at both ends of the reflector.

Different D-sections have been computed and displayed with respect to the polarity reversal of the diffraction hyperbola. Figure 5-6 shows D-sections computed from the simple diffractor model: (a) shows a D-section computed without taking phase-reversal into account during the summation of the diffraction traveltime. The D-section shows the edge diffraction in red as well the specular reflections. However, considering the phase-reversal in the D-section computation enhances the edge diffraction energy over the reflections and that is clearly seen in Figure 5-6 (b).

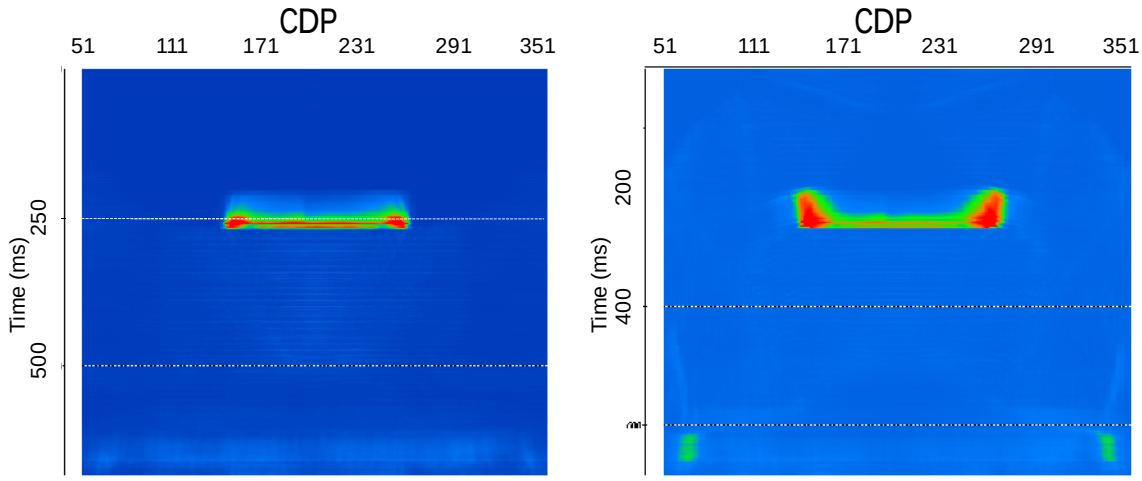

Figure 5-6: A D-section with respect to polarity-reversal: (a) without polarity-reversal consideration, (b) with polarity-reversal consideration where diffraction energy is enhanced over reflections.

5.3 Physical model of the edge diffractor

The aim of the physical modelling is to simulate the response of diffracted wave, and study the behaviour of seismic diffraction at a laboratory scale. The experiment was conducted at the rock-physics and physical modelling laboratory in the Department of Exploration Geophysics at Curtin University. Seismic physical modelling is considered extremely useful in filling the gap between what is described in the theory and what is observed in the real seismic field data. Physical modelling is considered fast and cost effective compared to real earth acquisition. Moreover, it allows us to control a wider range of the experimental parameters.

The source and receiver are two piezoelectric transducers connected to robotic motion controllers that are in turn connected to a work station. The transducers can transmit and receive high-frequency ultrasonic vibrations; each can operate as either the source or receiver. A special program was used to design the survey geometry and define data acquisition parameters then run the survey automatically (Figure 5-7) with precise positioning and movement of source and receivers over the model. The seismic experiment was performed in a water tank using a physical model that consisted of a block of paper-reinforced phenolic. A schematic of the experiment's setup is shown in Figure 5-8.

To simulate a conventional time-lapse surface seismic experiment, two surveys were acquired: the first one was recorded as a baseline survey with just water and then the survey was repeated with the same parameters after placing the paper-reinforced phenolic block in the water tank (Figure 5-9). Each survey consisted of a 2D line with a constant-offset of 30 mm and 150 shots with 2 mm spacing between shot locations. In each source-receiver position the data was stacked 32 times to reduce ringing and increase the signal-to-noise ratio. Figure 5-10 shows the raw data obtained from both surveys, before and after placing the block in the tank, where the edge diffraction produced from each side of the block is clearly observed. One can see that the reflection from the water level is shifted due to the water replacement by the block. Applying a 2D spatial filter (to remove the horizontal reflections) allows us to observe a clear phase-reversal on each side of the diffraction hyperbola as shown in the zoomed Figure 5-11.

This finding supports the results obtained from the numerical simulations where edge diffraction with phase-reversal is observed as well.

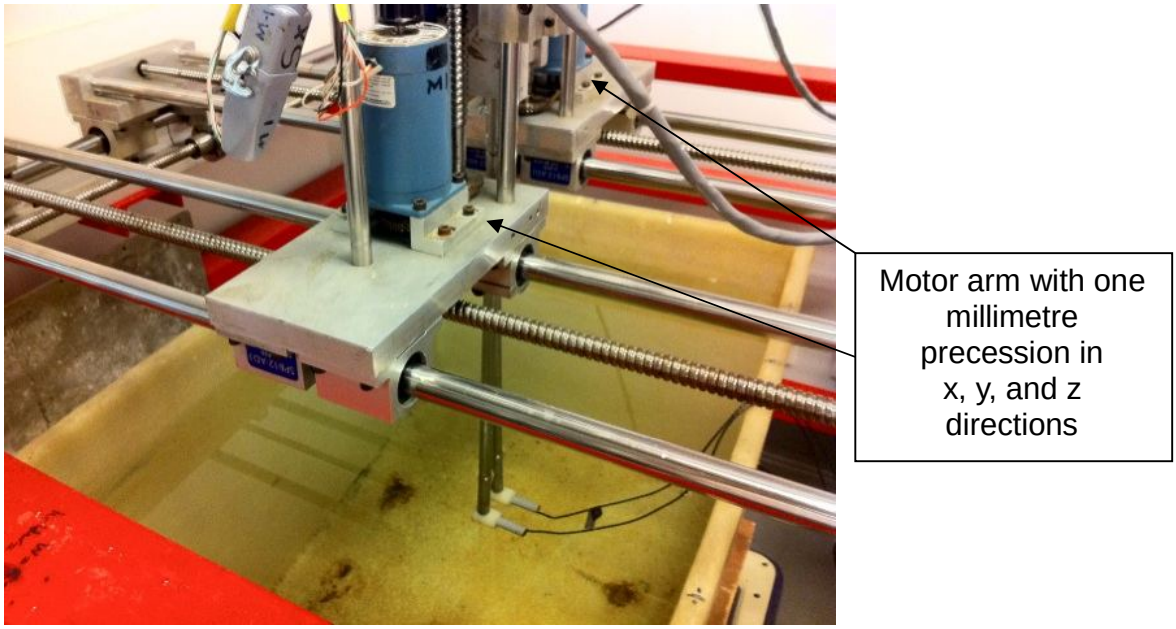

Figure 5-7: The acquisition system used for the physical diffraction modelling. Two transducers are used, which are controlled by two robotic arms for high precision positioning.

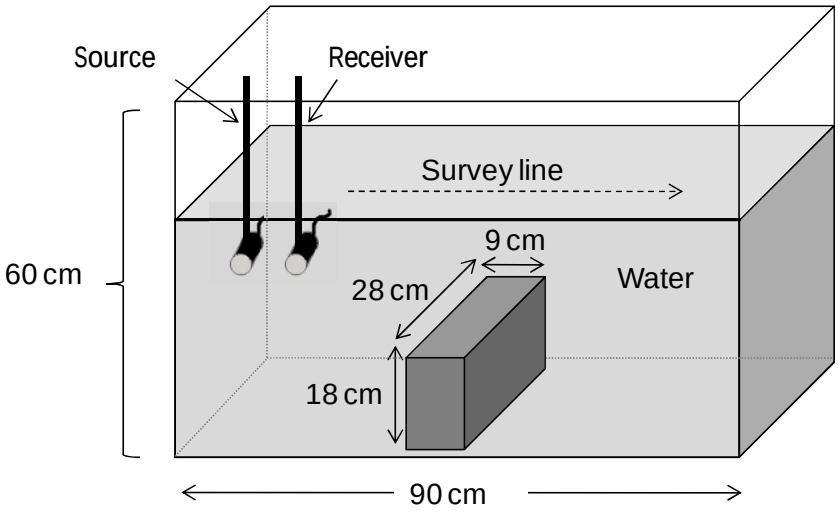

Figure 5-8: The schematic diagram of the physical modelling experiment using the paper-reinforced phenolic block to produce edge diffractions.

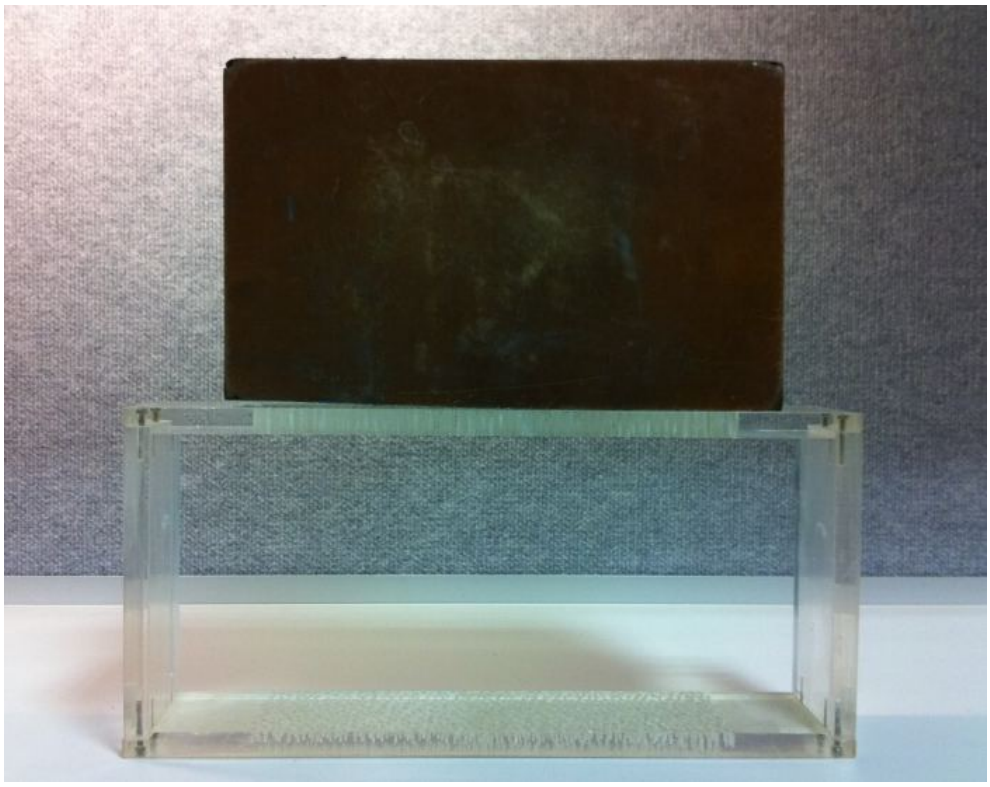

Figure 5-9: The physical model consists of a paper-reinforced phenolic blocked used for the experiments.

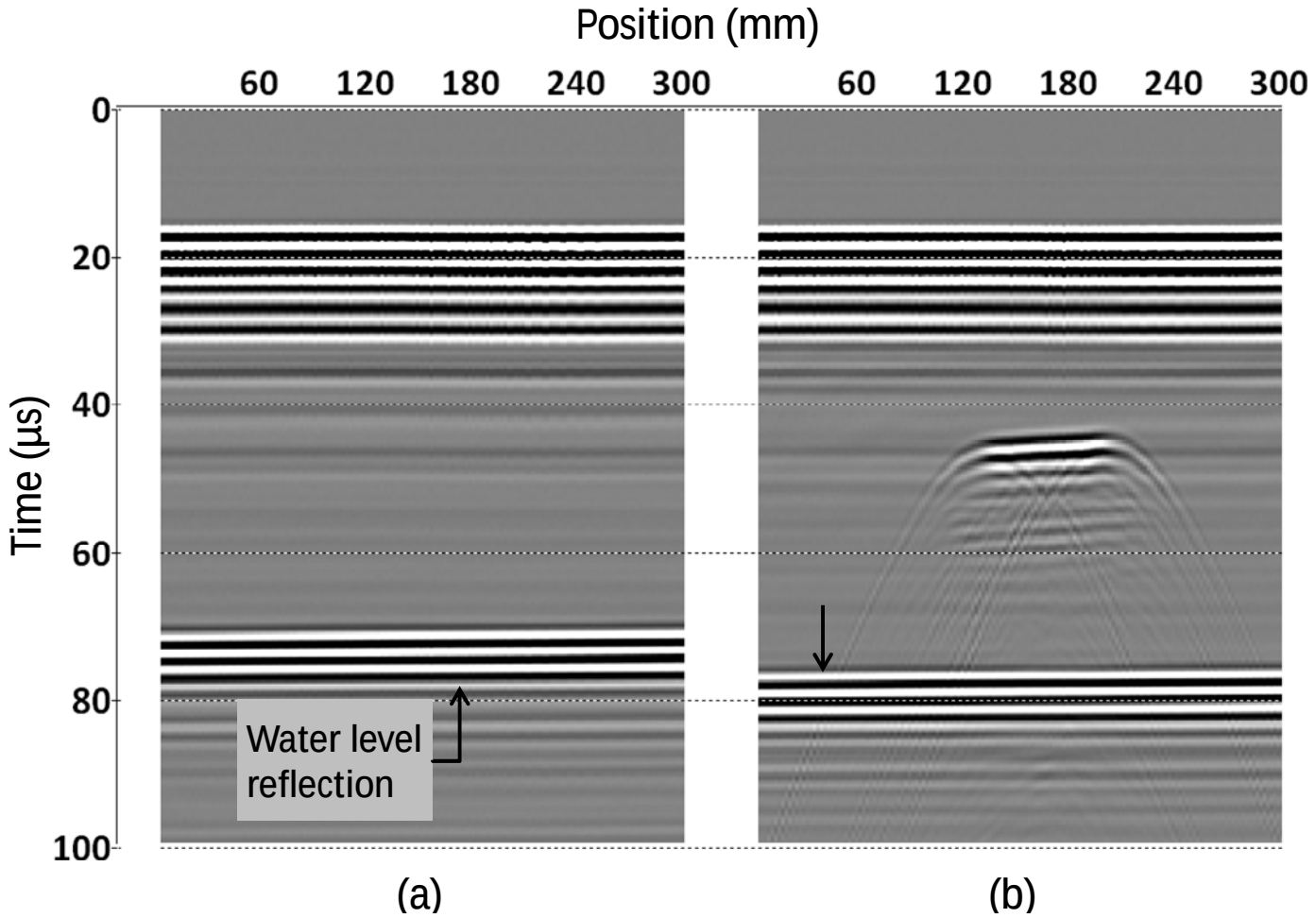

Figure 5-10: The data obtained from the physical modelling experiment: (a) the base line survey with the tank filled with water and (b) the monitor survey after placing the paper-reinforced phenolic block in the tank. Notice the reflection from the water level is shifted due to water replacement by the block.

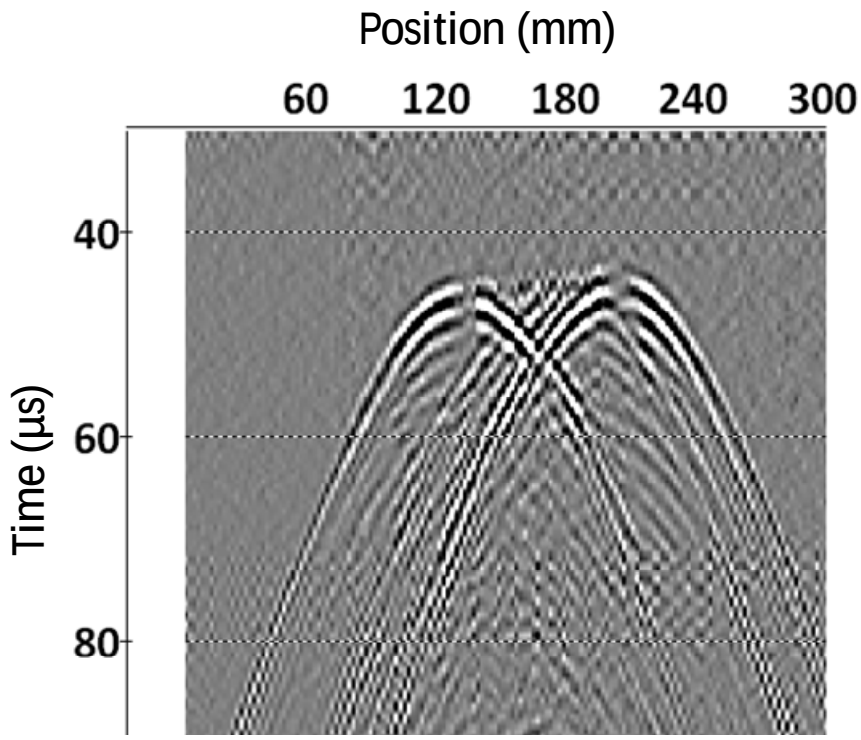

Figure 5-11: Edge diffraction from the block model after applying 2D spatial filtering. Phase reversal at each side of the block can be observed.

Figure 5-12 shows a comparison between the time-lapse data after post-stack time migration, (a) without phase reversal (conventional migration), and (b) with phase reversal consideration, and (c) a D-section of the same data highlighting the edges of the block. The physical model experiment shows that the phase reversal correction substantially improves the focussing of the energy on the edges of the block.

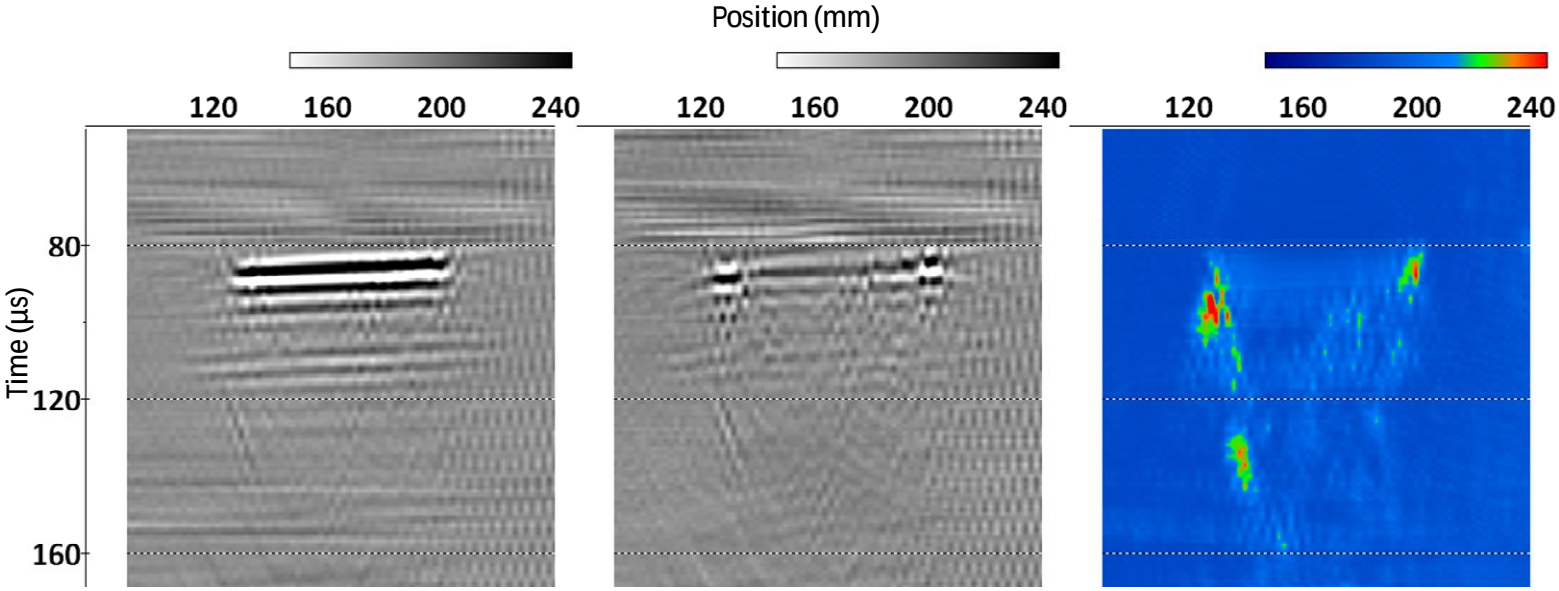

(a) (b) (c)

Figure 5-12: (a) The physical modelling migrated section, (b) the same data after migration with phase reversal correction, and (c) a D-section giving high semblance values at the edges of the block.

5.4 Ground penetrating radar example

Ground penetrating radar (GPR) system is a near-surface geophysical method that uses pulses of electromagnetic waves that radiate from a surface transmitter antenna into the ground. A part of the signal is reflected or diffracted and the time elapsed for the signal coming back to receiver antenna is recorded. Using the reflection and the two-way traveltime (measured in nanoseconds), a cross-sectional GPR reflection profile is created similar to the seismic reflection method (Beres and Haeni, 1991). GPR surveying has been widely applied to a number of engineering and environmental problems.

In this example, the same diffraction detecting method used in seismic data has been applied to zero-offset GPR data. The field data were collected over a fresh water lake using an unshielded GPR antenna system. The frequency of the GPR antenna is approximately 150 MHz. The GPR antenna was placed on a fiberglass boat with 4cm station intervals. Due to inconstant boat speed the spacing between readings is not constant. This in return affects the diffraction traveltime curve.

A part of the survey line was used to compute the D-section as shown in Figure 5-13. In this part multiple hyperbolic diffraction patterns are observed at around 100 ns and below. The migration section in Figure 5-14 was computed using a constant velocity assumption showing that some diffraction events collapse to their position. However, some of those diffractions are not collapsed correctly because of the variation of the interval between traces, which affect the diffraction traveltime curve. Similarly, the high semblance value in the D-section in Figure 5-15 successfully points out the diffraction event locations where some diffractions did not collapse at the right position due to the inconsistency of channels intervals. Other anomalies, mainly located at the lacustrine sediments, can be attributed to a sharp bend in the sediment layer.

From the above experiment, it can be seen that applying the detection method to GPR data is very efficient. Diffraction events from different structures, such as localised objects and faults at the bottom of the lake were successfully detected. Moreover, diffractions originating from sharp bends that are masked by the reflection from the lacustrine sediments interface are easily observed on the D-section image.

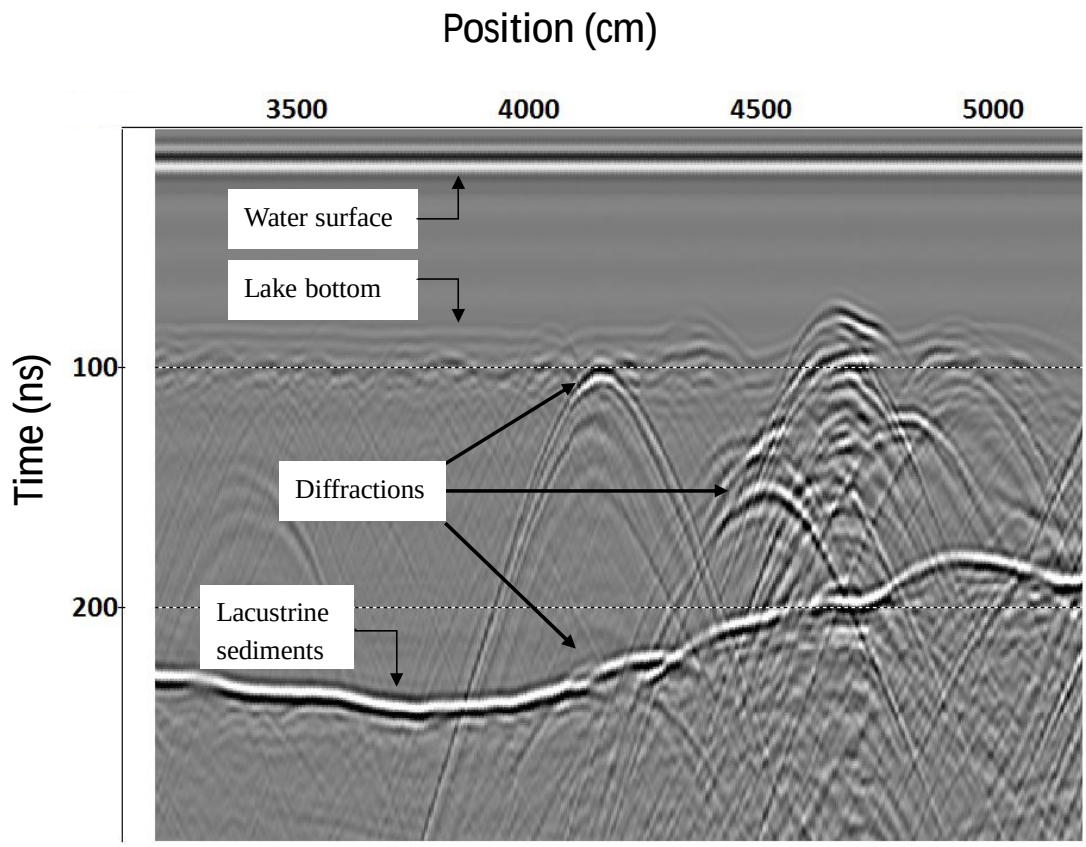

Figure 5-13: An interpreted part of the GPR lake data that is used with diffraction imaging techniques.

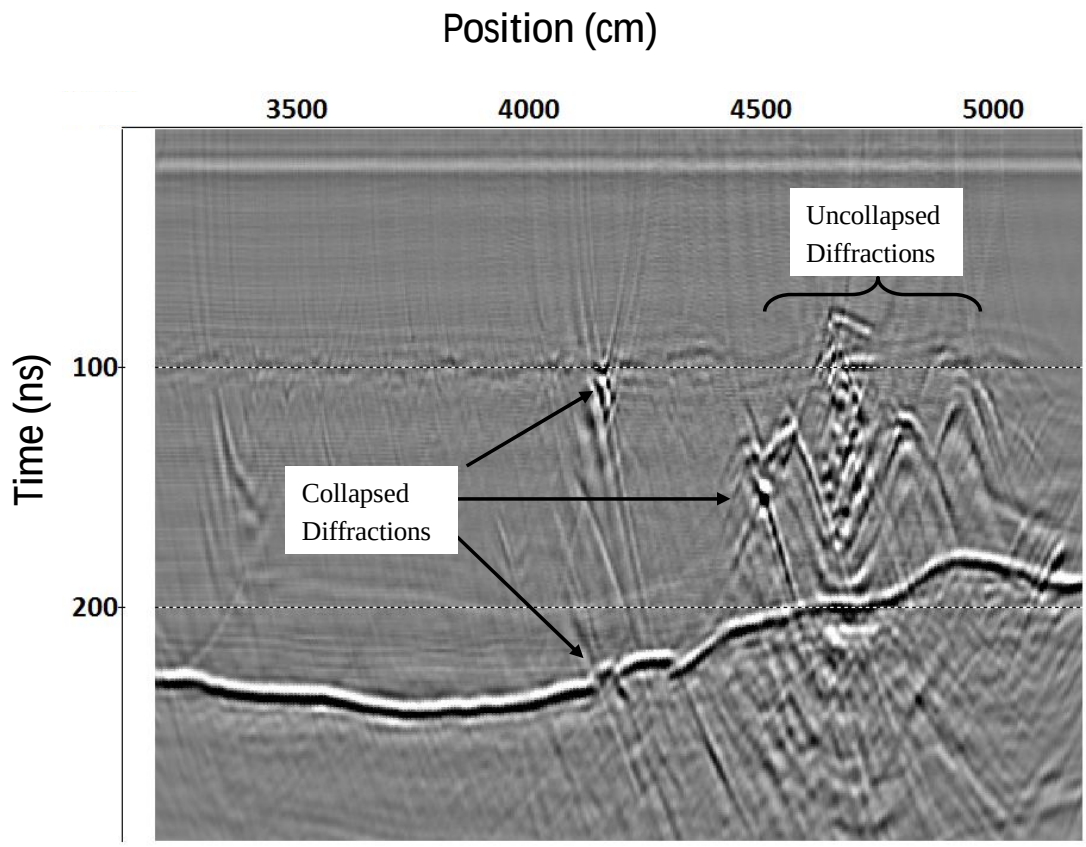

Figure 5-14: The same section as in Figure 5-13 after migration. The diffraction events indicated by the arrows are collapsed while the other diffractions that affected by the variation of the traces interval are not collapsed.

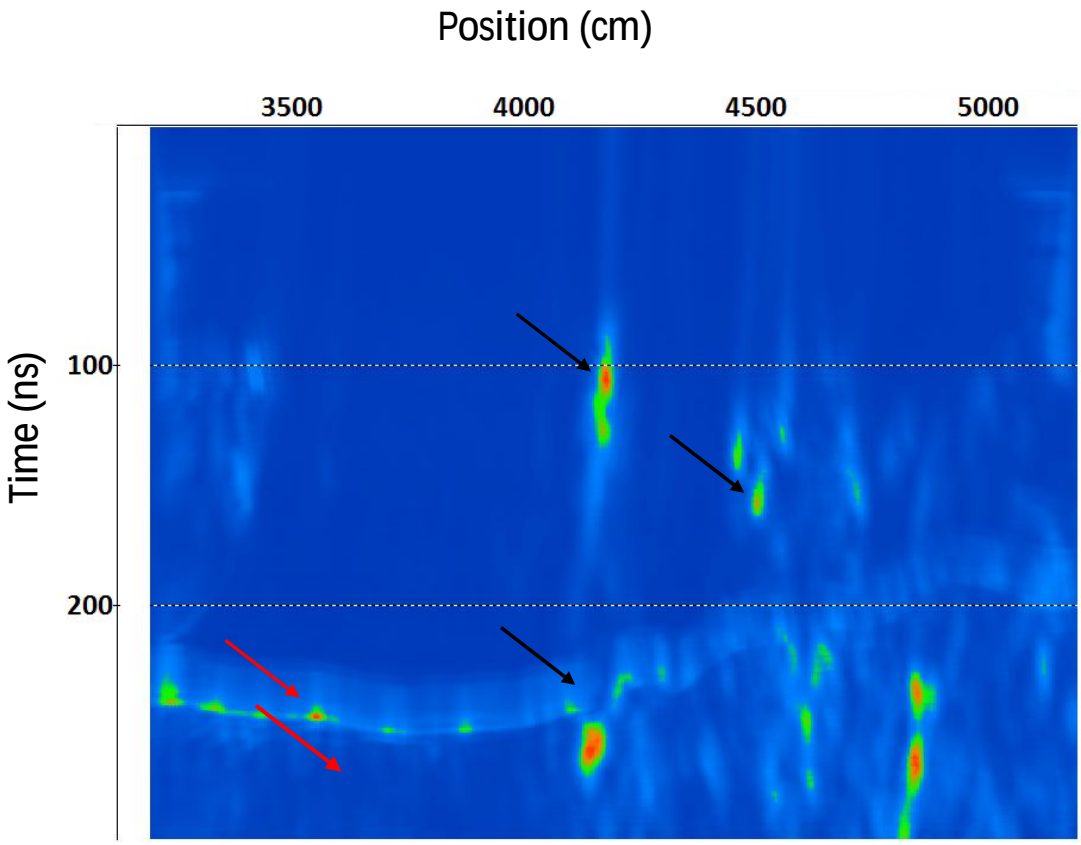

Figure 5-15: The D-section of the input section in Figure 5-13 with phase-reversal consideration showing high semblance values at the location of the diffraction events. The red arrow indicates a diffraction produced from a sharp bend in the lacustrine sediment that was hidden by the reflection interface.

5.5 CO2CRC Otway synthetic time-lapse model

In this section, a more detailed seismic forward model is presented based on the geological model of the CO_2 sequestration site of the CO2CRC Otway Project. The objective of this model is to illustrate the application of diffracted wave imaging in time-lapse data to detect small amounts of CO_2, which could escape from its primary containment. The properties of the synthetic time-lapse seismic data, such as offset range, bandwidth, repeatability and signal-to-noise (S/N) ratio, are based on the field data acquired at the Otway site (Pevzner et al., 2011). In this example, the diffraction detection method is targeting the weak signals related to small secondary accumulations of CO_2 in the saline formation above the main reservoir. Two assumptions are considered in this approach: (1) there is no significant change in velocity due to introduction of the CO_2 plume and (2) baseline and monitor surveys are cross-equalised; all repeatable events (reflections) are suppressed by subtraction (monitor minus baseline). In this case the difference section will only contain non-repeatable noise and signals related to the presence of new scatterers.

5.5.1 Rock-physics modelling

It is expected that injecting CO_2 into a formation will change its response to seismic waves, which will accordingly change their amplitudes and traveltimes. The degree of this change is strongly dependent on the properties of the reservoir rock and injected fluid. Therefore, a rock-physics model based on the reservoir condition is needed to see whether such change is observable as a function of time. The reservoir properties were obtained from well logs and core data from the injection well. Table 5.1 shows the values used for the fluid substitution modelling. The injected CO_2 gas mixture is 80% CO_2, 20% CH_4.

Table 5.1: Reservoir properties used for the fluid substitution model.

Reservoir properties	**Temperature in °C**	**Pressure in MPa**	**Salinity in ppm**	**Porosity in %**
	57	15	750	26
Gas composition	CO_2 mole fraction		CH_4 mole fraction	
	0.8		0.2	
Elastic properties	**Bulk modulus (*K*) in GPa**		**Density (ρ) in g/cm^3**	
Brine	2.466 (gas free)		0.992 (Batzle and Wang)	
CO_2/CH_4	0.0326		0.383	
Grain material	35		2.65	
Interval velocity obtained from VSP	$V_{P,pre}$		$V_{S,pre}$	
	3375 m/s		1801 m/s	

A fluid substitution workflow was employed in order to model the seismic properties (velocities and densities) in a given reservoir condition (pressure, temperature, salinity, porosity) (Batzle and Wang, 1992). Gassmann's equation represents the elastic properties prior to and after CO_2 injection by predicting the change in bulk modulus due to fluid substitution (Gassmann, 1951; Smith, et al., 2003). In this workflow, the elastic properties of a rock saturated with a mixture of brine and the injected gas (a mixture of CO_2 and CH_4) are calculated from the elastic properties of a rock saturated with formation brine, the properties of the fluid mixture, the solid grain material and porosity f. The bulk modulus of the rock before the injection (K_{pre}) is calculated from the VSP interval velocities ($V_{P,\text{pre}}$, $V_{S,\text{pre}}$),

$$K_{pre} = v_{P(pre)}^2 \rho_{pre} - \frac{4}{3}\mu \,, \tag{5-1}$$

where μ is the shear modulus is given by

$$\mu = v_{S(pre)}^2 \rho_{pre}$$

and the density of the reservoir before injection (ρ_{pre}) is given by

$$\rho_{\text{pre}} = \phi\, \rho_{\text{brine}} + (1 - \phi)\, \rho_{\text{grain}}. \tag{5-2}$$

The bulk modulus of the rock after injection of the gas mixture (K_{post}) is then computed using Gassmann's equation:

$$\frac{K_{pre}}{(K_{grain}-K_{pre})}-\frac{K_{brine}}{\emptyset(K_{grain}-K_{brine})}=\frac{K_{post}}{(K_{grain}-K_{post})}-\frac{K_{brine,CO_2,CH_4}}{\emptyset(K_{grain}-K_{brine,CO_2,CH_4})} \quad (5\text{-}3)$$

In-situ brine properties, (ρ_{brine}) in equation (5 2), and (Kbrine) in equation (5 3) are calculated using the empirical formula of Batzle and Wang (1992). The CO_2/CH_4 mixture properties ($K_{\text{CO}_2,\text{CH}_4}$, $r_{\text{CO}_2,\text{CH}_4}$) are computed by an equation of state based on the GERG 2004 model (Kunz et al., 2004). Wood's mixing rule (Mavko et al., 1998) is then applied to estimate the fluid bulk CO_2 modulus of the CO_2/CH_4/brine mixture ($K_{\text{brine},\text{CO}_2,\text{CH}_4}$),

$$\frac{1}{K_{brine,CO_2,CH_4}}=\frac{S_{brine}}{K_{brine}}+\frac{S_{CO_2,CH_4}}{K_{CO_2,Ch_4}}, \quad (5\text{-}4)$$

where S_{brine} and $S_{\text{CO}_2,\text{CH}_4}$ $\text{S}_{\text{CO}_2,\text{CH}_4}$denote the brine saturation and gas saturation, respectively.

The use of Wood's equation assumes uniform saturation—a reasonable assumption for sandstones at seismic frequencies. The values of the bulk modulus (K_{grain}) and density (ρ_{grain}) of the grain material are close to those of the Paaratte injection zone. The values after injection $V_{P,\text{post}}$ = 3164 m/s, $V_{S,\text{post}}$ = 1821 m/s, and density ρ_{post} = 2172 kg/m^3 were estimated using the following equations:

$$r_{\text{post}} = f\left(S_{\text{brine}}\, r_{\text{brine}} + S_{\text{CO}_2,\text{CH}_4}\, r_{\text{CO}_2,\text{CH}_4}\right) + (1-f)\, r_{\text{grain}}, \quad (5\text{-}5)$$

$$v_{p(post)} = \sqrt{\frac{K_{post}+\frac{4}{3}\mu}{\rho_{post}}},\ v_{s(post)} = \sqrt{\frac{\mu}{\rho_{post}}}.$$

One of the scenarios investigated was to inject 10,000 tonnes of CO_2 at a depth of 1490 m into the Paaratte formation. Based on flow simulations, we assume that a small plume (170 m wide and 13 m thick) with CO_2 saturation of 30% is formed (Figure 5-16).

At the injection depth, the radius of the first Fresnel zone—from which most of the energy is reflected—is more than 215 m. This means that a secondary accumulation of CO_2 will fall within the first Fresnel zone and will produce a velocity perturbation

causing seismic diffractions. Therefore, to image a small amount of CO_2 we need to look at the diffracted energy.

5.5.2 2D finite-difference modelling

2D finite-element forward modelling package Tesseral 2D was used to compute the seismic response of a small CO_2 plume placed into the Paaratte formation at a depth of 1500 m. Two 2D depth models (with and without the CO_2 plume) were created consisting of thirteen layers up to a depth of 2500 m mapped from a seismic line extracted from a pre-production, large scale 3D survey recorded at the area of interest. The synthetic seismic datasets were obtained using 301 receivers with a 10 m spacing interval along the model and 200 sources placed at the receiver positions 51 to 250 as shown in Figure 5-16. The synthetic data sets were generated using a 50 Hz Ricker wavelet and a 2 ms sampling interval. The velocities used were based on the interval velocities measured from zero-offset VSP data recorded in a nearby monitor well (Naylor-1). Both synthetic datasets were produced by acoustic finite-difference modelling so only P-waves are modelled.

Figure 5-17 shows one synthetic shot gather before and after placing the CO_2 plume into the model and the difference between them. Both datasets were NMO corrected and stacked. From Figure 5-18, we can observe that stacking with a macrovelocity model produces reflection image with horizons, whereas diffractions remain un-collapsed.

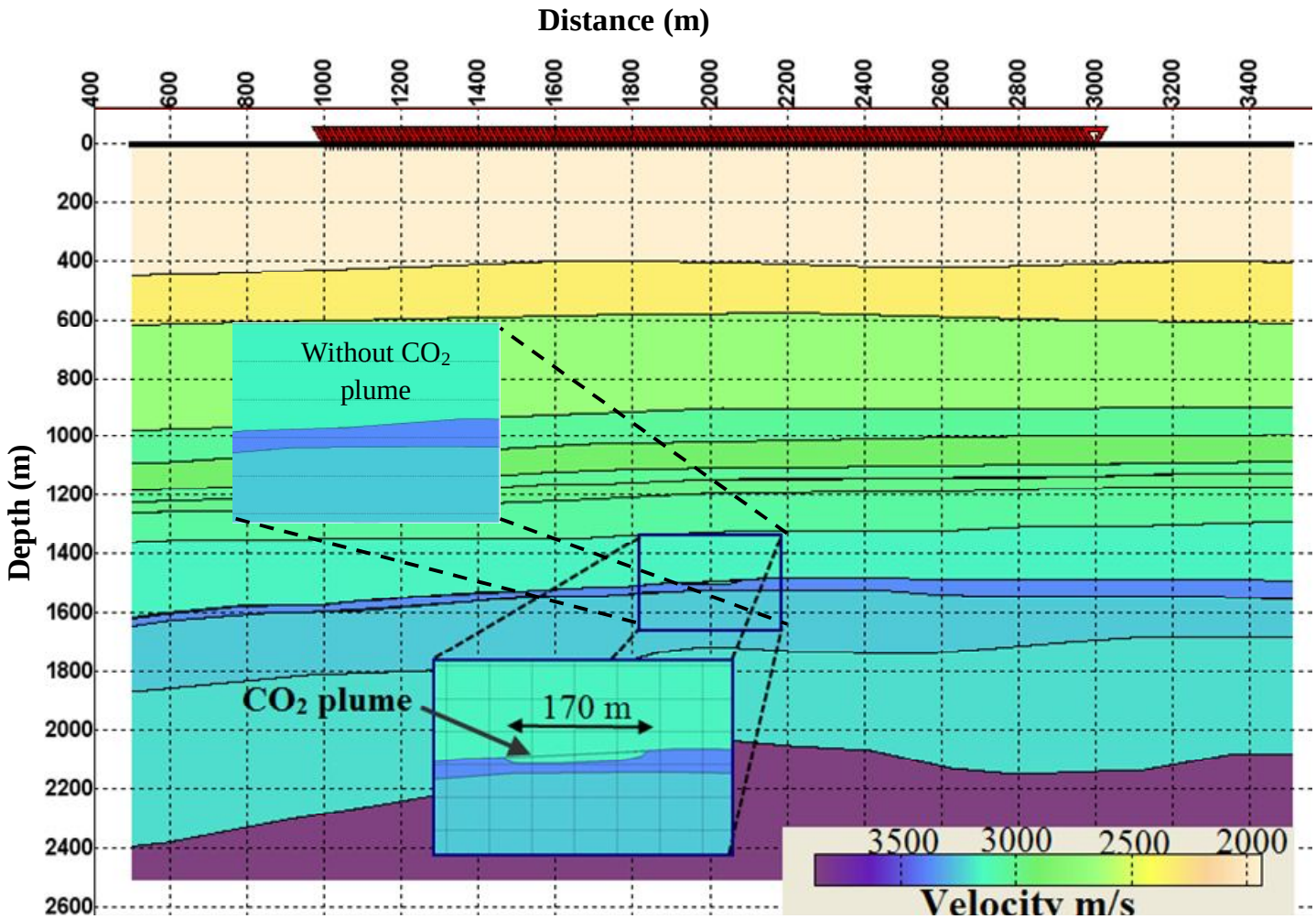

Figure 5-16: The velocity depth model used for the finite-difference modelling; the zoomed area shows the CO_2 plume added to the time-lapse model.

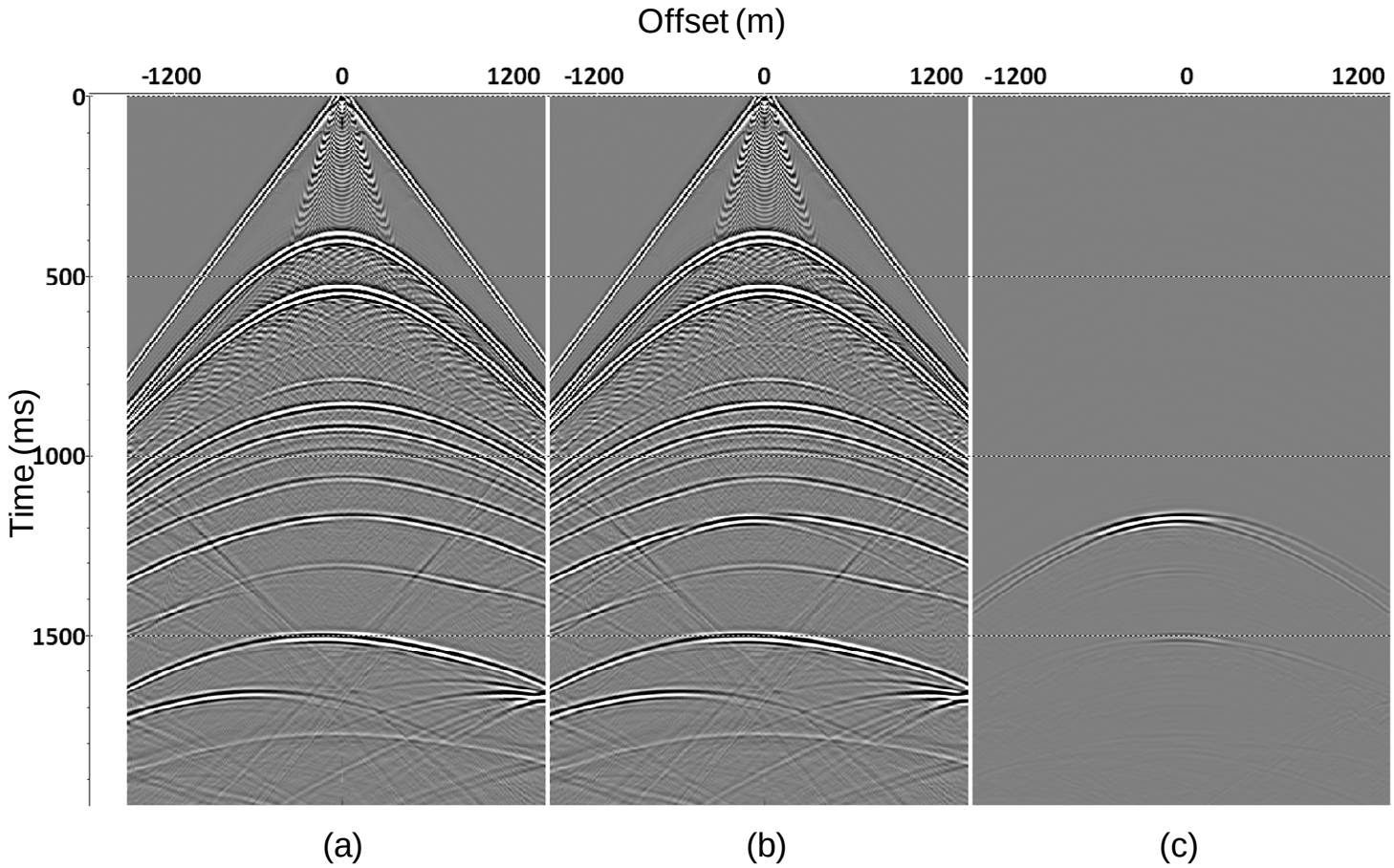

Figure 5-17: (a) The finite-difference acoustic wavefield of one shot gather from the baseline survey, (b) monitor survey with CO2 plume and (c) the difference between the two surveys.

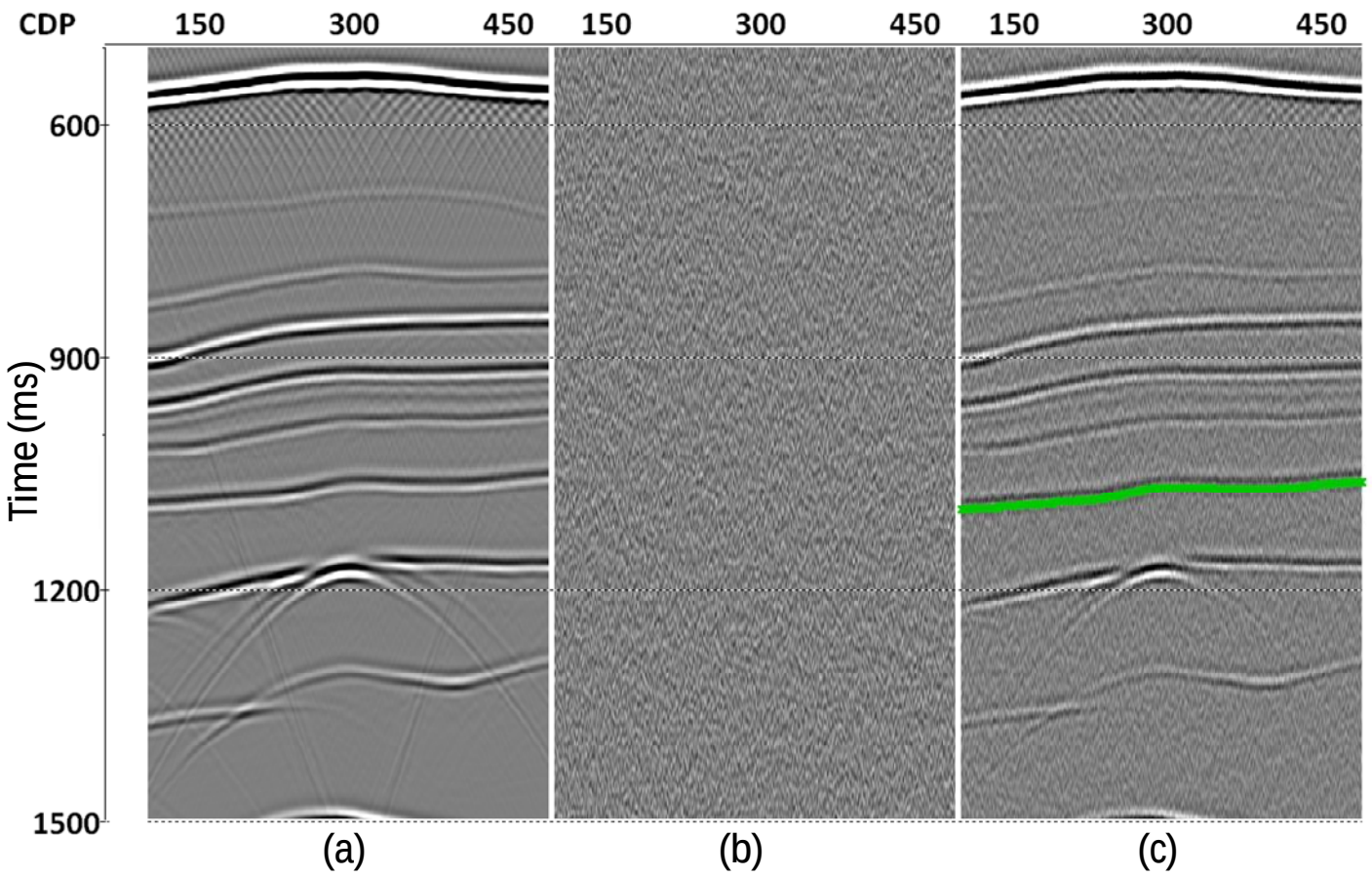

Figure 5-18: (a) A stacked section of the noise-free synthetic data, (b) random noise corresponding to the S/N ratio and bandwidth of real data and (c) signal plus noise. The green line indicates the horizon picked to calculate the desired S/N ratio.

5.5.3 Data conditioning

The feasibility of monitoring the injected CO_2 using time-lapse seismic signals depends on two main factors: (1) the seismic response to CO_2 and (2) the level of repeatability (e.g., level of the time-lapse noise) of the time-lapse seismic data (Lumley, 2010). The seismic response can be modelled using fluid substitution, replacing the saline water with CO_2, which changes the reflectivity of the host rock formation and hence the seismic response. However, the time-lapse noise level cannot be modelled as easily. While the geometry problems caused by the mismatching source-receiver positions between the surveys can be solved relatively easily with modern acquisition positioning systems, changes of near-surface conditions that can affect the time-lapse signal are unavoidable and require field studies. To this end, repeatability of time-lapse land seismic in the Otway project area has been studied extensively. Al-Jabri and Urosevic (2010) discussed the near-surface effect to understand the factors influencing the repeatability of 4D land seismic data. Pevzner et al. (2011) showed that one of the main factors affecting the measured non-repeatability (NRMS) of the time-lapse data is the ratio of the signal to coherent and background noise and found that there is a direct relationship between the S/N ratio and NRMS, so that the areas with a greater S/N ratio correspond to higher repeatability. For the field data acquired in the Otway project, a good repeatability with a value of NRMS 30 – 40% at the injection depth requires the S/N ratio to be between 5 and 10. Based on the field data quality at the site, we applied the following steps to simulate real conditions:

1. Generating artificial non-repeatable random noise for the baseline and for the repeated data sets. The generated noise has the same characteristics as the noise measured on the field data sets: the same frequency range, sample rate and so on, as shown in Figure 5-18b.
2. Picking a horizon in the Paaratte formation just above the injection zone to measure the S/N ratio around this horizon.
3. Mixing the random noise with the signal at the measured S/N ratio, producing synthetic data of quality comparable to the field seismic data as shown in Figure 5-18c.

The amount of noise added corresponds to S/N ratio of about 5, which is the lowest data quality scenario. This is done in order to include the non-modelled noise factors (e.g., source generated noise, near-surface noise, geophone coupling, etc.) that affect the data quality. The S/N ratio was measured along the Paaratte horizon within a 30 ms time window as shown in Figure 5-18c.

5.5.4 Computation of D-sections

Datasets, baseline and monitor (with a CO_2 plume) have been processed simultaneously to produce two stacked sections, both with the same amount of noise. The diffraction energy on the monitor section was significantly affected by the noise as shown in Figure 5-18c; this indicates that diffractions are more sensitive to noise than reflections. Using time-lapse analysis, the baseline stack is subtracted from the monitor stack. This process will supress reflections and any other repeated signal, leaving only the diffraction events produced from the CO_2 plume as shown in Figure 5-19a. The difference section is then used as an input for D-section computation. This can be seen in the resulting D-section in Figure 5-19b, where the time-lapse signal corresponding to 4,000 tonnes of CO_2 is clearly identified on the D-section as an anomaly.

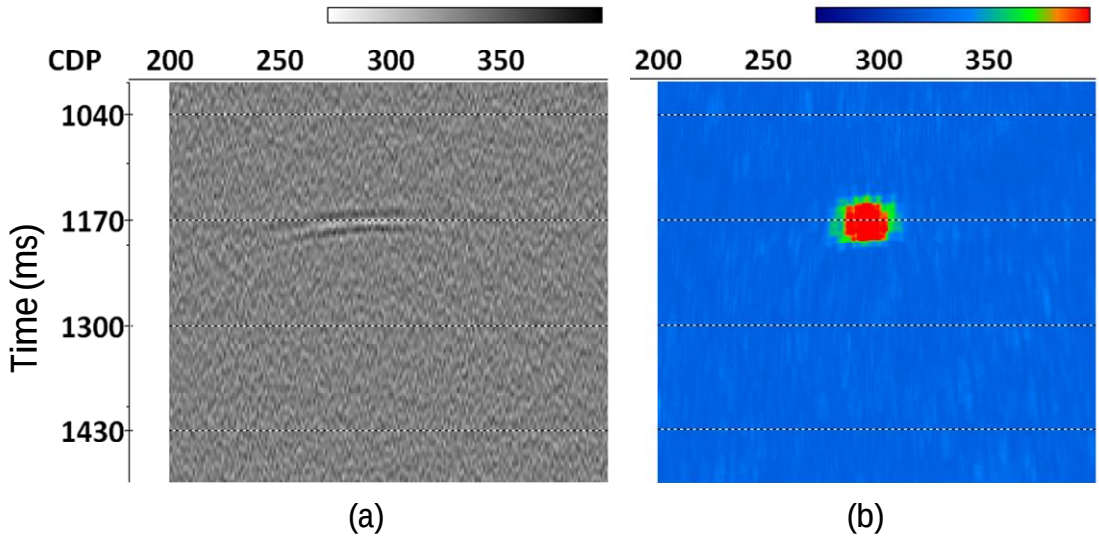

Figure 5-19: (a) The time-lapse stacked section of 4,000 tonnes of CO_2 plume, and (b) the corresponding D-section. The diffraction is correctly depicted at the position of the plume.

The diffraction imaging method discussed above is applied to post-stack data. This means that the datasets are NMO corrected and stacked over the common midpoints (CMP). This process enhances the reflections and attenuates the diffractions (Khaidukov, et al., 2004). Therefore, dip moveout (DMO) correction is applied to the data in order to enhance the diffraction energy over the noise and to improve the detection method. Figure 5-20 shows two zoomed-in D-sections, (a) one before DMO and (b) another with DMO applied for 3,000 t of CO_2. It can be seen that the D-section image produced when applying DMO to the data enhances the results and significantly improves the S/N ratio.

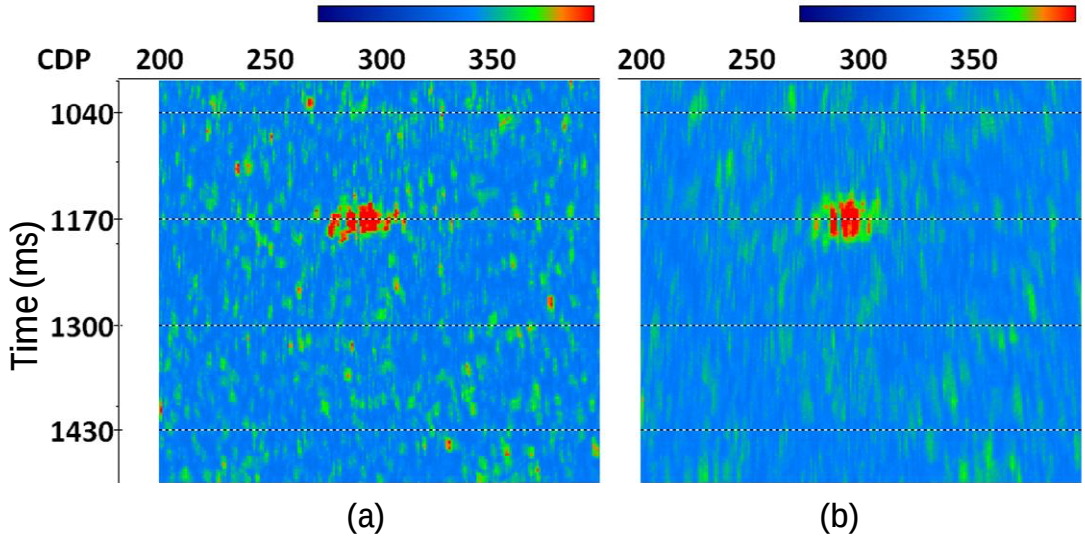

Figure 5-20: A comparison between two D-sections of the same data, (a) before, and (b) after applying DMO.

In order to better understand the CO_2 plume effect on the seismic data, we produced a noise-free time-lapse section that included only diffracted waves (Figure 5-21). It can be seen that there are two diffraction hyperbolae produced from the edges of the plume. Unlike point scatterer diffraction, edge diffraction has a phase reversal on the inner side of the hyperbola, that is, the part below the plume. The blue and red hyperbolae in (Figure 5-21) show a phase reversal between the outward and inward parts of diffracted waves at both edges of the plume. For a small plume, the apices of the diffraction hyperbolae are too close to each other; this makes the phase change difficult to observe, especially in the case of poor data quality.

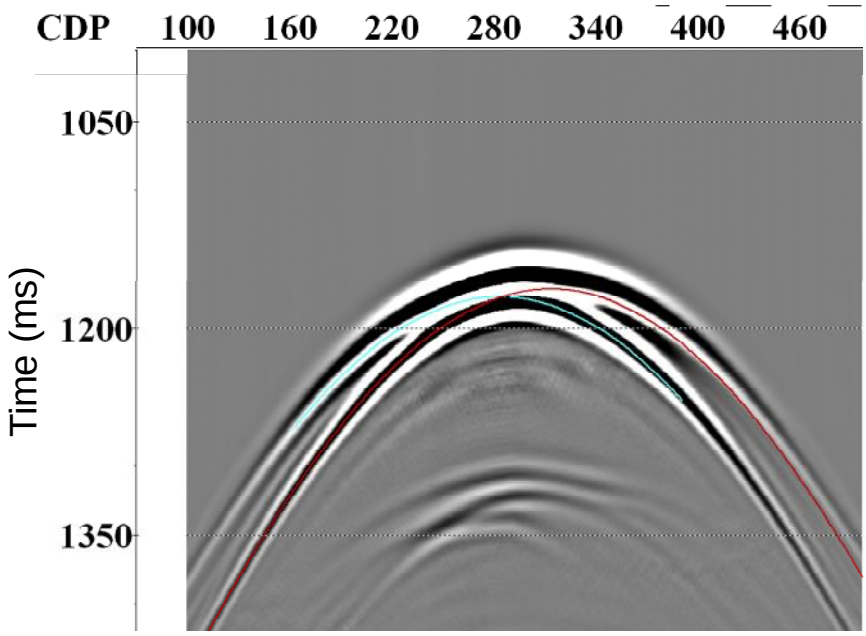

Figure 5-21: Noise free data zoomed on the CO_2 plume. The blue and red diffraction hyperbolae show the phase reversal across the edge of the CO_2 plume.

Applying equation (4.1) to both sides of the diffraction curve will reduce the coherency of the signals due to a 180 degree phase change on either side. Therefore, we can produce two different D-sections for each side of the diffraction hyperbolae and add them. This process enhances the energy on each side of the plume by avoiding amplitude cancellation during the correlation process. Figure 5-22 shows (a) a comparison between a D-section computed along both sides of the diffraction hyperbola and (b) D-sections computed separately for each side of the hyperbola and then added together; the latter result has a higher S/N ratio.

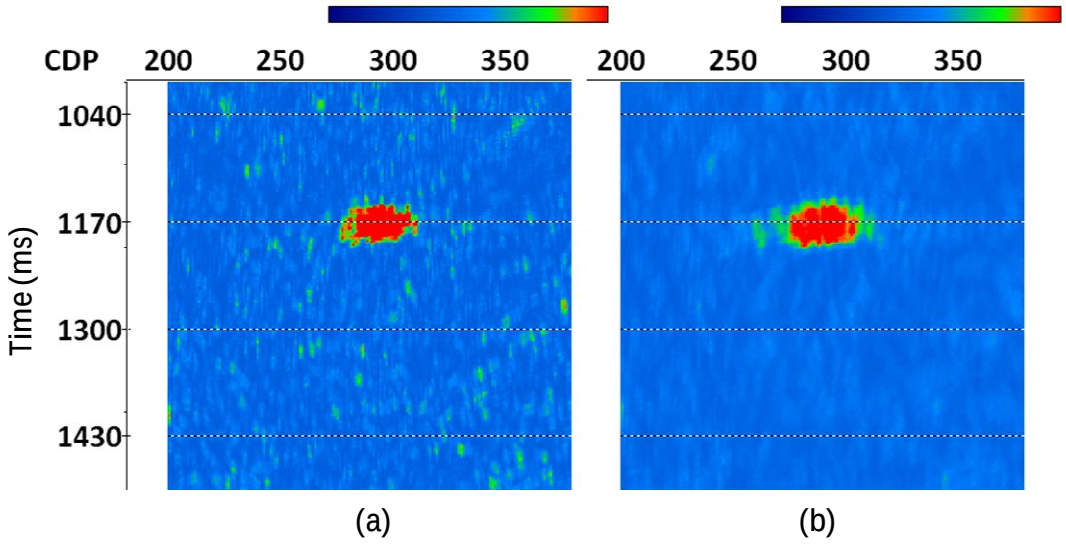

Figure 5-22: Two different D-sections, (a) calculated along the full diffraction hyperbola and (b) with the phase reversal. The latter significantly enhances the D-section image.

5.5.5 Comparison of reflection verses diffraction images

To analyse the ability of diffraction imaging to detect small amounts of CO_2 we produced a number of time-lapse stacked sections corresponding to different amounts of CO_2. For each stacked section, a D-section was computed and compared with the reflection section produced by post-stack time migration. Figure 5-23 shows a comparison between migrated sections and D-sections for different CO_2 volumes. It can be seen that the amount of CO_2 resolved on the data is about 1,000–2,000 tonnes. Data with less than 1,000 tonnes of CO_2 has very weak diffraction energy and will be difficult to detect. This threshold is similar for migrated data and D-sections.

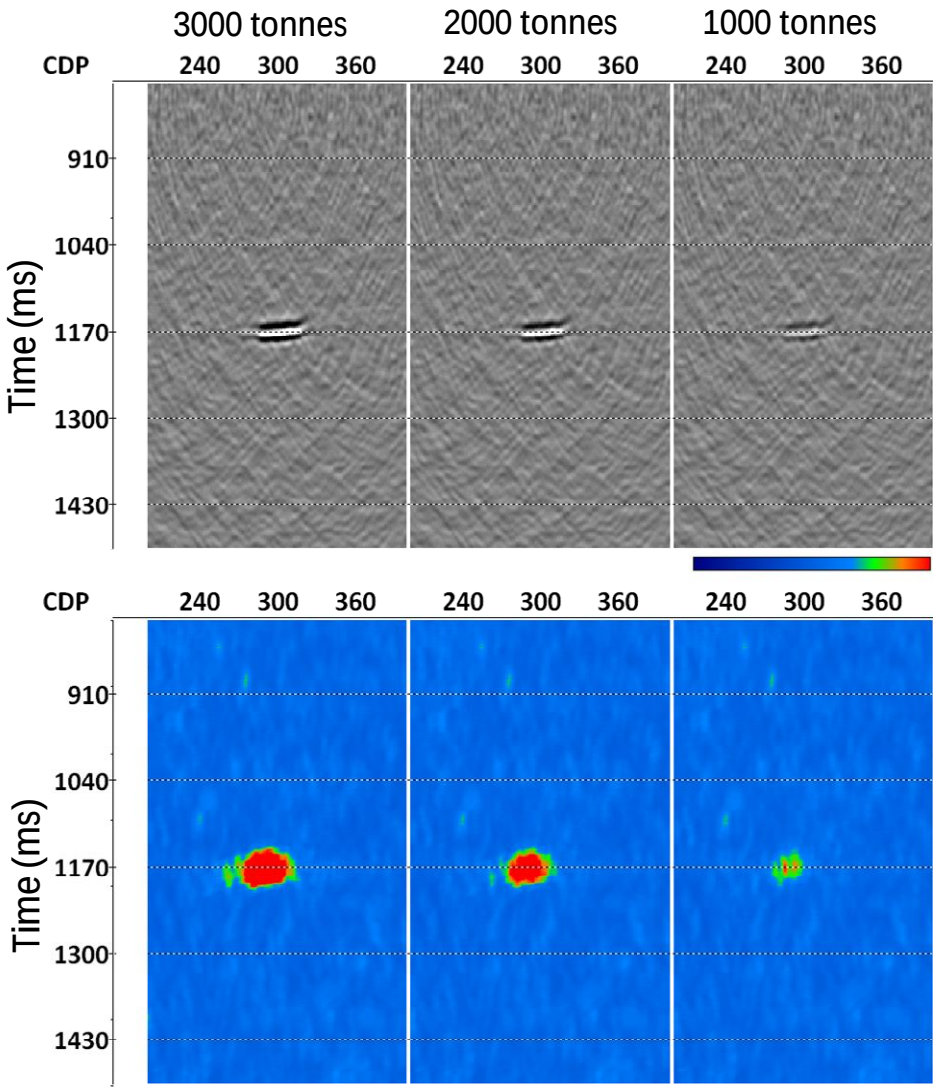

Figure 5-23: Comparison between (top) migrated sections and (bottom) D-sections for the time-lapse signal of different CO_2 volumes.

5.6 Conclusions

In this chapter the diffraction detection method was examined on different 2D datasets by using numerical and physical modelling of a simple edge diffractor. The phase-reversal that is exclusive to edge diffraction was observed on both models. GPR data was also used to illustrate the validity of the method. The results demonstrate the efficiency of the method in detecting diffraction events originated from different sources such as faults, small objects, sharp bends, and so on. The detection quality is enhanced when considering the phase-reversal correction where specular reflections are significantly suppressed.

The Otway numerical modelling experiment shows that in data with relatively low S/N ratios, seismic diffractions can be used to detect comparatively small amounts of CO_2. The method is based on defining the CO_2 location by measuring the coherency of the signal along the diffraction offset-traveltime curves on time-lapse difference sections. The robustness of the method results from the fact that the offset-traveltime curves are computed using NMO velocities already obtained from the conventional velocity analysis. The method was applied to a time-lapse synthetic stacked section representative of a CO_2 geosequestration site of the CO2CRC Otway Project. Using time-lapse analysis any repeated structures, including specular reflections, are suppressed. Given the amount of noise found in the field data, the predicted minimum detectable amount of CO_2 using the proposed approach was estimated to be 1,000 to 2,000 tonnes. This example demonstrates that the phase-reversal correction substantially avoids amplitude cancellation, maximises the semblance value and improves the detection method. The use of diffractions rather than reflections for monitoring small amounts of CO_2 can enhance the capability of subsurface monitoring of CO_2 accumulations.

6. Chapter 6 - 3D DIFFRACTION IMAGING EXAMPLES

6.1 Introduction

In this chapter, further tests for the detection of diffracted waves are presented, this time on 3D data using both numerical and real seismic data. The objectives of using synthetics are to examine the detectability limits of the method and to optimise the computational parameters for the subsequent analysis of field data. In the numerical models diffractors from a dipping plane were introduced and the sensitivity of the method to different amount of random noise was tested. In the real seismic data example 3D seismic data obtained from the Otway CCS project was used. 4D seismic data from Otway project has been utilised to produce different time-lapse D-volumes.

6.2 Numerical model of simple edge diffractor

A 3D synthetic example is used to examine the validity of the method for the detection of dipping edge diffractors, this time using a response from a segment of a dipping plane. The data were computed using the edge wave superposition method (Klem-Musatov and Aizenberg, 1989). The data contain reflections from a corner of a dipping plane and diffractions at the termination of the plane. Dip of the interface is 9°. P-wave velocity in the model is constant and equal to 2500 m/s; the central frequency of the wavelet is 30 Hz. Zero-offset synthetic datasets are obtained using 100 in-lines and 123 cross-lines with 50 m trace spacing as shown in Figure 6-1. 7% of random white noise was added to the synthetic data.

The D-volume was computed with phase-reversal consideration and compared with time migrated data as shown in Figure 6-2. Utilising the phase-reversal phenomena the output D-volume in Figure 6-2 (b) shows location of the edge of the quarter-plane, while the specular reflection from the plane itself is largely suppressed. As discussed in chapter 4, the phase-reversal of the diffraction traveltime curve from a dipping reflector does not occur at its apex. In this example however the result is not affected because the dipping angle is very small.

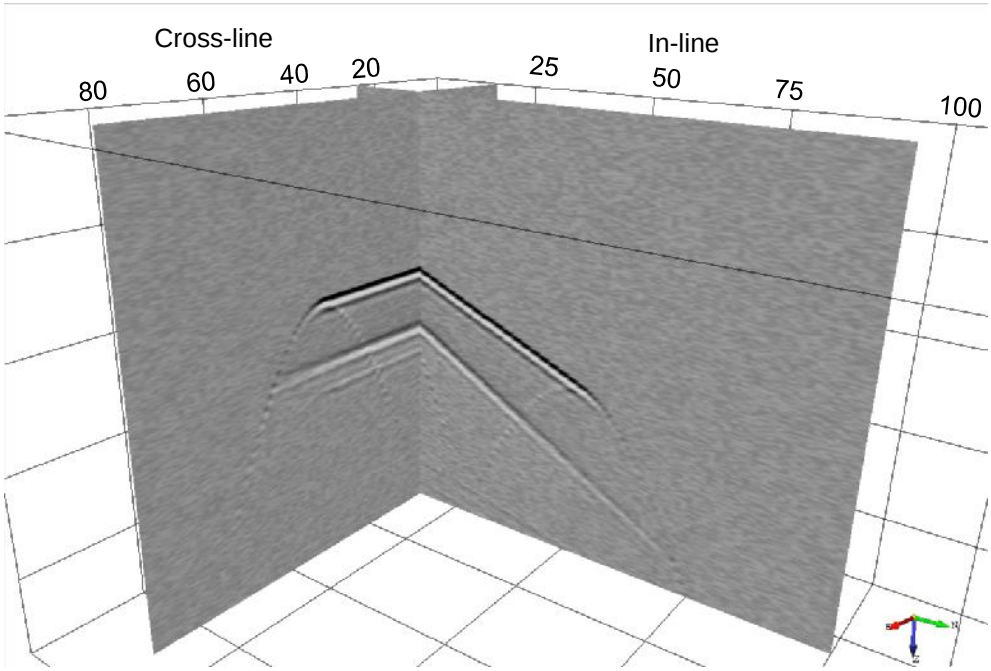

Figure 6-1: The zero-offset synthetic 3D dataset of a dipping plane with edge diffraction at the termination of the plane.

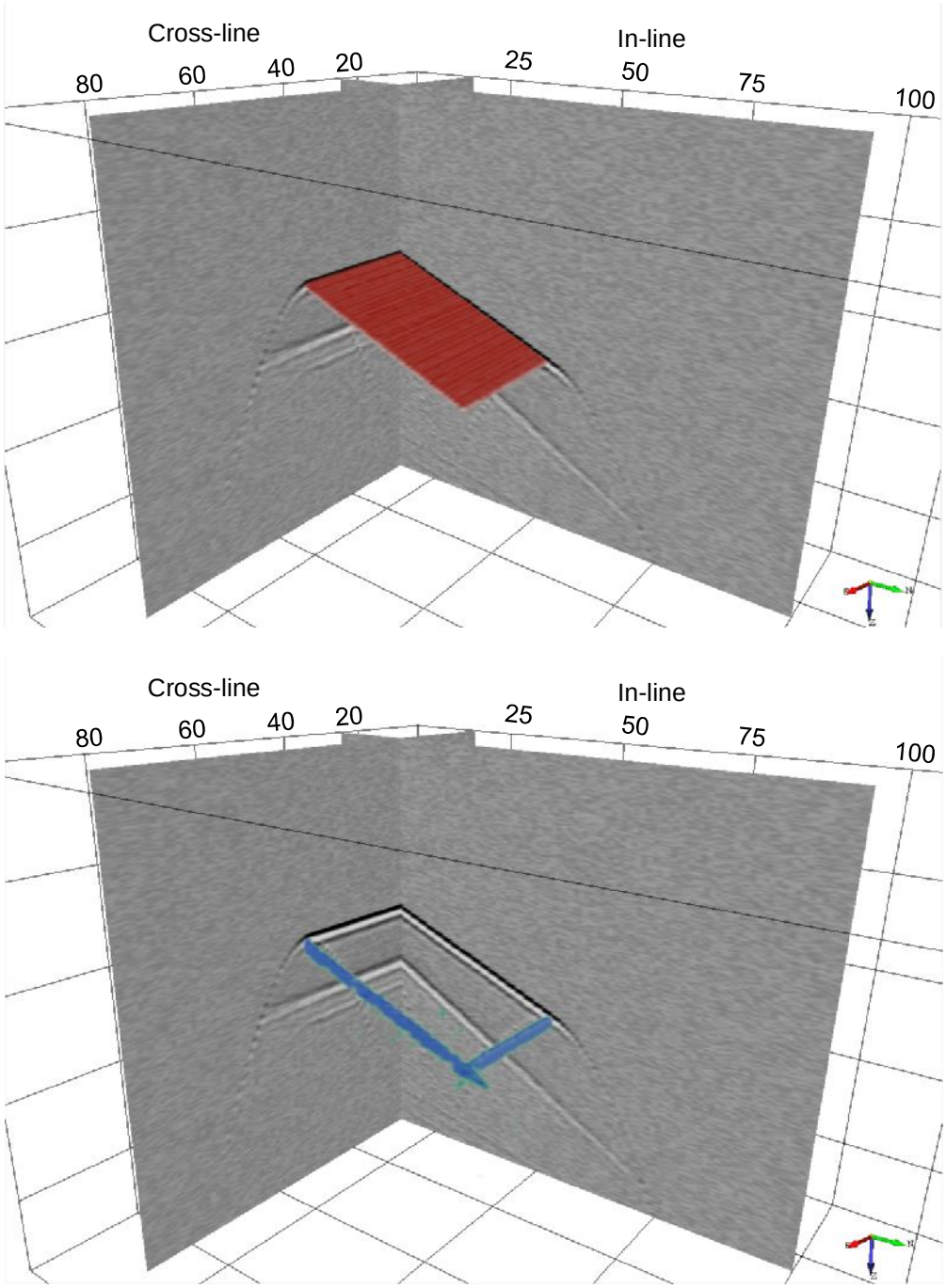

Figure 6-2: (top) 3D migrated data (in red) showing the dipping plane. (bottom) A D-volume image showing the diffraction events collapse at the termination of the plane (in blue).

6.3 Grid test

In this example the 3D synthetic dataset was obtained using the same geometry and velocity model of the 3D Otway field data example discussed in the next section. The dataset consists of 159 in-lines and 195 cross-lines, bin size is 10x10 m and the in-line axis of the binning grid is oriented at 25° from north. A grid of line diffractors is placed at every 200 m and repeated every 200 ms over the 2 s record length (Figure 6-3). Since the size of the 3D survey is small (1.6x1.95 km), a single velocity function without lateral variations is used for the D-volume computation; the same approach was used to migrate the field data. The synthetic data is generated by convolving spikes placed along the traveltime curves with zero-phase wavelet and then applying a band-pass filter (10-14-40-80 Hz) to match it with the field data frequency band. The method is tested on the synthetic data with different amounts of added random band-limited noise as shown in Figure 6-4.

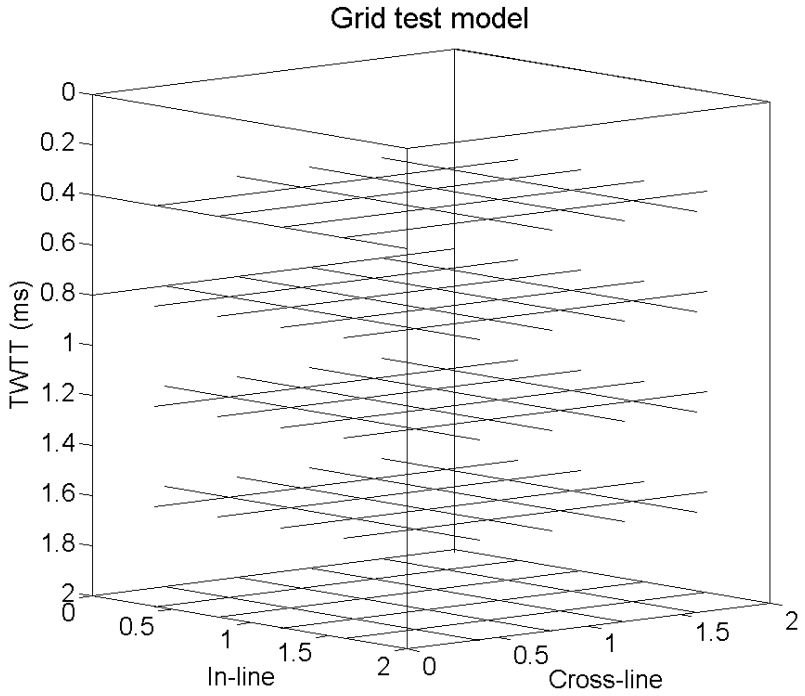

Figure 6-3: A schematic showing the in-line and cross-line diffractors produced at every 200 ms.

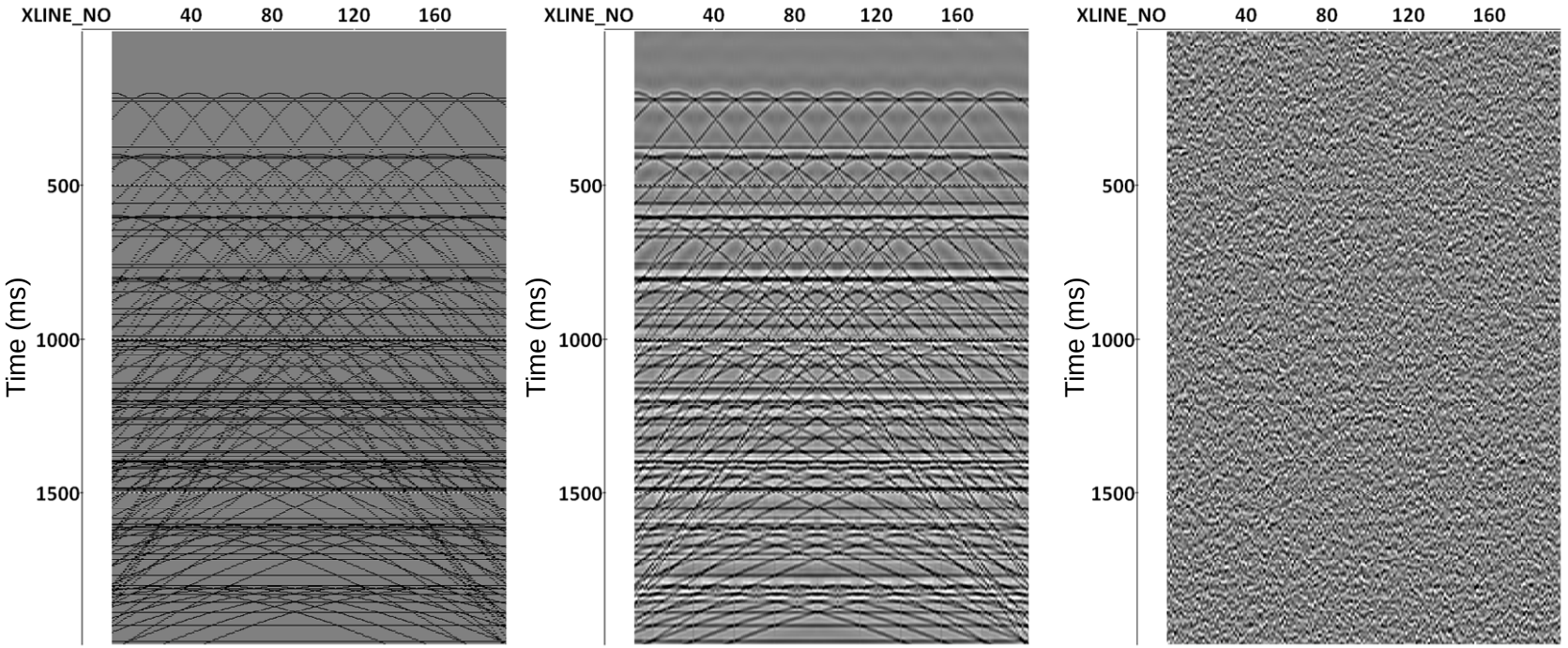

Figure 6-4: (a) Synthetic spikes created along the diffraction traveltime curve distributed every 20 in-lines and cross-lines and repeated every 2 ms using the velocity field from Otway data. (b) The noise-free section after convolving it with the same frequency bandwidth. (c) The same section after adding random noise six times the signal (S/N ratio of 0.16) where the diffractions are masked by the noise.

In order to test the sensitivity of the method to noise we introduce a range of noise levels to the model and produce synthetics with different S/N ratios starting from noise-free case and finishing with S/N ratio of 0.1 (i.e., 1000% of random band-limited noise). For every noise level we compute D-volumes over three different offset limits (h=50 m, 100 m, and 200 m) and compare the results. A time window of 30 ms (roughly the apparent period of the actual seismic data) is used to compute semblance in both synthetic and field data examples.

Figure 6-5 shows 600 ms time slices of a D-volume with a S/N ratio of 0.16 over three different offset limits: h=50 m, 100 m, and 200 m. The time slice of the D-volume computed over a 100 m offset limit has the best resolution; the diffractor lines are the sharpest. However, the same D-volumes sliced at 1200 ms (Figure 6-6) shows the best results for the offset limit parameter of 200 m; with this offset limit the diffractor lines are less distorted than with the other values. Figure 6-7 shows different time slices of the data computed with the offset limit of 200 m and with S/N ratio of 0.16. As the time increases, the diffractor lines become wider and exhibit more distortion. To explore the sensitivity of the method to the band-limited random noise, we show the D-volumes time slices in Figure 6-8 for different amount of noise at the level of 1600 ms. Even with the high noise levels the diffractions are still clearly detectable with only some noise artefacts. The level of 1600 ms corresponds to the reservoir level where we expect to observe time-lapse effects in the field data.

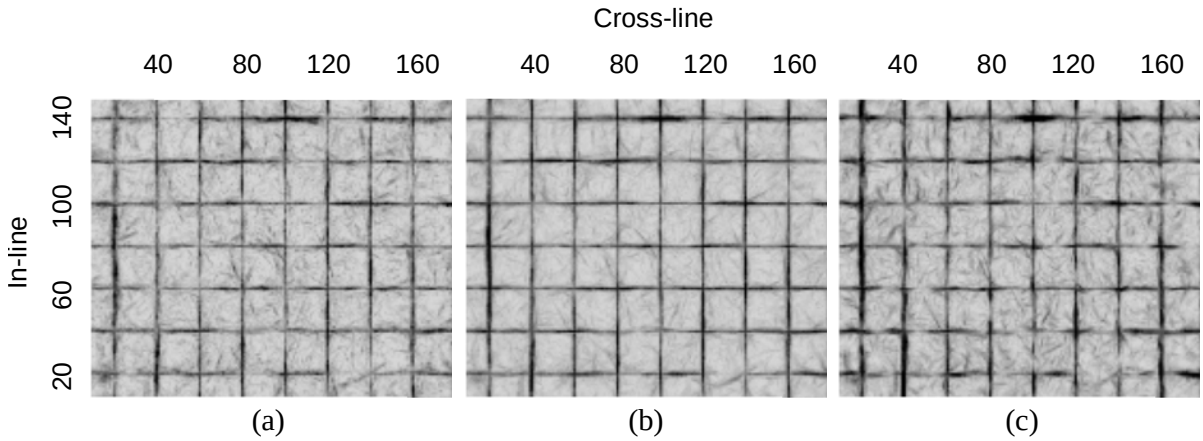

Figure 6-5: 600 ms time slices of three D-volumes computed over different offset limits, (a) 50 m, (b) 100 m, and (c) 200 m. The D-volume computed with 100 m limit has the sharpest image of the edge diffraction.

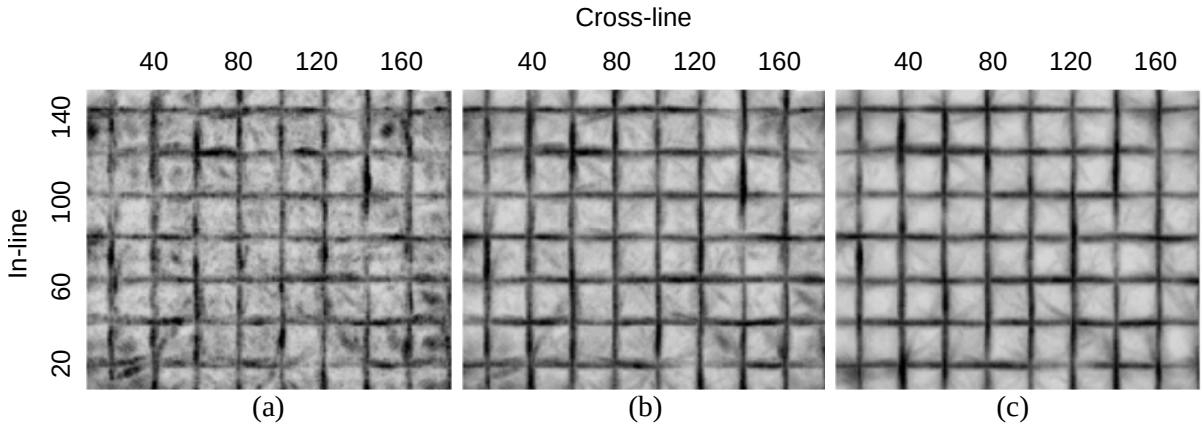

Figure 6-6: 1200 ms time slices of three D-volumes with S/N ratio of 0.16 computed over different offset limits, (a) 50 m, (b) 100 m, and (c) 200 m. The D-volume computed with 200 m limit has the sharpest image of the edge diffraction.

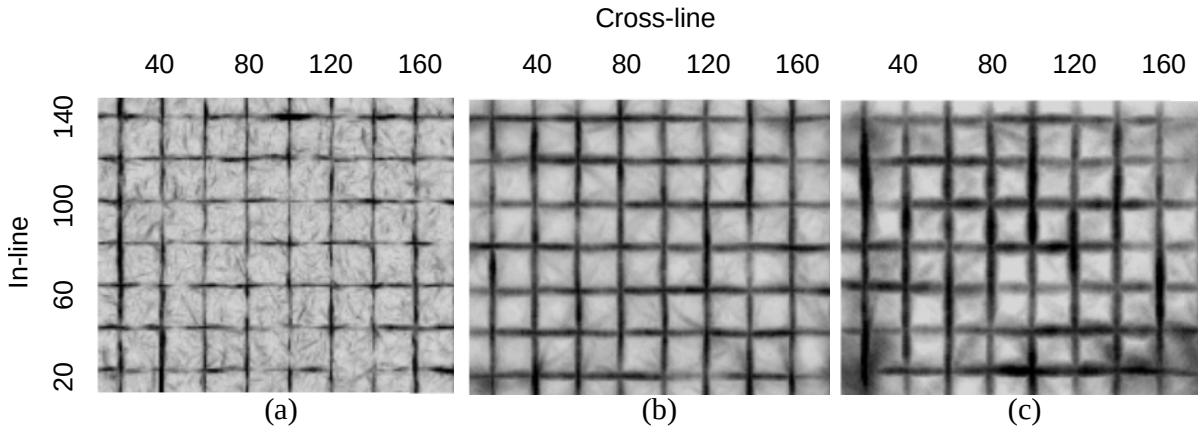

Figure 6-7: Three time slices of the same D-volume computed with 200 m offset limit, (a) at 600 ms, (b) at 1200 ms, and (c) at 1600 ms.

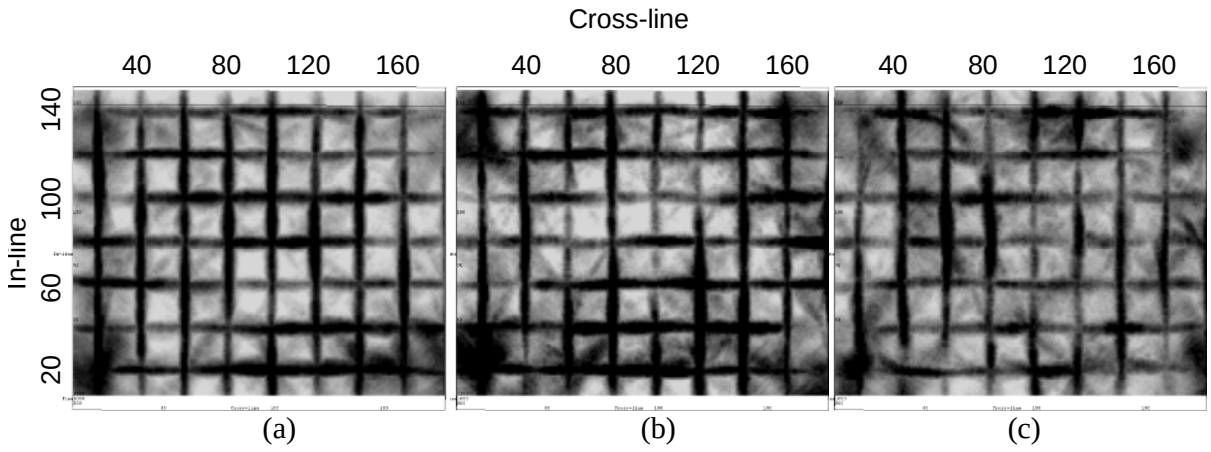

Figure 6-8: 1600 ms time slices of a D-volume for different S/N ratio data sets: (a) 0.16, (b) 0.125, and (c) 0.1. Even with the high noise levels the diffractions are still clearly detectable with only some noise artefacts.

6.4 3D Otway example

The real data example used for the diffraction detection method was obtained as part of the monitoring program of the Otway project. The method was tested using both a single vintage 3D dataset as well as the difference volumes (2008-2009 and 2008-2010) of the 4D time-lapse seismic data. In both cases we consider only edge diffractors, that is, we assume a change of polarity across the edge. In the case of the single vintage 3D data, the maximum energy from diffracted waves, which we refer to as diffractivity,

should correspond to the fault planes and as such, we could compare it to standard seismic attributes used to detect faults. The S/N ratio is quite high for these datasets so we should get comparable results. In the case of the difference volumes, the maximum diffractivity should correspond to edges of the area within the reservoir induced by CO_2 injection. However, since previous studies show that the anticipated 4D signal level is low (Caspari, et al., 2012), we should not expect very conclusive results from the edge imaging.

First, we apply the method to a single vintage of Otway 3D data (2010). The D-volume is computed on a stacked 2010 volume. We also compute a so-called minimum similarity attribute (Tingdahl and De Rooij, 2005), a multi-trace attribute often used for fault detection. This attribute is computed on the post-stacked time-migrated volume. Figure 6-9 shows 1000 ms time slices of both attributes. The D-volume (Figure 6-9a) is clearly delineating the faults, which can also be observed on the minimum similarity attribute (Figure 6-9b). The anomalies on the D-section are attributed to the diffractions produced by the fault system. Figure 6-10 shows in-line sections from the D-volumes computed for 2008, 2009 and 2010 datasets. In all the three D-sections, persistent anomalies are observed where faults are located above the injection zone. High semblance values (attributed to high diffractivity) are also located between the monitoring well (Naylor-1) and the injection well (CRC-1) at the injection level. Note that the reservoir is bounded by a number of faults, which are probably the main cause of high diffractivity at the Waarre-C reservoir level (~1600 ms TWTT); in addition, the reservoir hosts some free gas, mainly residual CH_4, which produces high acoustic contrast and hence high diffractivity at the edges. However, comparison of the diffractivity maps (Figure 6-11) along the Waarre-C reservoir reveals some arguably consistent changes with time, which may indicate the effect of injected CO_2.

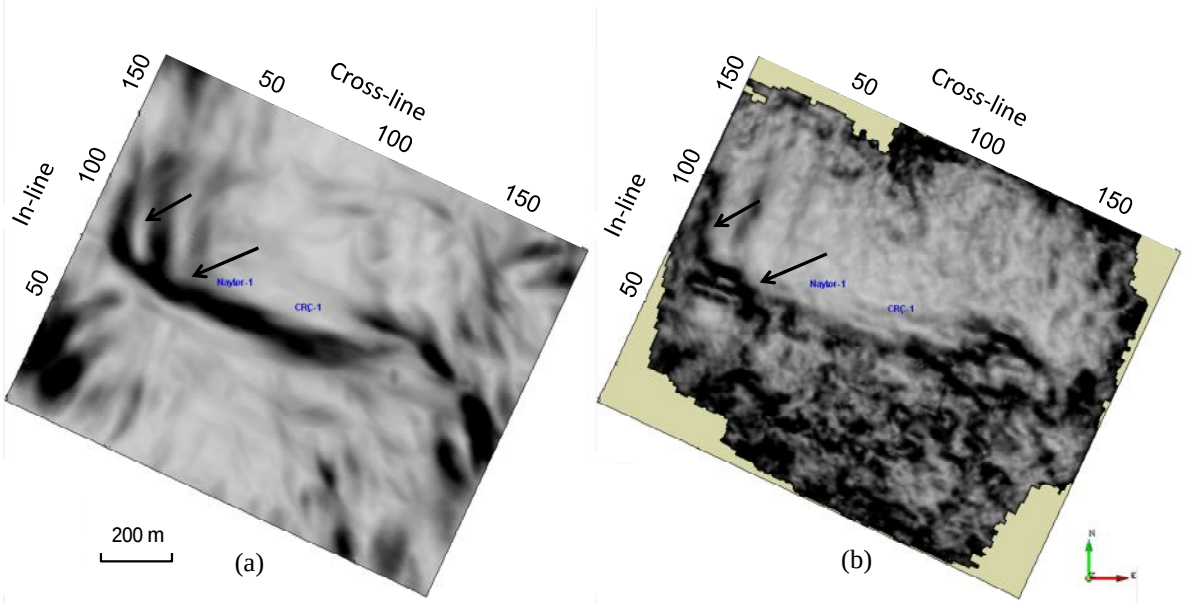

Figure 6-9: The comparison between two time slices of 2010 data at 1000 ms: (a) a D-section, and (b) a minimum similarity attribute. The arrows points to the location of faults.

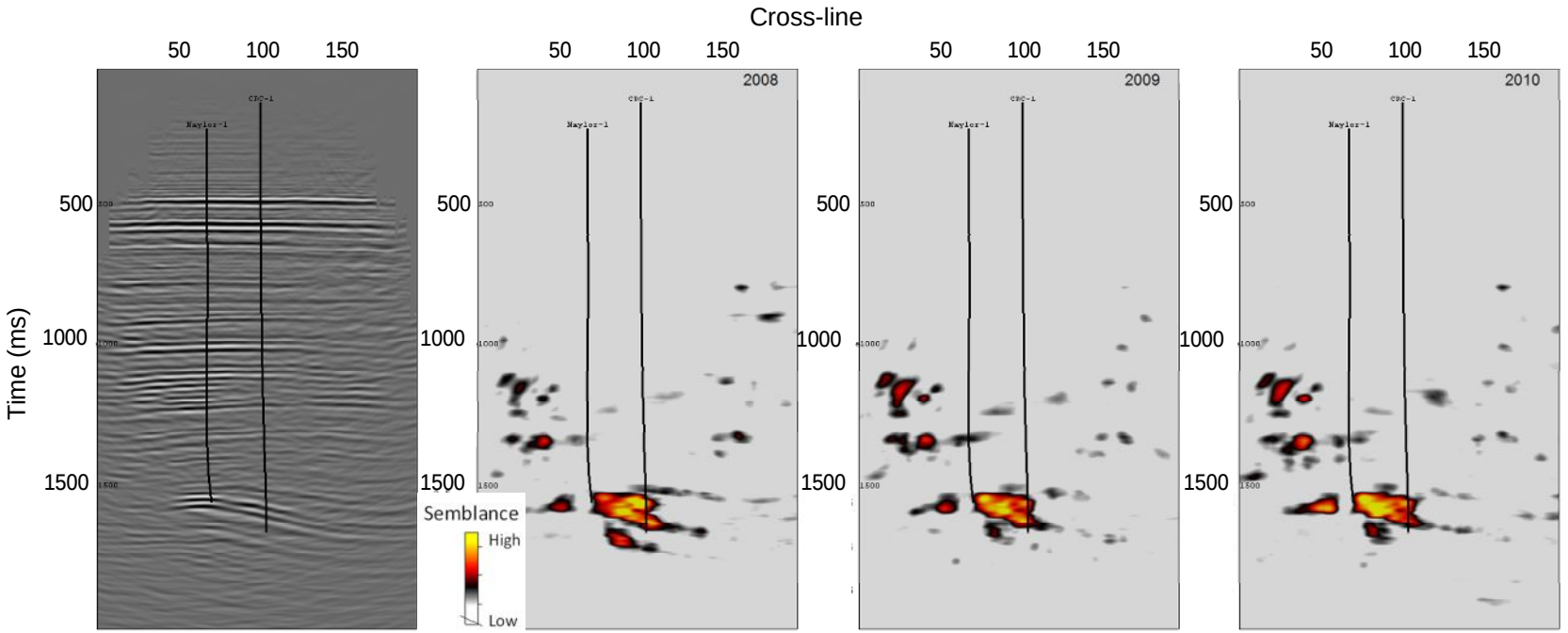

Figure 6-10: (a) The migrated section of in-line 87 showing the reservoir zone (at ~ 1600 ms) between the injection well (CRC-1) and the monitoring well (Naylor-1). (b) The same in-line of the pre-injection (2008), (c) after the injection of 35,000 tonnes of CO2 (2009), and (d) Post-injection (2010).

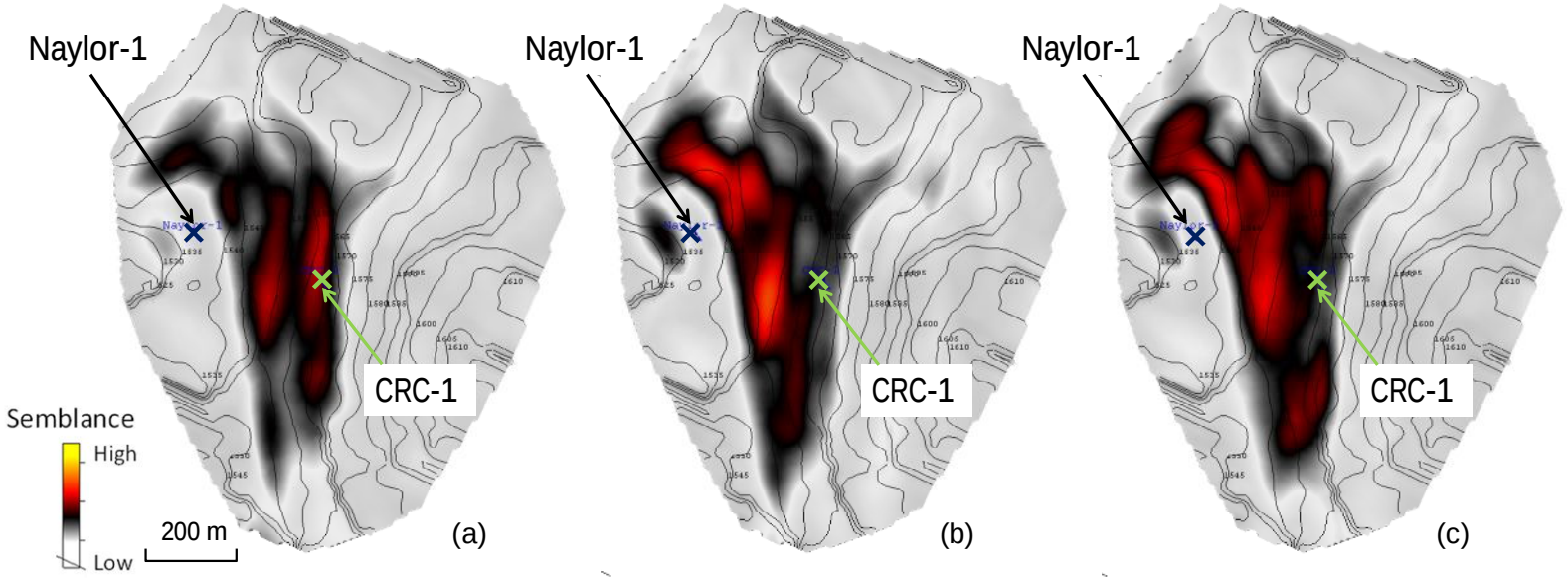

Figure 6-11: D-volume time slices at the top of the reservoir zone for: (a) the 2008 survey (pre-injection), (b) the 2009 survey (after injection 35,000 tonnes of CO2 and (c) the 2010 survey (post-injection).

6.5 4D Otway example

The same diffraction imaging technique has been applied to time-lapse data by using the difference between repeated stacked volumes as an input to the computation of the D-volumes. In an ideal situation only those edge diffractors that correspond to the boundaries of zones of subsurface changes can appear in the D-volumes. Figure 6-12 shows D-volumes of time-lapse difference data: Figure 6-12a shows the difference between the baseline (2008) and monitor I (2009). Figure 6-12b shows the difference between the baseline and monitor II (2010). Both D-volumes show high semblance values at the reservoir zone at about 1600 ms. There are also some areas of high diffractivity above the injection zone. They correspond mainly to the locations of the fault planes and can be explained by a slight misalignment of faults on different seismic data vintages caused by changes in statics/near-surface conditions.

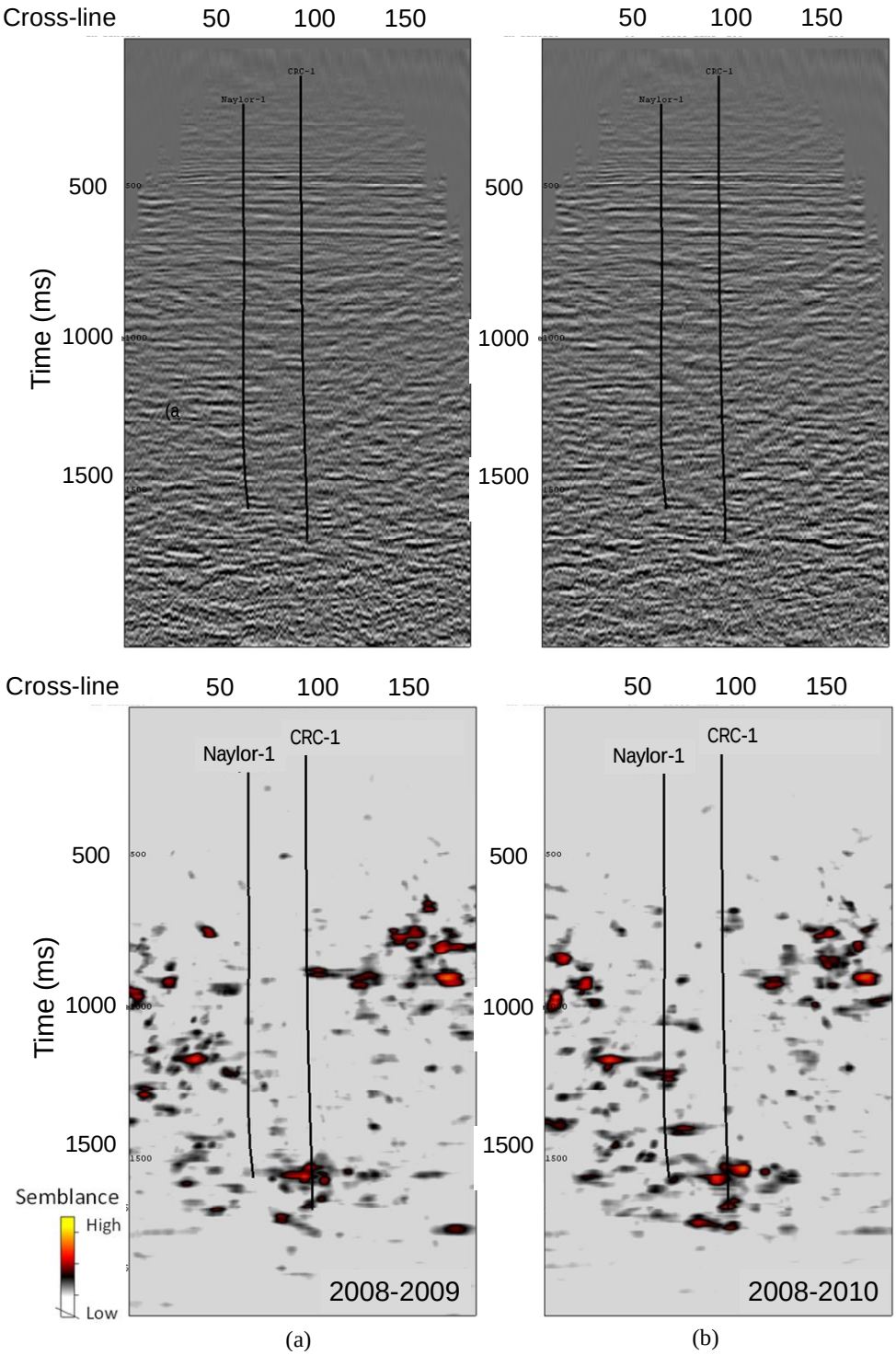

(a) (b)

Figure 6-12: (a) Time-lapse D-volumes obtained from the difference between 2008, 2009 and (b) 2008, 2010.

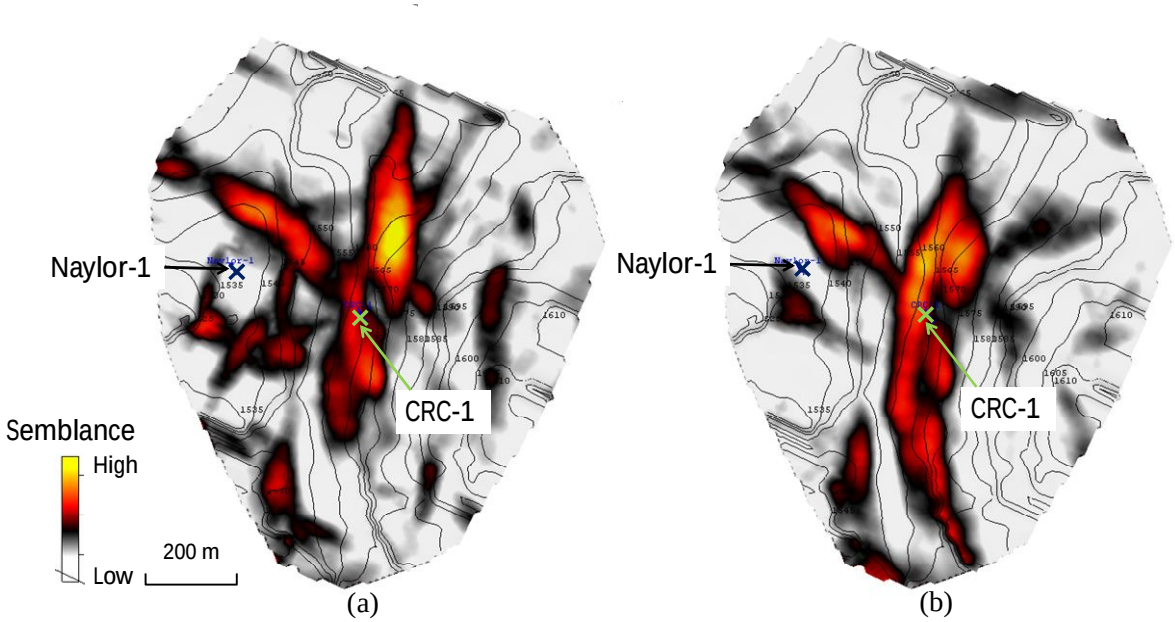

Figure 6-13: Time-lapse D-volumes of Waarre-C horizon showing high semblance values mapped on the difference volumes between: (a) 2008 and 2009 and (b) 2008 and 2010.

6.6 Discussion

I have generalised the method of diffraction imaging proposed by Landa and Keydar (1998) to a 3D stacked data case and tested it on synthetic and real data examples. The use of semblance, which examines data along a fixed time window, trades off the robustness of the imaging in the presence of random noise for resolution in time (vertical resolution). This robustness was illustrated by examining extreme noise conditions of up to 1000 % of random band-limited noise. The first 3D synthetic example (computed using the same frequency, geometry and velocities as in the field data) Figure 6-8, shows that the approach is capable of producing acceptable quality images for very low S/N ratio (as low as S/N =0.1). However, the background noise does affect the semblance value and makes the diffraction signals less coherent.

Figure 6-14 shows a comparison of the diffraction image with the result of conventional migration of the 3D grid test with S/N ration of 0.16. It is clear that the D-volume provides much better stability in poor S/N ratio conditions.

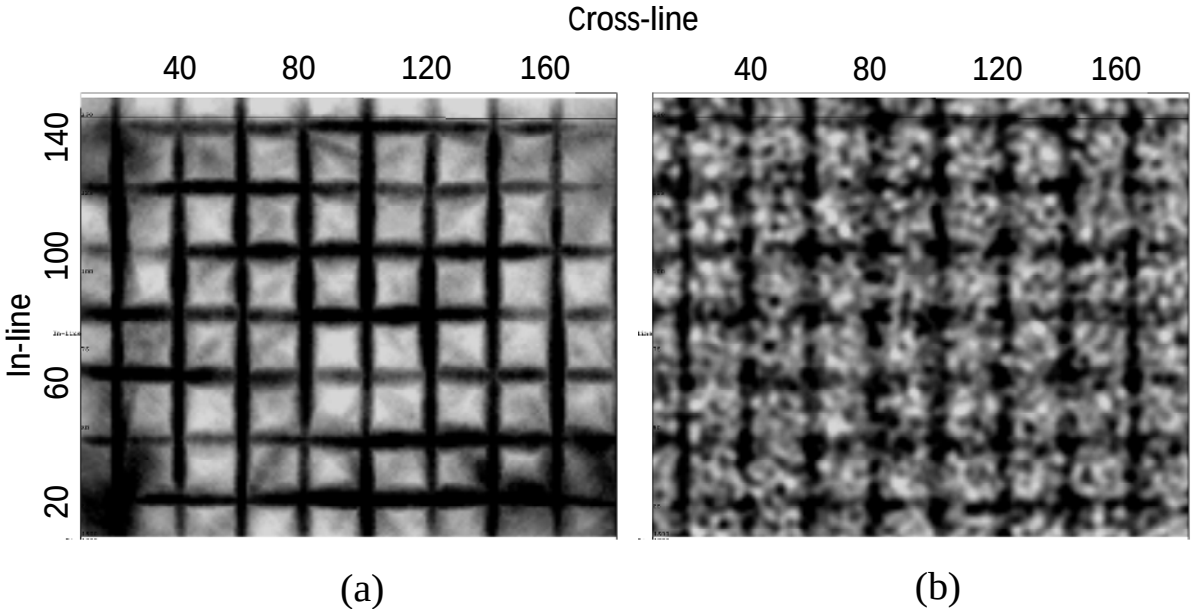

Figure 6-14: (a) A time-slice of the D-volume at 1600 ms compared to (b) post-stack migration of the same dataset; S/N = 0.16.

The noise-free tests of the algorithm on synthetic data show that the spatial resolution is decreasing with depth. As the arrival time of the diffracted waves increases, the image gets more distorted and blurry. This is clearly shown in Figure 6-7, where the deep diffractor lines (at 1600 ms time slice) are wider than the shallow ones.

In this chapter different offset limits have been examined as shown in Figure 6-5 and 6-6. At a shallow time a short offset limit is required and as the time increases a greater offset range is required. The variation of the resolution and optimal offset limit with depth are attributed to the shape of the diffraction hyperboloid, which varies with depth.

The technique was applied to Otway 3D/4D field data. As expected, when applied to 3D data, the approach allows us to produce reasonable images of the faults. The spatial resolution of the image obtained with the algorithm is comparable to the

resolution of the standard minimum similarity attribute, while the noise level is significantly lower on the D-volume slices.

In order to check if the higher semblance values shown in the D-volume attribute of the field data example truly correspond to edge diffractions we pick a point on the D-volume of 2010 Otway data around the reservoir level (1520 ms) located on the in-line 75 and cross-line 100. Figure 6-15 shows the maximum semblance value versus azimuth at that point. The maximum semblance value varies significantly with azimuth; the highest values are observed along the North-South direction. This agrees with the orientation of the edge diffraction, that is, orientation of the line, which we change across the polarity of the seismic data during computation of the D-volume. Thus the azimuthal variation of the semblance is consistent with the directivity expected from edge diffraction.

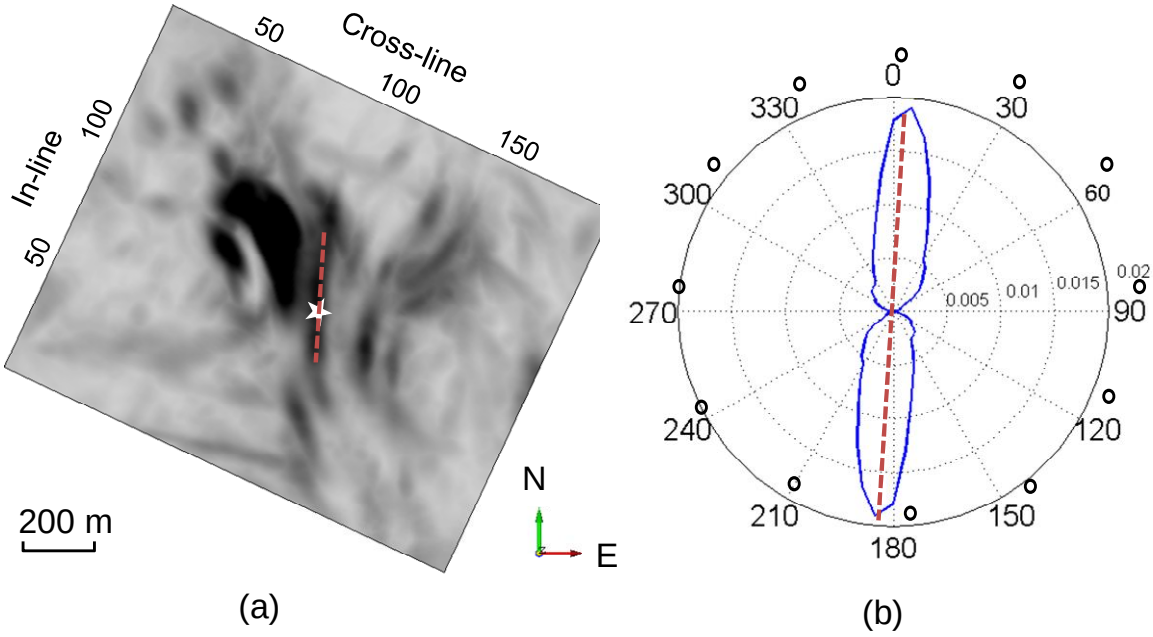

Figure 6-15: (a) A point at the reservoir level (1522 ms) indicated by star, located at in-line 75 and cross-line 100, and (b) the maximum semblance values of that point as a function of azimuth showing the direction of the edge diffraction. The high semblance values indicate the edge diffraction direction. The red lines in both images show that the orientation of the edge diffraction is perfectly aligned.

Application of the algorithm to the difference volumes reveals several interesting issues. On one hand, at the reservoir level we observe the highest diffractivity around the CRC-1 well (the injector) and the level of the signal is increasing with the increase of CO_2 volume (Figures 6-11 to 6-13). However, due to imperfect repeatability the areas of high level of diffracted energy can also be associated with the fault planes. Thus, even if we speculate that the changes at the reservoir level could be associated with the injection-related changes, significant caution is required in interpreting them.

6.7 Conclusions

In this chapter, the proposed diffraction imaging method was extended to work on 3D stacked data (or zero-offset) by including additional scanning over the diffractor's azimuth. Using the phase-reversal phenomena we can discriminate between linear and edge diffractors and to some extent suppress specular reflections.

A number of 3D synthetic tests based on real data geometry, frequency, and velocities show that the method is robust to the presence of random band-limited noise in the data. It shows that, at least in cases similar to Otway 3D surveys, S/N ratio of 0.1 is still acceptable for imaging using D-volumes. The actual threshold value is likely to be dependent on the post-stack geometry and depth of the scatterers as it will affect a portion of the diffracted wave traveltime curve and the number of traces used for coherency estimates. Even in mildly dipping structures, such as in the dipping plane example, the algorithm manages to focus the diffracted events on the termination of the plane. Comparison between the diffraction imaging and post-stack migration shows that the former is significantly more stable in presence of the large amount of noise.

The edge diffraction algorithm was applied to the field Otway 3D/4D seismic data. Single-vintage (3D) analysis shows that the algorithm efficiently detects fault planes without the need to suppress any specular reflections beforehand. This might be partially related to very mild dips of the reflectors observed in the area.

Application of the diffraction imaging to time-lapse seismic data should detect boundaries of the areas affected by changes at the reservoir level as all specular reflections and repeatable diffractions should cancel out by the subtraction of the

baseline stacked section from the monitor. However our field data example shows that misalignment of reflections close to the fault planes can contribute to the apparent diffractivity. Therefore, successful D-section imaging of the time-lapse data mainly depends on the “repeatability” of the seismic survey experiment.

Areas of high semblance values at the reservoir level observed for the Otway 4D seismic are mainly located around the injector well, that is, where we could expect to have actual time-lapse signals. However, due to the fact that the reservoir itself coincides with the area of high diffractive structures (faults), those high semblance values cannot be conclusively attributed to real subsurface changes only.

7. Chapter 7 - CONCLUSIONS AND FUTURE RESEARCH

7.1 Conclusions

Carbon capture and storage (CCS) is an emerging technology that can remove and store the CO_2 produced from industrial installations, which will help reduce greenhouse gas emissions from the atmosphere. Wide-scale CCS projects need to be established in order to make a significant contribution to meet this target. Therefore, sensitive monitoring tools such as seismic techniques capable of detecting small-scale CO_2 leakage and leakage pathways are necessities if carbon sequestration is ever to be a viable technology for the mitigation of greenhouse gases.

Time-lapse seismic techniques provide the most attractive approach for monitoring subsurface CO_2 plume migration and the potential release of CO_2 from a deep injection reservoir zone. However, the sensitivity of time-lapse seismic signals is affected by different factors, including the seismic repeatability of the survey area, the contrast between the physical properties of CO_2 and reservoir gas/fluid contents, as well as the reservoir lithology, structure and conditions (fluid pressure and temperature). All of these parameters need to be addressed for 4D seismic monitoring to be successful. Advanced processing techniques are therefore required in order to enhance the detectability of small time-lapse signals. Seismic diffraction imaging is one promising technique that may achieve this.

This thesis deals with seismic diffraction analysis and its application to CO_2 detection by focusing on the edge of objects. This has been accomplished by expanding the method presented by Landa and Keydar in 1987 to work on 3D seismic data. Many forward seismic modelling examples have been implemented in both 2D and 3D in order to gain more insight into edge diffraction and develop an approach that can best image diffractions and suppress reflections (chapters 5 and 6). Both numerical and physical experiments show that diffraction energy is much weaker than specular reflections and decays rapidly away from its apex.

The primary achievement of this thesis is the development of a technique that can extract more information from seismic data by focusing on diffracted waves. Utilising

the phase-reversal feature, which is exclusive to edge diffraction (sections 4.3 and 4.4) and using it as a criterion in the computation, allows us to produce an image that is more biased to diffraction energy than specular reflections. The algorithm scans over the linear/edge diffractor orientation azimuths and automatically performs a selection of a subset data that have the highest semblance value. The conventional Kirchhoff migration stacks the full data along the point scatterers' traveltime surface. In the case of linear diffractors, only a small part of this surface contains the signal, the rest is noise. Therefore, this approach allows adaptively selecting that portion of the data that hosts most of the signal. Working on stacked data makes the method more efficient and robust. There is a trade-off of vertical resolution for S/N ratio by using a relatively large vertical time window in the semblance function computation. This is done the same way as in the conventional normal move-out routine. The method relies on hyperbolic moveout and thus is limited to situations with moderate lateral velocity variations. This limitation is similar to that of the time migration. It is easy to envisage a modification of the method for strongly laterally heterogeneous media, where the diffraction traveltimes would be obtained from ray tracing methods.

The algorithm can also be applied to different data sets as shown in section 5.4 where GPR data is used. The results from the examples provided successfully locate discontinuities in the data and illustrate that diffraction analysis can recover more valuable details and image the important structures that could be masked by strong reflections. Even in mildly dipping structures such as in the dipping plane example (section 6.2), the algorithm manages to focus the diffracted events at the termination of the plane.

The result obtained from the time-lapse finite forward modelling (section 5.5) suggests that the first few thousand (1000 to 2000) tonnes of CO_2 could be visible in the seismic data using diffracted waves analysis. However, deep surface CO_2 quantifications require further investigation and calibration to improve the reliability of the results.

Applying the proposed method to Otway data, we can conclude the following findings:

- The algorithm for detection of diffracted waves allows us to obtain superior images in low S/N ratio data.
- Diffractions are reliable indicators of small-scale significant structures, such as cracks, faults and pinch-outs. This is illustrated in section 6.4 where 3D diffraction imaging analysis detected fault throws and identified their orientations.
- Application of diffraction imaging to time-lapse seismic data detects boundaries of the areas affected by changes at the reservoir level as all specular reflections and repeatable diffractions are cancelled out by the subtraction of the baseline stacked section from the monitor. However, caution is needed when interpreting time-lapse D-sections to avoid any artefacts that are attributed to non-repeatability issues.

Accordingly, in 4D (time-lapse) studies seismic diffraction analysis can help in imaging the change induced by CO_2 injection. Changes such as induced faults or cracks in the overlaying layer can be detected early enough for action to be taken. Ultimately, the thesis outcomes demonstrate that seismic diffraction analysis can be used as a substantial tool in CO_2 subsurface monitoring and provides a vital contribution to the M&V process in CO_2 sequestration projects.

7.2 Further research

For future research purposes, the diffracted waves imaging approach can be applied to other challenging situations, such as hard rock seismic exploration. A preliminary work presented by Tertyshnikov et al. (2013) shows that the diffracted waves method can be integrated into a steered migration algorithm. The proposed method can also be applied to different geometry settings as in VSP, where higher resolution results can be achieved. Moreover, the method can be modified to work in the pre-stack domain. Although utilising the diffracted waves method on a pre-stack domain might be computationally expensive, this could be justified if the output image can

provide more reliable diffraction information. In this case, a pre-stack time-lapse data analysis is required before D-section computation. Finally, in order to examine the validity of the method it is recommended to test it in other projects such as Cranfield or Ketzin.

REFERENCES

Al-Jabri, Y., and M. Urosevic, 2010, Assessing the repeatability of reflection seismic data in the presence of complex near-surface conditions CO2CRC Otway Project, Victoria, Australia: Exploration Geophysics, **41**, 24-30.

Alonaizi, F., R. Pevzner, A. Bona, M. Alshamry, E. Caspari, and B. Gurevich, 2013, Application of Diffracted wave analysis to time-lapse seismic data for CO_2 leakage detection: Geophysical Prospecting. doi: 10.1111/1365-2478.12085

Alonaizi, F., R. Pevzner, A. Bona, E. Caspari, and B. Gurevich, 2011, Application of Diffracted wave analysis to time-lapse seismic data for CO_2 leakage detection: Presented at the 73rd EAGE Conference and Exhibition, Extended abstract.

Arts, R., O. Eiken, A. Chadwick, P. Zweigel, L. van der Meer, and B. Zinszner, 2004, Monitoring of CO_2 injected at Sleipner using time-lapse seismic data: Energy, **29**, 1383-1392.

Audebert, F., P. Froidevaux, H. Rakotoarisoa, and J. S. Lucas, 2002, Insights Into Migration In the Angle Domain: Presented at the 72nd SEG Annual International Meeting.

Bancroft, J. C., 2007, A Practical Understanding of Pre-and Poststack Migrations: Prestack: Soc of Exploration Geophysicists.

Bannister, S., A. Nicol, R. Funnell, D. Etheridge, B. Christenson, J. Underschultz, G. Caldwell, V. Stagpoole, A. Kepic, and L. Stalker, 2009, Opportunities for underground geological storage of CO2 in New Zealand-Report CCS-08/11-Monitoring and verification methodologies: GNS Science Report, **64**.

Bansal, R., and M. G. Imhof, 2005, Diffraction enhancement in prestack seismic data: Geophysics, **70**, V73-V79.

Batzle, M., and Z. Wang, 1992, Seismic properties of pore fluids: Geophysics, **57**, 1396-1408.

Benson, S., and L. Myer, 2000, Monitoring to ensure safe and effective geologic sequestration of carbon dioxide: Presented at the IPCC workshop on carbon dioxide capture and storage, Citeseer.

Benson, S. M., 2006, Monitoring Carbon Dioxide Sequestration in Deep Geological Formations for Inventory Verification and Carbon Credits: Presented at the SPE Annual Technical Conference and Exhibition, Society of Petroleum Engineers.

Benson, S. M., and D. R. Cole, 2008, CO_2 Sequestration in Deep Sedimentary Formations: Elements, **4**, 325-331.

Beres, M., and F. P. Haeni, 1991, Application of Ground-Penetrating-Radar Methods in Hydrogeologie Studies: Ground Water, **29**, 375-386.

Berkovitch, A., I. Belfer, Y. Hassin, and E. Landa, 2009, Diffraction imaging by multifocusing: Geophysics, **74**, WCA75-WCA81.

Berkovitch, A., I. Belfer, and E. Landa, 2008, Multifocusing as a method of improving subsurface imaging: The Leading Edge, **27**, 250-256.

Berkovitch, A., B. Gelchinsky, and S. Keydar, 1994, Basic formulae for multifocusing stack: Presented at the 56th EAEG Meeting.

Berkovitch, A., S. Keydar, E. Landa, and P. Trachtman, 1998, Multifocusing in Practice: SEG Technical Program Expanded Abstracts, **17**, 1748-1751.

Berryhill, J. R., 1977, Diffraction response for nonzero separation of source and receiver: Geophysics, **42**, 1158-1176.

Bohnhoff, M., M. D. Zoback, L. Chiaramonte, J. L. Gerst, and N. Gupta, 2010, Seismic detection of CO_2 leakage along monitoring wellbores: International Journal of Greenhouse Gas Control, **4**, 687-697.

Boreham, C., J. Underschultz, L. Stalker, D. Kirste, B. Freifeld, C. Jenkins, and J. Ennis-King, 2011, Monitoring of CO_2 storage in a depleted natural gas reservoir: Gas geochemistry from the CO2CRC Otway Project, Australia: International Journal of Greenhouse Gas Control, **5**, 1039-1054.

Born, M., and E. Wolf, 1999, Principles of optics: electromagnetic theory of propagation, interference and diffraction of light: CUP Archive.

Brock, W., and L. Bryan, 1989, Summary results of CO_2 EOR field tests, 1972-1987: Presented at the Low Permeability Reservoirs Symposium.

Cairns, G., H. Jakubowicz, L. Lonergan, and A. Muggeridge, 2012, Using time-lapse seismic monitoring to identify trapping mechanisms during CO_2 sequestration: International Journal of Greenhouse Gas Control, **11**, 316-325.

Caspari, E., J. Ennis-King, R. Pevzner, and B. Gurevich, 2012, Prediction of the seismic time-lapse signal of CO_2/CH_4 injection into a depleted gas reservoir - Otway Project: ASEG Extended Abstracts, **2012**, 1-4.

Chadwick, A., G. Williams, N. Delepine, V. Clochard, K. Labat, S. Sturton, M.-L. Buddensiek, M. Dillen, M. Nickel, A. L. Lima, R. Arts, F. Neele, and G. Rossi, 2010, Quantitative analysis of time-lapse seismic monitoring data at the Sleipner CO_2 storage operation: The Leading Edge, **29**, 170-177.

Chadwick, R. A., R. Arts, and O. Eiken, 2005, 4D seismic quantification of a growing CO_2 plume at Sleipner, North Sea: Geological Society, London, Petroleum Geology Conference **6**, 1385-1399.

Chang, K. W., S. Minkoff, and S. Bryant, 2008, Modeling leakage through faults of CO_2 stored in an aquifer: Presented at the SPE Annual Technical Conference and Exhibition.

Claerbout, J. F., 1992, Earth soundings analysis: Processing versus inversion: Blackwell Scientific Publications Cambridge, Massachusetts, USA.

de Figueiredo, J. J. S., F. Oliveira, E. Esmi, L. Freitas, J. Schleicher, A. Novais, P. Sussner, and S. Green, 2013, Automatic detection and imaging of diffraction points using pattern recognition: Geophysical Prospecting, **61**, 368-379.

Demirbas, A., A. Sahin-Demirbas, and A. Hilal Demirbas, 2004, Global Energy Sources, Energy Usage, and Future Developments: Energy Sources, **26**, 191-204.

Dethlefsen, F., R. Köber, D. Schäfer, S. A. a. Hagrey, G. Hornbruch, M. Ebert, M. Beyer, J. Großmann, and A. Dahmke, 2013, Monitoring Approaches for

Detecting and Evaluating CO_2 and Formation Water Leakages into Near-surface Aquifers: Energy Procedia, **37**, 4886-4893.

Dickinson, R. E., and R. J. Cicerone, 1986, Future global warming from atmospheric trace gases: Nature, **319**, 109-115.

Durucan, S., J.-Q. Shi, C. Sinayuc, and A. Korre, 2011, In Salah CO_2 storage JIP: Carbon dioxide plume extension around KB-502 well–New insights into reservoir behaviour at the In Salah storage site: Energy Procedia, **4**, 3379-3385.

Eiken, O., P. Ringrose, C. Hermanrud, B. Nazarian, T. A. Torp, and L. Høier, 2011, Lessons learned from 14 years of CCS operations: Sleipner, In Salah and Snøhvit: Energy Procedia, **4**, 5541-5548.

Elodie, J., and S. Philippe, 2012, The Relevance of Geochemical Tools to Monitor Deep Geological CO_2 Storage Sites-Geochemistry - Earth's System Processes.

Feynman, R. P., 2006, QED: The strange theory of light and matter: Princeton University Press.

Figueroa, J. D., T. Fout, S. Plasynski, H. McIlvried, and R. D. Srivastava, 2008, Advances in CO_2 capture technology—The U.S. Department of Energy's Carbon Sequestration Program: International Journal of Greenhouse Gas Control, **2**, 9-20.

Flett, M., J. Brantjes, R. Gurton, J. McKenna, T. Tankersley, and M. Trupp, 2009, Subsurface development of CO_2 disposal for the Gorgon Project: Energy Procedia, **1**, 3031-3038.

Fomel, S., 2002, Applications of plane-wave destruction filters: Geophysics, **67**, 1946-1960.

Fomel, S., E. Landa, and M. T. Taner, 2007, Poststack velocity analysis by separation and imaging of seismic diffractions: Geophysics, **72**, U89-U94.

Freifeld, B. M., R. C. Trautz, Y. K. Kharaka, T. J. Phelps, L. R. Myer, S. D. Hovorka, and D. J. Collins, 2005, The U-tube: A novel system for acquiring borehole fluid samples from a deep geologic CO_2 sequestration experiment: Journal of Geophysical Research: Solid Earth, **110**, B10203.

Fresnel, A., 1819, La diffraction de la lumiere: Presented at the Annales de Chimie et Physique.

Fu, C., and T. Gundersen, 2012, Carbon Capture and Storage in the Power Industry: Challenges and Opportunities: Energy Procedia, **16, Part C**, 1806-1812.

Fulcheri, L., and Y. Schwob, 1995, From methane to hydrogen, carbon black and water: International Journal of Hydrogen Energy, **20**, 197-202.

Gassmann, F., 1951, Elastic waves through a packing of spheres: Geophysics, **16**, 673-685.

Goodman, J. W., and S. C. Gustafson, 1996, Introduction to Fourier optics: Optical Engineering, **35**, 1513-1513.

Grimaldi, F. M., 1665, Physico-mathesis de lvmine, coloribvs, et iride, aliisque adnexis libri duo: opvs posthvmvm.

Harlan, W. S., J. F. Claerbout, and F. Rocca, 1983, Extracting velocities from diffractions: SEG Technical Program Expanded Abstracts, **2**, 574-577.

Hermanrud, C., T. Andresen, O. Eiken, H. Hansen, A. Janbu, J. Lippard, H. N. Bolås, T. H. Simmenes, G. M. G. Teige, and S. Østmo, 2009, Storage of CO_2 in saline aquifers–Lessons learned from 10 years of injection into the Utsira Formation in the Sleipner area: Energy Procedia, **1**, 1997-2004.

Houghton, J. T., Y. Ding, D. J. Griggs, M. Noguer, P. J. van der LINDEN, X. Dai, K. Maskell, and C. Johnson, 2001, Climate change 2001: the scientific basis: Cambridge University Press Cambridge.

Hoversten, G. M., R. Gritto, T. M. Daley, E. L. Majer, and L. R. Myer, 2002, Crosswell seismic and electromagnetic monitoring of CO_2 sequestration.

Huygens, C., 1690, Treatise on Light, translated and edited by SP Thompson: University of Chicago Press, Chicago.

IEAGHG, 2012, IEAGHG, "Quantification Techniques For CO_2 Leakage", 2012/02, January, 2012.

Jeandel, E., A. Battani, and P. Sarda, 2010, Lessons learned from natural and industrial analogues for storage of carbon dioxide: International Journal of Greenhouse Gas Control, **4**, 890-909.

Jenkins, C. R., P. J. Cook, J. Ennis-King, J. Undershultz, C. Boreham, T. Dance, P. de Caritat, D. M. Etheridge, B. M. Freifeld, and A. Hortle, 2012, Safe storage and effective monitoring of CO_2 in depleted gas fields: Proceedings of the National Academy of Sciences, **109**, E35-E41.

Jenkins, C. R., P. J. Cook, J. Ennis-King, J. Undershultz, C. Boreham, T. Dance, P. de Caritat, D. M. Etheridge, B. M. Freifeld, A. Hortle, D. Kirste, L. Paterson, R. Pevzner, U. Schacht, S. Sharma, L. Stalker, and M. Urosevic, 2011, Safe storage and effective monitoring of CO_2 in depleted gas fields: Proceedings of the National Academy of Sciences.

Jensen, G. K. S., E. H. Nickel, and B. J. Rostron, 2013, Refinement of the Weyburn-Midale geological and hydrogeological model: Developing a better framework to determine reservoir response to injected CO_2 and subsequent CO_2 movement: International Journal of Greenhouse Gas Control, **16, Supplement 1**, S5-S14.

Kanasewich, E. R., and S. M. Phadke, 1988, Imaging discontinuities on seismic sections: Geophysics, **53**, 334-345.

Kazemeini, S. H., C. Juhlin, and S. Fomel, 2010, Monitoring CO_2 response on surface seismic data; a rock physics and seismic modeling feasibility study at the CO_2 sequestration site, Ketzin, Germany: Journal of Applied Geophysics, **71**, 109-124.

Keller, J. B., 1962, Geometrical Theory of Diffraction: J. Opt. Soc. Am., **52**, 116-130.

Khaidukov, V., E. Landa, and T. J. Moser, 2004, Diffraction imaging by focusing-defocusing: An outlook on seismic superresolution: Geophysics, **69**, 1478-1490.

Klem-Musatov, K. D., 2008, Edge and Tip Diffractions: Theory and Applications in Seismic Prospecting: Soc of Exploration Geophysicists.

Klem-Musatov, K. D., and A. M. Aizenberg, 1989, The edge wave superposition method (2-D scalar problem): Geophysical Journal International, **99**, 351-367.

Klokov, A., R. Baina, E. Landa, P. Thore, and I. Tarrass, 2010, Diffraction imaging for fracture detection: synthetic case study: SEG Technical Program Expanded Abstracts, **29**, 3354-3358.

Korre, A., C. E. Imrie, F. May, S. E. Beaubien, V. Vandermeijer, S. Persoglia, L. Golmen, H. Fabriol, and T. Dixon, 2011, Quantification techniques for potential CO_2 leakage from geological storage sites: Energy Procedia, **4**, 3413-3420.

Kragh, E., and P. Christie, 2002, Seismic repeatability, normalized rms, and predictability: The Leading Edge, **21**, 640-647.

Krey, T., 1952, The segnificance of diffraction in the investigating of faults: Geophysics, **17**, 843-858.

Kumar, A., A. Datta-Gupta, R. Shekhar, and R. Gibson, 2008, Modeling time lapse seismic monitoring of CO_2 sequestration in hydrocarbon reservoirs including compositional and geochemical effects: Petroleum Science and Technology, **26**, 887-911.

Kunz, O., R. Klimeck, W. Wagner, and M. Jaeschke, 2004, The GERG-2004 Wide-Range Equation of State for Natural Gases and Other Mixtures: GERG TM15-2007.

Landa, E., 2007, Beyond conventional seismic imaging: EAGE publications.

Landa, E., S. Fomel, and M. Reshef, 2008, Separation, imaging, and velocity analysis of seismic diffractions using migrated dip-angle gathers.

Landa, E., and S. Keydar, 1998, Seismic monitoring of diffraction images for detection of local heterogeneities: Geophysics, **63**, 1093-1100.

Landa, E., M. Rauch-Davies, A. Berkovitch, D. Pelman, and K. Deev, 2013, Using Multi-focusing 3D Diffraction Imaging to Predict Fracture Corridors/Swarms in the Bazhenov Formation: Presented at the 75th EAGE Conference & Exhibition incorporating SPE EUROPEC 2013.

Landa, E., V. Shtivelman, and B. Gelchinsky, 1987, A method for detection of diffracted waves on common-offset sections: Geophysical Prospecting, **35**, 359-373.

Leuning, R., D. Etheridge, A. Luhar, and B. Dunse, 2008, Atmospheric monitoring and verification technologies for CO_2 geosequestration: International Journal of Greenhouse Gas Control, **2**, 401-414.

Lewicki, J. L., G. E. Hilley, and C. M. Oldenburg, 2005, An improved strategy to detect CO_2 leakage for verification of geologic carbon sequestration: Geophysical Research Letters, **32**, L19403.

Lipponen, J., K. Burnard, B. Beck, J. Gale, and B. Pegler, 2011, The IEA CCS Technology Roadmap: One Year On: Energy Procedia, **4**, 5752-5761.

Lumley, D., 2010, 4D seismic monitoring of CO_2 sequestration: The Leading Edge, **29**, 150-155.

Lumley, D., D. Adams, R. Wright, D. Markus, and S. Cole, 2008, Seismic monitoring of CO_2 geo-sequestration: realistic capabilities and limitations: SEG Technical Program Expanded Abstracts, **27**, 2841-2845.

Martens, S., A. Liebscher, F. Möller, J. Henninges, T. Kempka, S. Lüth, B. Norden, B. Prevedel, A. Szizybalski, M. Zimmer, M. Kühn, and K. Group, 2013, CO_2 Storage at the Ketzin Pilot Site, Germany: Fourth Year of Injection, Monitoring, Modelling and Verification: Energy Procedia, **37**, 6434-6443.

Mathieson, A., J. Midgely, I. Wright, N. Saoula, and P. Ringrose, 2011, In Salah CO_2 Storage JIP: CO_2 sequestration monitoring and verification technologies applied at Krechba, Algeria: Energy Procedia, **4**, 3596-3603.

Mathieson, A., I. Wright, D. Roberts, and P. Ringrose, 2009, Satellite imaging to monitor CO2 movement at Krechba, Algeria: Energy Procedia, **1**, 2201-2209.

Mavko, G., T. Mukerji, and J. Dvorkan, 1998, The Rock Physics Handbook: Cambridge University Press.

McCoy, S. T., and E. S. Rubin, 2008, An engineering-economic model of pipeline transport of CO2 with application to carbon capture and storage: International Journal of Greenhouse Gas Control, **2**, 219-229.

Metz, B., O. Davidson, H. de Coninck, M. Loos, and L. Meyer, 2005, IPCC special report on carbon dioxide capture and storage: Intergovernmental Panel on Climate Change, Geneva (Switzerland). Working Group III.

Michael, K., A. Golab, V. Shulakova, J. Ennis-King, G. Allinson, S. Sharma, and T. Aiken, 2010, Geological storage of CO2 in saline aquifers—A review of the experience from existing storage operations: International Journal of Greenhouse Gas Control, **4**, 659-667.

Moser, T., 2011, Edge and tip diffraction imaging in three dimensions: Presented at the 73rd EAGE Conference & Exhibition.

Moser, T. J., and C. B. Howard, 2008, Diffraction imaging in depth: Geophysical Prospecting, **56**, 627-641.

Muncaster, R., 1993, A-level Physics: Nelson Thornes.

Nordbotten, J. M., M. A. Celia, S. Bachu, and H. K. Dahle, 2004, Semianalytical Solution for CO_2 Leakage through an Abandoned Well: Environmental Science & Technology, **39**, 602-611.

Oldenburg, C., and J. Lewicki, 2006, On leakage and seepage of CO_2 from geologic storage sites into surface water: Environmental Geology, **50**, 691-705.

Oldenburg, C. M., and A. J. A. Unger, 2003, On Leakage and Seepage from Geologic Carbon Sequestration Sites: Unsaturated Zone Attenuation: Vadose Zone Journal, **2**, 287-296.

Pant, D. R., S. A. Greenhalgh, and B. Zhou, 1992, Physical and numerical model study of diffraction effects on seismic profiles over simple structures: Geophysical Journal International, **108**, 906-916.

Papziner, U., and K.-P. Nick, 1998, Automatic detection of hyperbolas in georadargrams by slant-stack processing and migration: First Break, **16**, 219-223.

Park, J., M. Fawad, I. Viken, E. Aker, and T. I. Bjørnarå, 2013, CSEM Sensitivity Study for Sleipner CO_2-injection Monitoring: Energy Procedia, **37**, 4199-4206.

Pevzner, R., V. Shulakova, A. Kepic, Y. Al-Jabri, and M. Urosevic, 2009, Repeatability of Land Time-lapse Seismic Surveys–Otway Project 2D Test Line Case Study: Presented at the 71st EAGE Conference & Exhibition.

Pevzner, R., V. Shulakova, A. Kepic, and M. Urosevic, 2011, Repeatability analysis of land time-lapse seismic data: CO2CRC Otway pilot project case study: Geophysical Prospecting, **59**, 66-77.

Plasynski, S. I., J. T. Litynski, H. G. McIlvried, D. M. Vikara, and R. D. Srivastava, 2011, The critical role of monitoring, verification, and accounting for geologic carbon dioxide storage projects: Environmental Geosciences, **18**, 19-34.

Porter, R., and M. Teich, 1992, The scientific revolution in national context: Cambridge University Press.

Pruess, K., 2005, Numerical studies of fluid leakage from a geologic disposal reservoir for CO_2 show self-limiting feedback between fluid flow and heat transfer: Geophysical Research Letters, **32**, L14404.

Reshef, M., and E. Landa, 2009, Post-stack velocity analysis in the dip-angle domain using diffractions: Geophysical Prospecting, **57**, 811-821.

Reshef, M., A. Reshef, and Rüger, 2005, Influence of structural dip on interval velocity analysis: Presented at the 75th SEG Annual International meeting.

Sauer, U., C. Schütze, C. Leven, S. Schlömer, and P. Dietrich, 2013, An Integrative Hierarchical Monitoring Approach for Detecting and Characterizing CO_2 Releases: Energy Procedia, **37**, 4257-4267.

Scales, J., 1997, Theory of Seismic Imaging: Samizdat Press, e-book.

Schmidt-Hattenberger, C., P. Bergmann, D. Bösing, T. Labitzke, M. Möller, S. Schröder, F. Wagner, and H. Schütt, 2013, Electrical Resistivity Tomography (ERT) for Monitoring of CO_2 Migration - from Tool Development to Reservoir Surveillance at the Ketzin Pilot Site: Energy Procedia, **37**, 4268-4275.

Sharma, S., P. Cook, T. Berly, and C. Anderson, 2007, Australia's first geosequestration demonstration project-the CO2CRC Otway Basin Pilot Project: APPEA journal, 259-270.

Sharma, S., P. Cook, T. Berly, and M. Lees, 2009, The CO2CRC Otway Project: Overcoming challenges from planning to execution of Australia's first CCS project: Energy Procedia, **1**, 1965-1972.

Shulakova, V., R. Pevsner, M. Urosevic, and A. Kepic, 2012, CO2CRC Otway Project 3D/4D seismic data processing.

Simone, A., E. Mackie, and N. Jenvey, 2009, CO_2 geological storage field development–Application of baseline, monitoring and verification technology: Energy Procedia, **1**, 2219-2226.

Smith, T. M., C. H. Sondergeld, and C. S. Rai, 2003, Gassmann fluid substitutions: A tutorial: Geophysics, **68**, 430-440.

Statoil, 2007, Carbon capture and storage-Sleipner Vest.

Stephens, J. C., 2006, Growing interest in carbon capture and storage(CCS) for climate change mitigation: Sustainability: Science Practice and Policy, **2**, 4-13.

Sweatman, R., S. Crookshank, and S. Edman, 2011, Outlook and technologies for offshore CO_2 EOR/CCS projects: Offshore Technology Conference.

Taner, M., 1976, Simplan: Similated plane-wave exploration: 46th Annual International Meeting: Presented at the SEG, Expanded Abstracts.

Taner, M. T., S. T. Fomel, and E. Landa, 2006, Separation and imaging of seismic diffractions using plane-wave decomposition: Presented at the 2006 SEG Annual Meeting.

Taner, M. T., and F. Koehler, 1969, Velocity spectra-digital computer derivation applications of velocity functions: Geophysics, **34**, 859-881.

Tertyshnikov, K., R. Pevzner, A. Bóna, F. Alonaizi, and B. Gurevich, 2013, Steering Migration with Diffractions in Seismic Exploration for Hard Rock Environments: Presented at the 75th EAGE Conference & Exhibition incorporating SPE EUROPEC 2013.

Tingdahl, K. M., and M. De Rooij, 2005, Semi-automatic detection of faults in 3D seismic data: Geophysical Prospecting, **53**, 533-542.

Torp, T. A., and J. Gale, 2004, Demonstrating storage of CO2 in geological reservoirs: The Sleipner and SACS projects: Energy, **29**, 1361-1369.

Trorey, A. W., 1970, A simple theory for seismic diffractions: Geophysics, **35**, 762-784.

Trorey, A. W., 1977, Diffraction for arbitrary source-receiver locations: Geophysics, **42**, 1177-1182.

Tsang, C.-F., S. M. Benson, B. Kobelski, and R. E. Smith, 2002, Scientific considerations related to regulation development for CO2 sequestration in brine formations: Environmental Geology, **42**, 275-281.

Urosevic, M., R. Pevzner, A. Kepic, P. Wisman, V. Shulakova, and S. Sharma, 2010, Time-lapse seismic monitoring of CO_2 injection into a depleted gas reservoir-Naylor Field, Australia: The Leading Edge, **29**, 164-169.

Urosevic, M., R. Pevzner, V. Shulakova, A. Kepic, E. Caspari, and S. Sharma, 2011, Seismic monitoring of CO2 injection into a depleted gas reservoir–Otway Basin Pilot Project, Australia: Energy Procedia, **4**, 3550-3557.

Verdon, J., J. Kendall, D. White, D. Angus, Q. Fisher, and T. Urbancic, 2010, Passive seismic monitoring of carbon dioxide storage at Weyburn: The Leading Edge, **29**, 200-206.

Vermeulen, J., B. Gurevich, M. Urosevic, and E. Landa, 2006, Enhancing coherency analysis for fault detection and mapping using 3D diffraction imaging: SEG Technical Program Expanded Abstracts, **25**, 1108-1112.

Wells, A. W., R. W. Hammack, G. A. Veloski, J. R. Diehl, B. R. Strazisar, H. Rauch, T. H. Wilson, and C. M. White, 2006, Monitoring, mitigation, and verification at sequestration sites: SEQURE technologies and the challenge for geophysical detection: The Leading Edge, **25**, 1264-1270.

White, C. M., B. R. Strazisar, E. J. Granite, J. S. Hoffman, and H. W. Pennline, 2003, Separation and Capture of CO2 from Large Stationary Sources and Sequestration

in Geological Formations—Coalbeds and Deep Saline Aquifers: Journal of the Air & Waste Management Association, **53**, 645-715.

White, D., 2009, Monitoring CO_2 storage during EOR at the Weyburn-Midale Field: The Leading Edge, **28**, 838-842.

White, D. J., 2011, Geophysical monitoring of the Weyburn CO2 flood: Results during 10 years of injection: Energy Procedia, **4**, 3628-3635.

Wildenborg, T., M. Bentham, A. Chadwick, P. David, J.-P. Deflandree, M. Dillen, H. Groenenberg, K. Kirk, and Y. L. Gallo, 2009, Large-scale CO2 injection demos for the development of monitoring and verification technology and guidelines (CO2 ReMoVe): Energy Procedia, **1**, 2367-2374.

Young, T., 1804, The Bakerian Lecture: Experiments and Calculations Relative to Physical Optics: Philosophical Transactions of the Royal Society of London, **94**, 1-16.

Yuh, S. H., and R. L. Gibson, 2001, Time-lapse seismic monitoring of CO_2 sequestration in hydrocarbon reservoirs: SEG Technical Program Expanded Abstracts, **20**, 1627-1630.

---

*McColpin, G. R., 2009, Surface deformation monitoring as a cost effective MMV method: Energy Procedia, **1**, 2079-2086.*

*Ringrose, P., M. Atbi, D. Mason, M. Espinassous, Ø. Myhrer, M. Iding, A. Mathieson, and I. Wright, 2009, Plume development around well KB-502 at the In Salah CO2 storage site: First Break, **27**.*

White, D., Year, Geophysical Monitoring at the Aquistore CO2 Storage Site, Saskatchewan, Canada: AGU Fall Meeting Abstracts, 01.